

THÈSE

Pour obtenir le grade de

DOCTEUR DE L'UNIVERSITÉ DE REIMS CHAMPAGNE-ARDENNE

Discipline : MÉCANIQUE DES SOLIDES, GÉNIE MÉCANIQUE, PRODUCTIQUE, TRANSPORT ET GÉNIE CIVIL

Spécialité : SGM - Sciences et Génie des Matériaux

Présentée et soutenue publiquement par

Anoop Ebey THOMAS

Le 17 avril 2019

THERMO-VISCOPLASTIC NUMERICAL MODELING OF METAL FORGING PROCESS BY THE PSEUDO INVERSE APPROACH

Thèse dirigée par **Boussad ABBES**

JURY

M. Francisco CHINESTA	Professeur, ENSAM ParisTech	Président
M. Amine AMMAR	Professeur, Arts et Métiers ParisTech - Angers	Rapporteur
M. Pascal LAFON	Professeur, Université de Technologie de Troyes	Rapporteur
M. Hamid ZAHROUNI	Professeur, Université de Lorraine	Examineur
M. Jean-Louis DUVAL	Product Line Manager - VI, ESI Group	Examineur
M. Boussad ABBES	Professeur, Université de Reims Champagne-Ardenne	Directeur de thèse
M. Yu Ming LI	HDR, Université de Reims Champagne-Ardenne	Co-Directeur
Mme. Fazilay ABBES	Maître de Conférences, Université de Reims Champagne-Ardenne	Co-Directeur
Mme. Anne CHAMBARD	Product Marketing Manager, ESI Group	Invité



Abstract

Modélisation numérique thermo-viscoplastique du procédé de forgeage des métaux par l'Approche Pseudo Inverse

Le forgeage à chaud est un procédé de formage des métaux utilisé pour former des matériaux qui sont difficiles à former à froid ainsi que pour réaliser des géométries complexes. La réduction de la limite d'élasticité à haute température et une augmentation subséquente de l'aptitude à la mise en forme constituent le principal mécanisme à l'origine du procédé. Les méthodes numériques constituent un moyen efficace de prédire les états de contrainte / déformation du produit à différentes étapes de la mise en forme. Bien que les méthodes classiques soient suffisamment précises pour fournir une représentation appropriée du procédé, elles ont tendance à être coûteuses en ressources informatiques. Cela limite leur utilisation dans des cas concrets, en particulier pour des études d'optimisation du procédé. L'approche pseudo inverse (API), développée dans le contexte du forgeage à froid 2D axisymétrique, fournit une estimation rapide des champs de contrainte et de déformation dans le produit final pour une forme initiale donnée. Dans ce travail, l'API est étendue pour inclure les effets thermiques et viscoplastiques dans le procédé de forgeage ainsi que dans le cas général 3D. Les résultats sont comparés aux codes commerciaux disponibles basés sur les approches classiques pour montrer l'efficacité et les limites de l'API. Les résultats obtenus indiquent que l'API est un outil assez efficace pouvant être utilisé à la fois pour des simulations 2D et 3D du forgeage à chaud.

Thermo-viscoplastic numerical modeling of metal forging process by the Pseudo Inverse Approach

Hot forging is a metal forming process used to form difficult-to-form materials as well as to achieve complex geometries. The reduction of yield stress at high temperatures and a subsequent increase in formability is the primary mechanism that drives the process. Numerical methods provide an efficient means to predict the material yield and the stress/strain states of the product at different stages of forming. Although classical methods are accurate enough to provide a suitable representation of the process, they tend to be computationally expensive. This limits its use in practical cases especially for process optimization. Pseudo Inverse Approach (PIA) developed in the context of 2D axisymmetric cold forming, provides a quick estimate of the stress and strain fields in the final product for a given initial shape. In this work, the PIA is extended to include the thermal and viscoplastic effects on the forging pro-

cess as well as to the general 3D case. The results are compared with commercially available software based on the classical approaches, to show the efficiency and the limitations of PIA. The results obtained indicate that PIA is a quite effective tool that can be used for both 2D and 3D simulations of hot forging.

Contents

1	INTRODUCTION	11
1.1	Metal Forging	12
1.1.1	Forging Equipment	16
1.1.2	Cold forging, Hot forging & Warm forging	17
1.1.3	Types of Forging Operations	18
1.2	Processes and Challenges	20
1.3	Numerical Simulation of Forging Process	22
1.3.1	Direct Method	24
1.3.2	Inverse Method	26
1.3.3	Pseudo Inverse Method	26
2	METAL FORMING PROCESS ANALYSIS	29
2.1	Mathematical Description	31
2.1.1	Field Equations & Weak Form - Mechanical Equilibrium	32
2.1.2	Mathematical Preliminaries - Nonlinear Analysis	35
2.1.3	Incremental Deformation Problem	42
2.1.4	Thermodynamics	43
2.1.5	Finite Element Method	45
2.2	Metal Forming Analysis by the Finite Element Method	46
2.2.1	Total Lagrangian and Updated Lagrangian Formulations	46
2.2.2	Drawbacks of the Lagrangian Formulations	48
2.2.3	Inverse Formulations	49
2.2.4	Drawbacks of the Backward Tracing Methods	50
3	PSEUDO INVERSE APPROACH FOR METAL FORMING ANALYSIS	52
3.1	Pseudo Inverse Approach	53
3.1.1	Description of the Method	54
3.1.2	Mathematical Formulation & Finite Element Method	55
3.1.3	FEM Solution of the Coupled Problem	58
3.1.4	Finite deformation Stress updates	60
3.1.5	Thermo-viscoplastic stress updates	63
3.1.6	Solving algorithm (Return Mapping / Direct Scalar Algorithm)	66
3.2	Practical Implementation	69
3.2.1	Generation of intermediate configurations	71
3.2.2	Free surface correction and boundary conditions	72

3.2.3	Co-ordinate transformations	73
4	SIMULATION RESULTS & DISCUSSION	77
4.1	Thermo-viscoplastic models	78
4.2	Simulation Results	79
4.2.1	2D Axisymmetric Screw	79
4.2.2	2D Axisymmetric Wheel	86
4.2.3	3D Upsetting	95
4.2.4	3D Cup	98
4.3	Computation Time	101
5	CONCLUSIONS AND FUTURE PERSPECTIVES	104
5.1	Conclusions	104
5.2	Future Perspectives	106
5.2.1	Optimization and Improvement of the Code	106
5.2.2	Process and Preform Optimization	107
5.2.3	Mesh Optimization	108
5.2.4	Other Applications	110
6	RÉSUMÉ ÉTENDU	112
	REFERENCES	142

List of figures

1.1	Forged crankshaft and sectional view showing the grain orientation [Massivumformung, 2011]	13
1.2	Production percentages of forged products [Massivumformung, 2011]	14
1.3	Major producers of forged components in *1000 tonnes [Massivumformung, 2011]	14
1.4	Types of forging: a) Open-die b)Flash-less c) Impression-die [Groover, 2010]	19
1.5	FEM Simulation of forged parts [Massivumformung, 2011]	23
2.1	The process of finite element analysis[Bathe, 1996]	30
2.2	Forming problem - Definition	32
2.3	General motion of a deformable body [Bonet & Wood, 2008]	37
2.4	Motion of a body[Bathe et al., 1975]	42
3.1	Elastic prediction and return mapping	68
3.2	Flowchart - PIA	70
3.3	Generation of a geometrically proportionate intermediate configuration	72
3.4	Spherical-polar and Cylindrical-polar Coordinates	74
4.1	Forging of a screw a) Target shape b) Initial billet and tools	79
4.2	Reference results obtained from ABAQUS®Explicit- Axisymmetric Screw	81
4.3	Results obtained from PIA - Axisymmetric Screw (15 steps)	81
4.4	Evolution of field values at Node 236 - Axisymmetric Screw. a)Equivalent Plastic Strain b) Von-Mises Stress c) Temperature	82
4.5	Reference results obtained from ABAQUS®Explicit- Axisymmetric screw with Inelastic heat fraction	83
4.6	Results obtained from PIA - Axisymmetric screw with Inelastic heat fraction (30steps)	83
4.7	Results from 80 steps PIA - Axisymmetric Screw with Inelastic heat fraction	84
4.8	Evolution of field values at Node 236 - Axisymmetric Screw including inelastic work. a)Equivalent Plastic Strain b) Von-Mises Stress c) Temperature	85
4.9	Target shape of the wheel	86
4.10	Tools and workpiece used for forging the 2D axisymmetric wheel	87
4.11	Reference results - Axisymmetric Wheel. a) Equivalent Plastic Strain b) Von-Mises Stress c) Temperature	88

4.12	PIA results 25 steps - Axisymmetric Wheel. a) Equivalent Plastic Strain b) Von-Mises Stress c) Temperature	89
4.13	Evolution of field values at node 965 - Equivalent Plastic Strain (PEEQ) . . .	91
4.14	Evolution of field values at node 965- Von-Mises Stress	91
4.15	Evolution of field values at node 965 - Temperature	92
4.16	Shape prediction/correction in PIA	94
4.17	Number of Non-Linear Iterations at each step	94
4.18	Representation of the upsetting process. a) Target shape b) Tools and Initial billet	95
4.19	Upsetting simulation Reference Results - Quarter Model a) Equivalent Plastic Strain b) Von-Mises Stress	96
4.20	Upsetting simulation PIA Results - Quarter Model - 1 Step a) Equivalent Plastic Strain b) Von-Mises Stress	96
4.21	Upsetting simulation PIA Results - Quarter Model - 10 Step a) Equivalent Plastic Strain b) Von-Mises Stress	97
4.22	Evolution of field values at Node 580: Reference vs PIA - 3D Upsetting . . .	98
4.23	3D Cup - a) Target shape b) Tools and Initial billet	99
4.24	3D Cup simulation Reference Results a) Equivalent Plastic Strain b) Von-Mises Stress	100
4.25	3D Cup simulation PIA Results - 20 steps a) Equivalent Plastic Strain b) Von-Mises Stress	100
4.26	Evolution of field values at Node 580: Reference vs PIA - 3D Cup	101
4.27	Computation Time - With Mass Scaling	103
5.1	Overview of the inverse pre-deformation method[Dheeravongkit & Shimada, 2005b]	110
6.1	Evolution des valeurs de champ au noeud 236 - Vis Axisymétrique, travail inélastique compris. a) Déformation plastique équivalente b) Contrainte de Von-Mises c) Température	125
6.2	Résultats de référence - Roue Axisymétrique. a) Déformation plastique équivalente b) Contrainte équivalente de Von-Mises c) Température	127
6.3	Résultats API - Roue Axisymétrique. a) Déformation plastique équivalente b) Contrainte équivalente de Von-Mises c) Température	128
6.4	Evolution des valeurs de champ au noeud 580: Référence vs API - Ecrasement 3D	129

Acknowledgments

At the onset, I would like to offer my sincerest gratitude to my thesis supervisor Pr. Bousad Abbès for his guidance, support and encouragement throughout my PhD. study at the Université de Reims Champagne-Ardenne. His expertise, advice and his human qualities made me enjoy working with him and learn a lot. Without his eminent supervision and the freedom given to pursue my own avenues of thought, this thesis would not have been completed. I would also like to acknowledge the support of my co-advisers Dr. Yu Ming Li and Dr. Fazilay Abbès over the course of my thesis.

I am grateful for the financial support by ESI Group in pursuing this research work and especially to my industrial adviser Dr. Jean-Louis Duval for all the guidance. I would also like to take this opportunity to thank all my colleagues at ESI Group with whom I have had fruitful discussions over the course of my thesis work and also to the IT department for their timely interventions and support. My best regards also to all my former colleagues and industry acquaintances who gave valuable inputs over the course of thesis, especially in terms of how the forging industry works and its needs.

My thanks to my colleagues in GRESPI/ISI for their help and friendship during the course of the past three and a half years. I would like to thank my friends who made me feel at home all around the world, and for becoming a family away from family. A big shout-out to all the friends who stayed by my side through thick and thin and helped me stay sane with their support and encouragement during all the difficult times. A special thanks to Dr. Nicholas Chevaugon who guided me to this particular opportunity in research.

I am grateful for the support of my family, especially my mom, sister, brother-in-law and their kids, and my extended family. You guys are amazing. This thesis would not have been completed without the words of encouragement and support from my better half. Thank you for being the light at the end of the tunnel

Last but not the least, a word of thanks to God almighty for all the timely guidance and respite in times of trouble.

To my Dad, for the guiding light he has been all throughout the years

To Sam Uncle, for lighting the fire of being a researcher

and to Vinodchan, for opening up the way

Imagination is more important than knowledge. Imagination is the language of the soul. Pay attention to your imagination and you will discover all you need to be fulfilled

Albert Einstein

1

Introduction

One of the major milestones in the history of mankind was the discovery of metals and metal-working to produce tools that had better mechanical properties and complex shapes in comparison with tools made of stone and/or wood. Metal working techniques still continue to be one of the bedrocks of the industrial world and aid in the production of components for a variety of purposes. The metal working techniques available today can be broadly classified into four: forming, cutting, joining and additive manufacturing. Of these, metal forming refers to a group of manufacturing methods by which a given workpiece, usually shapeless or of a simple geometry, is transformed through plastic deformation into a useful part having a complex geometry. It has a special place among other manufacturing processes since it helps to produce parts having superior mechanical properties with minimum material wastage. But, metal forming generally requires expensive tooling and is economically attractive only when a large number of parts must be produced and/or when the mechanical properties required in the finished product can only be obtained by a forming process.

1.1 METAL FORGING

Based upon the size and shape of the workpiece and how the size and shape is changed, metal forming operations can be broadly classified into two major types: Bulk forming operations and Sheet-forming operations [Black & Kohser, 2011]. Bulk forming operations generally include those that involve a significant change in thickness, cross-sections or shapes. Since the volume of the workpiece remains more-or-less constant, changes in one dimension requires a proportionate change in the other directions. Thus, the surface area of the workpiece changes significantly, often increasing as the product gets lengthened or the shape becomes more complex. In contrast, sheet-forming operations involve material deformation in which the surface area and thickness remain relatively constant. Bulk forming operations can be generally performed in all temperature regimes whereas most sheet-forming operations are performed cold since the sheet material tends to lose heat rapidly due to the large surface-to-volume ratio. Advances in the sheet-forming technology has given rise to hot-stamping operations that can produces parts with more complex shapes and strength as compared to cold-forming operations. Hot stamping was developed in the 1970's in Sweden and patented (SE7315058-3, 1973; GB1490535, 1977) [Plannja, 1973, 1977] by a Swedish company (Plannja), that used the process for saw blades and lawn mower blades [Karbasian & Tekkaya, 2010]. Nowadays, hot-stamping is an integral part of the automotive industry with its focus on producing lightweight parts that have high strength capabilities (AHSS and UHSS [Wankhede & Lehn, 2017]).

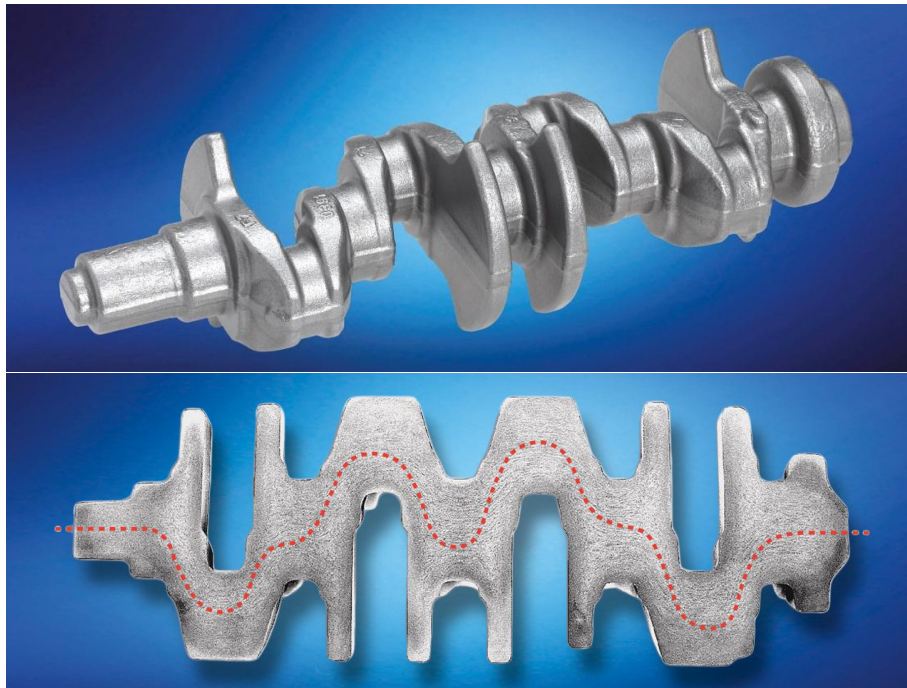


Figure 1.1: Forged crankshaft and sectional view showing the grain orientation [Massivumformung, 2011]

Forging, is considered to be one of the oldest metal working operations and, based upon the earliest written records of mankind, can be dated back to around 5000 BCE [Groover, 2010]. It is a bulk deformation process in which the work piece is compressed between two dies, using either impact or gradual pressure to form a desired shape. Today, forging is an important industrial process used to make a variety of high-strength components with a better strength-to-weight ratio than those obtained by other manufacturing operations like casting or welding/fabrication. This gain in strength is mainly due to plastic hardening and a favourable grain orientation during the forming process. An example of a forged part along with its sectional view showing the grain orientation can be seen in Fig (1.1). The automotive sector along with tier-1 system suppliers, account for more than 80% of the total forgings production. The percentage of forged parts delivered by the German industry in 2009 can be seen in Fig (1.2). Additionally, many industries use forging to establish the basic form of large components that are subsequently machined to final shape and dimensions. The world-wide

production of drop-forged products can be seen in Fig (1.3).

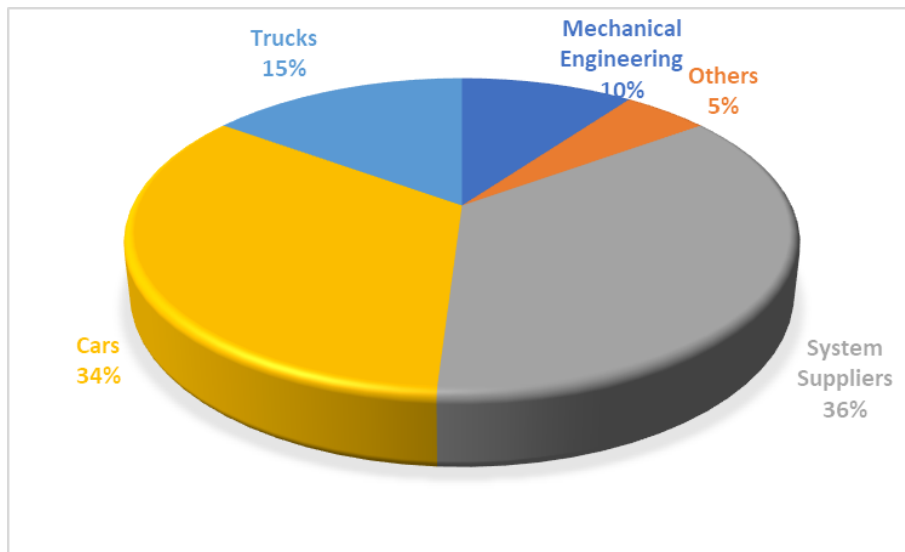


Figure 1.2: Production percentages of forged products [Massivumformung, 2011]

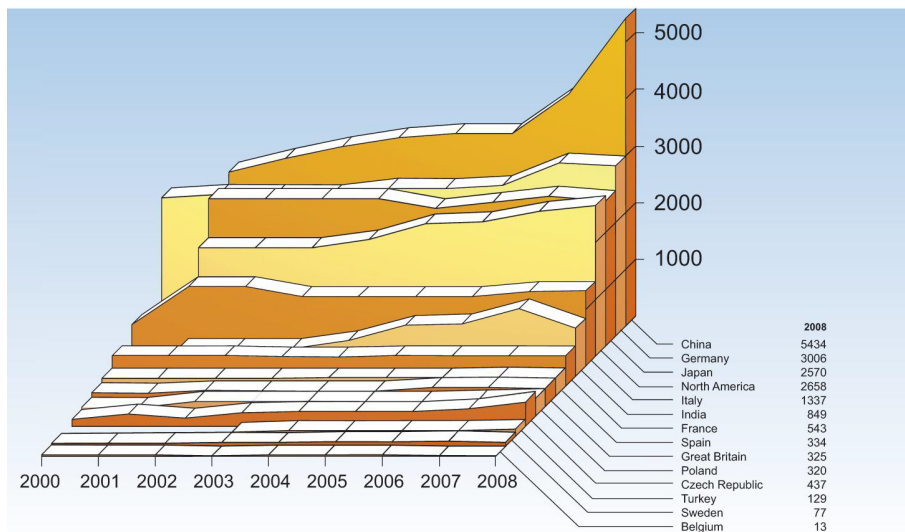


Figure 1.3: Major producers of forged components in *1000 tonnes [Massivumformung, 2011]

Parts that are usually produced by forging process are used in various industries [FIA, 2019] such as:

AUTOMOTIVE & TRUCK Forged components are commonly found at points of shock and stress such as wheel spindles, kingpins, axle beams and shafts, torsion bars, ball studs, idler arms, pitman arms and steering arms. Another common application is in the power-train, where connecting rods, transmission shafts and gears, differential gears, drive shafts, clutch hubs and universal joints are often forged. Although typically forged from carbon or alloy steel, other materials such as aluminum and micro-alloyed steels are seeing great advances in forged auto and truck applications.

AEROSPACE Forged components used in the aerospace industry include bulkheads, wing roots and spars, hinges, engine mounts, brackets, beams, shafts, landing gear cylinders and struts, wheels, brake carriers and discs and arresting hooks. In jet turbine engines, iron-based, nickel-based and cobalt-based super-alloys are forged into components such as discs, blades, buckets, couplings, manifolds, rings, chambers and shafts.

AGRICULTURAL MACHINERY, OFF-HIGHWAY EQUIPMENT In addition to engine and transmission components, key forgings subjected to impact and fatigue range from gears, shafts, levers and spindles to tie-rod ends, spike harrow teeth and cultivator shafts. Forgings are also used for a wide variety of ball joints, wheel hubs, rollers, yokes, axle beams, bearing holders and links.

GENERAL INDUSTRIAL EQUIPMENT Large-size forgings are often found in industrial equipment and machinery used by the steel, textile, paper, power generation and transmission, chemical and refinery industries, valves and oil field applications to name just a few. Typical forged configurations include bars, blanks, blocks, connecting rods, cylinders, discs, elbows, rings, shafts and sleeves.

1.1.1 FORGING EQUIPMENT

In the olden days component forging was done by a blacksmith using a hammer and anvil. The quality of the parts produced and the final shape achieved depended on the skill level of the blacksmith. Over the centuries, the smith or the forge has evolved to become a modern facility with engineered processes and production equipment. Industrial forging nowadays is carried out with the help of mechanical/hydraulic presses or hammers with reciprocating weights.

Hammers operate by applying an impact load on the work piece. In this case, the upper portion of the forging die is attached to the ram and the lower portion is attached to the anvil. The workpiece is placed on the lower die and the impact energy from lifting and dropping the ram causes the work piece to assume the form of the die cavity. In practice, several blows of the hammer is often required to achieve the desired shape. Drop hammers are most frequently used for impression-die forgings. In this type of impact forging the speeds are high and hence the forming time is short. Contact times between the work piece and the dies are on the order of milliseconds and this helps in minimizing the heat transfer and the subsequent cooling of the workpiece. However, one of the disadvantages of drop hammers is that a large amount of the impact energy can be dissipated by deformation of just the surface of the metal and through absorption by the anvil and the foundation.

In the case of forging presses the force is given gradually by means of the translation motion of the ram, rather than through a sudden impact, to obtain the required final part. The presses are generally able to achieve very high forging forces while also providing a more constant force throughout the stroke. The deformation is analyzed in terms of the forging forces and the slower action produces a more uniform deformation and flow. This also makes them suitable for forming operations of large/thick pieces. However, because of the longer contact time between the dies and the workpiece, there is higher cooling of the workpiece which causes it to become less ductile and can lead to cracking of the workpiece. This problem is mitigated to a certain extent through the use of heated dies and periodic re-heating of the

workpiece which enables the production of finer details and closer tolerances.

1.1.2 COLD FORGING, HOT FORGING & WARM FORGING

Low yield strength and high ductility, which are affected by temperature and the rate of deformation (strain rate), are desirable material properties for the workpiece material used in forging applications. The effect of temperature gives rise to distinctions among cold forging, warm forging and hot forging[Black & Kohser, 2011].

Cold forging is the forging process in which the workpiece is initially kept at or around the room temperature. Cold forging is accompanied by work hardening / strain hardening which imparts higher strength while lowering the ductility of the material. This results in higher forging forces while producing parts with higher strength to weight ratio. Cold forging produces parts with a high degree of dimensional accuracy (near net-shape), high surface quality, good repeatability and a very high degree of material utilization. The parts obtained are free from scaling and no heating is necessary but, higher tool forces are required. The loss of ductility also leads to difficulty in realizing complex shapes. Hence cold forging is suitable for the manufacture of a large number of precision manufactured small parts.

In the case of hot forging, the workpiece is heated to above the re-crystallization temperature (above 50% of the melting temperature of the material). The workpiece exhibits a high formability because of a reduction in the flow stress owing to the higher temperatures. Since the workpiece is kept above the re-crystallization temperature throughout the process, there is no strain hardening. During hot forging, the workpiece can undergo larger plastic deformation (larger strain rates and true strains) and complex shapes can be realized more easily. Parts produced by hot forging exhibit poor surface quality, higher wastage of material and poor dimensional accuracy due to scaling and shrinkage. The higher temperatures of the workpiece also increases the tool wear due to thermal degradation. Scaling defects are noticed on the workpiece and care needs to be taken during cooling to avoid warping.

In Warm forging, the workpiece is heated to above room temperature but below the re-

crystallization temperature (30% to 50% of the melting temperature of the material). It is a compromise between hot and cold forging and incorporates the advantages from both types. The workpiece exhibits a higher level of formability and requires lower forging forces when compared with cold forging due to the higher temperatures, while the lower temperatures when compared with hot forging helps in reducing tool wear. The high cost involved for the tooling and the machinery makes this kind of a process suitable only for the production of large batches of parts having complex shapes, especially in the automotive industry.

1.1.3 TYPES OF FORGING OPERATIONS

Forging operations have evolved over the years from the basic shaping operations in the smithy to complex operations capable of producing complex shapes that have a very high strength. Based on the extent to which the flow of the work metal is constrained by the dies, forging operations can be classified into mainly three types: Open-die forging, Impression-die forging and Flash-less/Precision forging. A schematic representation of the 3 different types of forging operations can be seen in Fig (1.4). The classifications almost follow the development of the forging process from forging simple shapes to forging complex shapes with fine tolerances.

Open-die hammer forging can be considered to be the modern industrialized equivalent of the forging done by the blacksmith of the olden times. In open-die forging, the workpiece is compressed between two flat (or almost flat) dies which allow the metal to flow without any constraints in a lateral direction relative to the dies. Since open-die forging does not fully control the flow of metal, the operator must re-orient and position the workpiece between the blows to obtain the desired shape. This makes it a slower operation where the shape and dimensional precision of the workpiece are dependent on the skill of the operator. While some finished parts can be made by this technique, open-die forging is generally used to pre-shape the workpiece for further operations.

Impression-die forging, also known as closed-die forging, overcomes the difficulties asso-

ciated with open-die forgings by the use of shaped dies to control the flow of metal. It is performed with dies that contain the inverse shape of the desired part. As the die closes to its final position, flash is formed by metal that flows beyond the die cavity and into the gap between the die plates. Usually, several forming steps are required in impression-die forging to transform the starting blank into the desired final geometry. Because of flash formation and the more complex parts made, forging forces in this process are significantly higher and more difficult to analyze than in open-die forging. However, impression-die forging is not capable of close-tolerance work and machining is often required before the component can be used in the final assembly. The basic geometry of the part is obtained from the forging process and then machining is performed on those portions of the part that require precision finishing.

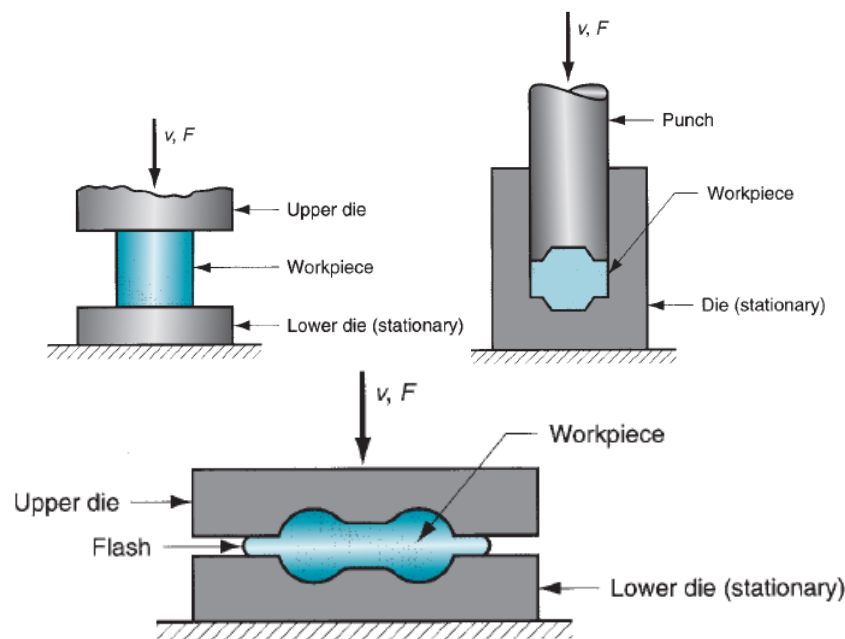


Figure 1.4: Types of forging: a) Open-die b) Flash-less c) Impression-die [Groover, 2010]

Improvements in impression-die forging technology has resulted in the capability to produce forgings with closer tolerances and the virtual elimination of machining allowances and flash. Forging processes with these features are known as precision forging. This process

produces very little to no flash and is often referred to as near net shape forgings. The principal distinction between Impression-die forging and a true closed-die forging is that in a true closed-die forging, the workpiece is completely contained within the die cavity during the process and no flash is formed. This is why it is appropriately called as flash-less forging. Flash-less forging imposes a more stringent set of requirements on process control than impression-die forging. The work volume must be equal to the space in the die cavity within a very close tolerance. If the initial workpiece is too large, excessive pressure can cause damage to the die or press. If the blank is too small, then it would result in under-filling of the die cavity.

1.2 PROCESSES AND CHALLENGES

Even though forging has been one of the oldest metalworking processes to be discovered, its development over the years has not been without challenges. The process still remains highly dependent on operator/process designer know-how and skills due to a variety of factors. It is a complex process and the physical phenomena describing a forging operation are difficult to express with quantitative relationships. The accuracy of the forging process is affected by many variables and can be classified into three main groups as shown in Table (1.1).

Before Forging	During Forging	After Forging
Workpiece material, size & shape	Workpiece temperature	Trimming
Die deformation, accuracy and surface	Flow stress	Heat treatment
Die setting accuracy	Scaling, shrinkage	Cooling process
Die design	Billet / preform volume	Cleaning process
Forging sequence	Lubrication	Sizing
Type of forging machine	Die temperature and wear	Finish machining

Table 1.1: Variables influencing accuracy of forgings Douglas & Kuhlmann [2000]

For the design of the forging process and the sequence of operations, a prediction of the variables associated with the process such as temperature and flow stress needs to be made.

The forces required for the forging operation and the resulting stresses are tied to the material properties, including the grain size evolution and the local temperature of the workpiece, and cannot be accurately predicted using simple formulae. Since the production of discrete parts is often a multi-step process, the metal flow, friction at the tool/material interface, heat generation and transfer and the relationships between micro-structure/properties and process conditions are difficult to predict and analyze. Consequently a numerical analysis needs to be done for the prediction of these essential variables and the most significant objective of any analysis is to assist in the design of forging and preforming sequences. Such design essentially consists of

- establishing the kinematic relationships (shape, velocities, strain rates, strains) between the deformed and the undeformed configurations (i.e. the metal flow)
- establishing the limits of formability i.e. determining whether it is possible to form the part without surface or internal failure
- predicting the forces and stresses necessary to execute the forging operation so that the tooling and equipment can be designed or selected. [Altan, 1983]
- minimizing the material wastage as flash and trimmings
- improving the cost-effectiveness of forged parts

Due to its high strength-to-weight ratio and better fatigue strength, forgings have traditionally found use in automotive and aerospace applications. However, recent advances in other traditional production techniques and the advent of newer production techniques such as additive manufacturing have put pressure on the forging industry to reduce costs while also being able to produce forged parts with higher shape complexity. The production of complex 3D geometries requires hot-forging with the use of impression-dies and can only be done in multiple stages to avoid cracking of the material. Flash is an integral part of these operations, but results in a low material yield and hence greater material wastage and higher costs

of production. The material yield [Simufact, 2019] can be defined as

$$\text{material yield \%} = \frac{\text{Raw part wt}}{\text{Input part wt}} * 100$$

and in a typical industrial forging operation, the material yield ranges from 60% to 80% depending on the complexity of the component family. This makes precision / near net-shape hot forging an attractive option for the forging industry. Precision hot forging can reduce costs by :

- reducing material usage by 10% - 30%
- eliminating trimming in flash-less forging
- reducing energy consumption due to the lower heating temperatures
- simplifying post-forge cleaning due to reduced oxidation and scale.
- eliminating some post forge process operations like normalizing
- substantially reducing downstream machining operations

In addition, the optimal grain flow can improve the material strength in critical areas. Since material costs amount to almost 50% of the forging cost, any material savings can greatly impact the cost-competitiveness of the forged part. Even accounting for the additional costs associated with precision hot forging, there is potential to supply a product with higher quality at a lower cost [Douglas & Kuhlmann, 2000].

1.3 NUMERICAL SIMULATION OF FORGING PROCESS

Numerical simulation techniques are an indispensable tool for the optimum selection of the process conditions, conditions and shape of the initial workpiece and some restrictions on the processes. Numerical simulations of the metal forging process helps to:

- reduce development lead times and minimize the number of experimental trials required



Figure 1.5: FEM Simulation of forged parts [Massivumformung, 2011]

- reduce development costs, particularly those incurred by the manufacture of expensive dies for experimental trials [Rowe et al., 2005]

Earliest efforts in this regard came in the form of numerical equations for simple geometries and empirical relations to extrapolate it to more complicated shapes. Even though it was useful in gaining a general insight about the process, they had limited practical applications. The advent of the Finite Element Method (FEM) and the considerable developments in the field of FEM made it possible to analyze more complicated shapes and configurations and give a satisfactory prediction about the tool forces and metal flow. The application of FEM to metal forming was a direct consequence of the extension of FEM to non-linear elasto-plastic analysis started by Argyris [Argyris, 1965], Pope [Pope, 1966], Marcal & King [Marcal & King, 1967], Yamada et al. [Yamada et al., 1968] and Zienkiewicz et al. [Zienkiewicz et al., 1969]. A comprehensive survey of the literature related to the analysis of metal forming processes using large deformation elasto-plastic formulations including unilateral contact and friction has

been given by Cheng & Kikuchi [Cheng & Kikuchi, 1985], Mackerle [Mackerle, 2006] and Hartley & Pillinger [Hartley & Pillinger, 2006]. An example of an automotive part made out of aluminium and optimised using FEM methods can be seen in Fig (1.5) and clearly shows the stressed zones in the part under two designs of an optimization study.

Software solutions based on the Finite Element Method are available in the market for use in industrial cases, but there is still a huge avenue open for their improvement. The requirements of the industry that still need to be met by the available software can be listed mainly as:

- improved accuracy of simulation results
- mathematical modelling of the interaction between the tool and the machine
- simulation of the entire process chain involved in the production of a forged part and coupling between various simulations
- prediction of components properties based upon the evolution of the micro-structure of the part
- minimization of computing time
- automatic optimization of manufacturing concepts.

1.3.1 DIRECT METHOD

The development of the FEM in the 1960's lead to the direct modelling approach in which the deformation process is posed as boundary-value problem. In this, the process conditions, boundary conditions and shape of the initial work piece are chosen either arbitrarily or based upon certain thumb-rules. The subsequent deformation and stress-state of the workpiece under the applied load, surface displacement and process conditions is computed by the FE method. The developments in the 60's and 70's were limited to two dimensional approximations and practical applications were limited due to the limited performance of computers

available at that time. 3D computations were developed in the 80's in research labs with the contributions of Park & Kobayashi[[Park & Kobayashi, 1984](#)], Surdon & Chenot[[Surdon & Chenot, 1987](#)] etc. But it was only in the 90's, with the development of commercial codes for metal forming such as FORGE[®]NxT, DEFORM-2D/3D, Simufact forming and QFORM VX that real industrial examples could be run[[Soyris et al., 1992](#), [Chenot, 1998](#)]. With the developments in the numerical solution of thermo-mechanically coupled problems and elastoviscoplasticity, this technique has proved to be very useful in predicting the shape of the final workpiece produced by the forging process and also in detecting defects like under-fill and folding in the workpiece. Recent developments in the field, including the use of parallel codes for solution and the incorporation of micro-structural level data for the material modelling, has made the direct modelling of great use for simulation of the forming process. Still, it is a computationally intensive process due to the inherent non-linearity of the material properties, the geometrical non-linearity associated with large deformations and the coupled thermo-mechanics.

One of the most important aspects of a closed die forging operation is the design of the preforms at various stages. Even though the direct modelling is mature enough to handle the complexities of the material forming process, it has one major disadvantage when it comes to the optimization of a forging process due to the semi-arbitrary choice of the initial conditions and shape of the workpiece and process conditions. Even though shape optimisation methods for the preform design has been proposed by different methods[[Fourment & Chenot, 1996](#), [Fourment et al., 1996](#), [Yang & Ngaile, 2009](#)], the optimal preform shapes and process conditions can only be found out by repeated direct modelling on all the different initial shapes and process conditions available. This places a huge computational burden, especially in the case of optimisation of complex 3D shapes due to the high computational effort required for the direct modelling of each proposed preform shape. Although recently, meta-model assisted methods[[Ejday & Fourment, 2010](#)] and neural network[[Ciancio et al., 2015](#), [D'Addona & Antonelli, 2018](#)] based optimization techniques have been proposed to

reduce the number of direct modelling computations required, practical applications at an industrial level has been limited.

1.3.2 INVERSE METHOD

To find out the optimal preform shape needed to obtain the required final shape, an original process called “Backward Tracing Method” was developed in the 80’s by Park et al. [Park et al., 1983] and was later developed by others. The method essentially consists of tracing the loading path in the actual forming process backward from a given final configuration, using the finite element method. Although this method represents an improvement over the trial-and-error design methodology employed in shape optimization techniques, the simulation of reverse material flow is a fictitious construct and cannot lead to physically realistic design solutions especially when thermal effects are also present. This is evidenced by the fact that the inverse modelling cannot take into account the accumulated plastic strain/work hardening and even though the preform shapes predicted by the inverse analysis is close to the optimal preform shapes, they provide a poor prediction of the stress state of the workpiece. Since, the inverse methods lead to a poor prediction of stresses but a good prediction of the preform shapes, Guo et al. [Guo et al., 1990] developed a single-step inverse modelling method in the context of sheet metal forming called the “Inverse Approach” for predicting the undeformed workpiece shapes. This was later extended to the case of axisymmetrical cold forging [Halouani et al., 2010, 2011d, Ali Halouani & Guo, 2010, Halouani et al., 2011a] and was found to be a good tool for predicting the strains but not good enough for the prediction of the stresses.

1.3.3 PSEUDO INVERSE METHOD

Since the optimisation of the preform takes into account several parameters including die filling, damage in the workpiece and the tool forces, it is important to develop a tool that can quickly and accurately predict the preform shape as well as the deformed shape and the

stresses in the workpiece after deformation. A first-step in this regard came with the Pseudo-Inverse Approach (PIA) developed for sheet metal forming [Gati et al., 2003, Guo et al., 2004]. This was later extended to the case of 2D axisymmetrical cold forging [Halouani et al., 2011c, 2012b, 2011b]. PIA essentially consisted of the prediction of an intermediate shape by using the information about the target shape and the undeformed shape predicted by a simple inverse approach to speed-up the computations. The stress and strain history is then computed by following an inverse approach between two successive configurations. A similar approach has also been followed in sheet-metal forming [Liu et al., 2017] where the intermediate configurations are predicted by a pseudo minimum approach (PMA)

This present work extends the PIA developed in the case of axisymmetrical cold forging to warm and hot forging applications by including the thermo-viscoplastic effects and also to the full three-dimensional forging case. It was observed during the computations that a better strain/stress estimation is obtained by employing a direct computation between intermediate configurations rather than an inverse computation. This helps in better computation of the accumulated strain and better overall prediction of the deformed shape and the stress-state at the end of deformation. The method also makes use of the Direct Scalar Algorithm developed for plastic integration [Li et al., 2007, Halouani et al., 2015] and extends the same to viscoplasticity in a straight-forward manner without incurring any additional computational effort. Thus the main objectives of this dissertation can be described as follows:

Postulate an alternative simulation method for 2D and 3D hot, cold and warm forging applications that

- Reduces the simulation time required for simulation of the forging process by virtue of the mathematical model being used
- Delivers a comparable accuracy to existing numerical analysis methods
- Can be easily used by designers for the optimisation of preforms and tools

The dissertation is arranged in the following manner. The first chapter introduces the forging process and the needs of the industry. It details the progression of the works in the field of

numerical simulation of forging and the needs of the industry in the present age and details the need for the development of a robust and quick simulation procedure for the efficient and optimal design of preforms.

The second chapter deals with the mathematical preliminaries associated with the simulation of forging process. A concise description of the large-deformation continuum mechanics is presented and a brief description of the Finite Element Method in the context of metal forming analysis is done. The advantages and disadvantages of the direct method and the inverse method are also briefly discussed.

The third chapter talks about the PIA and the implementation of PIA in a general thermo-viscoplastic analysis. The implementation features are discussed for both the 2D axisymmetrical and the general 3D case. Algorithms are presented and the similarities and differences between PIA and other methods are highlighted.

The fourth chapter presents the results of numerical simulations and compares the results obtained from PIA with those obtained by commercially available software. Examples are presented from both 2D axisymmetrical analysis of hot forgings and general 3D analysis of warm-forgings. The computational efficiency and accuracy of results obtained from PIA is compared with that of the results obtained from commercially available software.

The fifth and final chapter concludes the dissertation with a discussion on the results and the salient points of the Pseudo Inverse Approach. A discussion on the general perspectives for the method including improvements required and applications outside of metal forming where it maybe employed is briefly discussed.

Modern physics has taught us that the nature of any system cannot be discovered by dividing it into its component parts and studying each part by itself. We must keep our attention fixed on the whole and on the interconnection between the parts

Max Karl Ernst Ludwig Planck

2

Metal Forming Process Analysis

It was with the development of the Finite Element Method that the analysis of complex forming processes became possible in a realistic fashion. The large deformation continuum mechanics analysis has played a huge role in helping designers to predict the deformed shape of the workpiece, the stresses in the die and the workpiece, defects in the workpiece during forging operations like folding, lapping and crack formations, effects of temperature etc. In this chapter, we present a basic description of the mathematical preliminaries involved in the continuum mechanics description of the FEM solution of the metal forming process.

The Finite Element Method is used in engineering analysis and design to solve physical problems which involve a structure or a component subjected to certain loads and displacement conditions. This idealization of the physical problem to a mathematical model requires certain assumptions that lead to the differential equations governing the mathematical model. The finite element analysis solves this mathematical model until a sufficient accuracy level is

obtained.

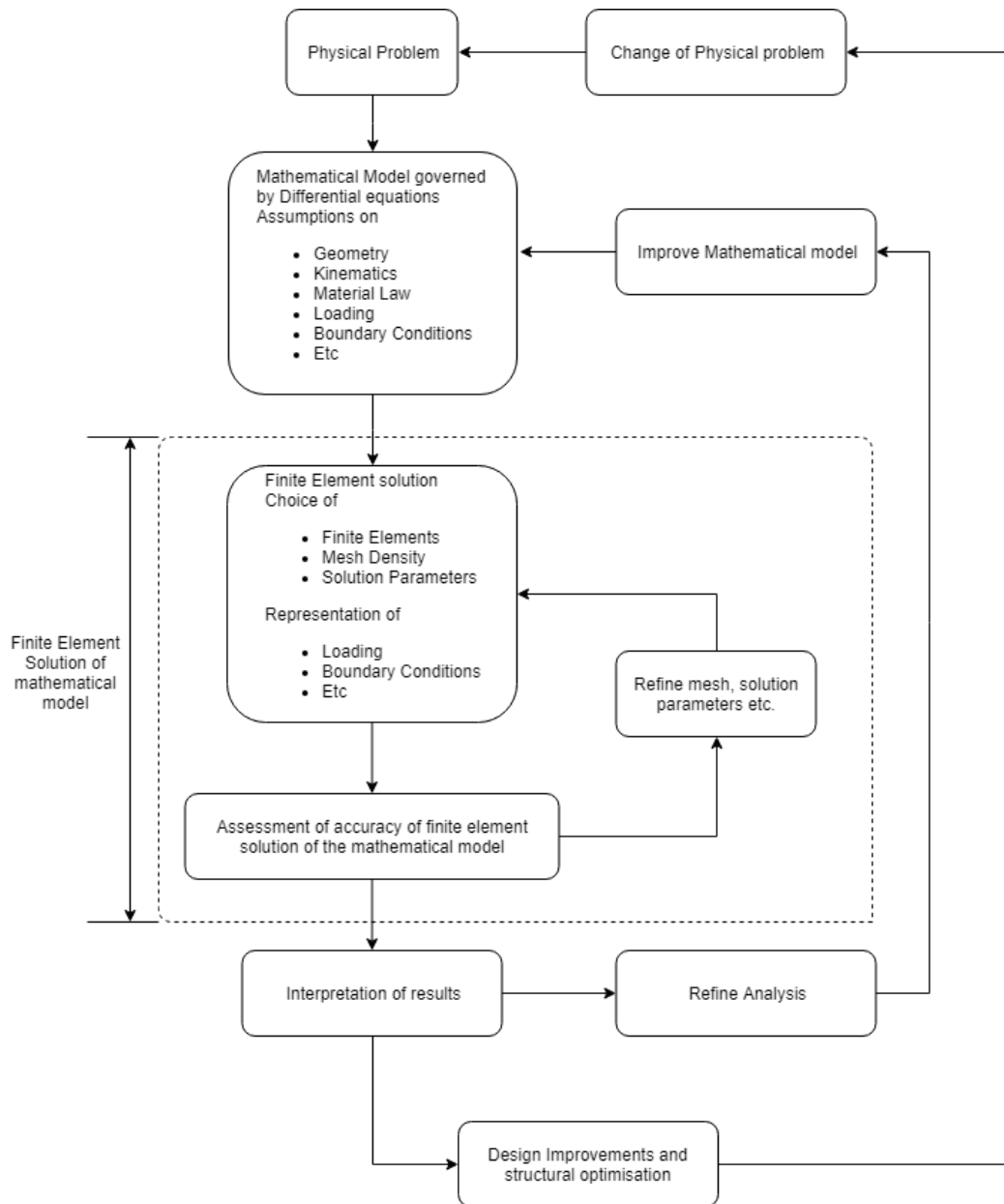


Figure 2.1: The process of finite element analysis[Bathe, 1996]

The finite element solution will only solve the mathematical model and all the assumptions made in this model will be reflected in the predicted response. One cannot expect any more information in the predicted response than the one contained in the underlying mathematical

model. Hence the choice of an appropriate mathematical model is crucial for getting insight into the actual physical problem that we are trying to analyze. It is important to note that we cannot predict the response of the physical problem exactly because, even in the most refined mathematical models, it is impossible to reproduce all the information that is present in nature and therefore contained in the physical problem [Bathe, 1996]. The Finite Element Analysis process maybe described succinctly by the flowchart given in Fig (2.1).

2.1 MATHEMATICAL DESCRIPTION

Since forging involves the shaping of a workpiece using plastic deformation, a plasticity analysis is required to make a satisfactory prediction about the process characteristics. A general description of the metal forming can be given by a continuum description if we ignore the microscopic effects and voids in the workpiece. This analysis, though not perfect, can give an useful insight into the metal forming process using empirical relations for the macroscopic material behaviour and is thus widely used in practice. Extensive studies on finite element analysis of finite strain problems were conducted in the 1960's, but it was not until Oden [Oden, 1969] that complete incremental forms, where the variations in loading and finite rotations were properly considered, were obtained from a nonlinear continuum mechanics description. The first elasto-plastic formulation suitable for large strain and large displacement were presented by Hibbit, Marcal & Rice [Hibbitt et al., 1970] using a Total Lagrangian approach with an additional "initial stiffness" matrix that was missed in small strain formulations. Later, McMeeking & Rice [McMeeking & Rice, 1975] developed an Eulerian type formulation based on the principle of virtual work where the updated finite element mesh was used as a reference configuration. A similar approach was followed by Bathe et al. [Bathe et al., 1975] and was named as the Updated Lagrangian approach. A summary of the advances in mathematical modelling of the metal forming process can be found in Cheng & Kikuchi [Cheng & Kikuchi, 1985], Mackerle [Mackerle, 2006] and Hartley & Pillinger [Hartley & Pillinger, 2006].

2.1.1 FIELD EQUATIONS & WEAK FORM - MECHANICAL EQUILIBRIUM

The simplest explanation of the forging process can be made as the deformation of a body in between a pair or more of dies as shown in Fig (2.2)[Fourment & Chenot, 1996].

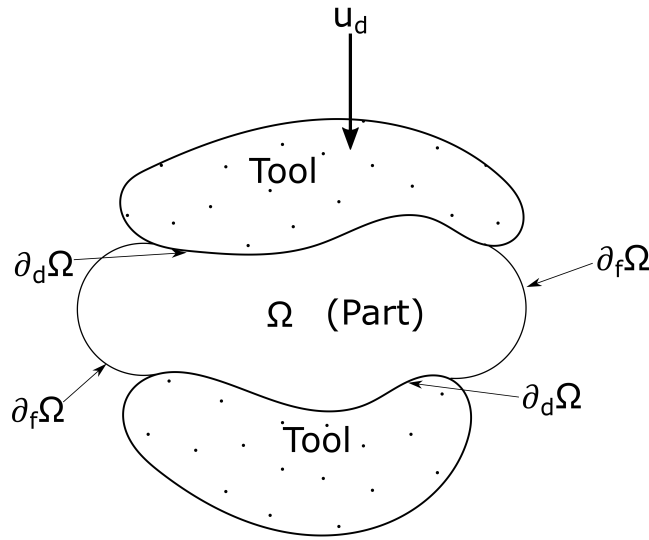


Figure 2.2: Forging problem - Definition

The body can be defined on the domain Ω with boundary $\partial\Omega$ such that $\partial_d\Omega$ is the part of the boundary in contact with the die and $\partial_f\Omega$ is the free surface. Neglecting the inertia forces, the quasi-static equilibrium of the domain at any time t can be expressed as,

$$\begin{aligned}
 \operatorname{div}\boldsymbol{\sigma} + \rho\mathbf{b} &= 0 \quad \text{in } \Omega \\
 (\mathbf{u} - \mathbf{u}_g) \cdot \mathbf{n} &= 0 \quad \text{on } \partial_d\Omega \\
 \boldsymbol{\sigma}\mathbf{n} &= \mathbf{t} = 0 \quad \text{on } \partial_f\Omega
 \end{aligned} \tag{2.1}$$

where $\boldsymbol{\sigma}$ is the Cauchy stress tensor defined in the deformed configuration Ω , \mathbf{b} is the body

force vector, \mathbf{u} is the displacement vector, \mathbf{u}_g is the given displacement of the tool on the boundary $\partial_d\Omega$ and \mathbf{t} is the traction vector prescribed on the surface $\partial_f\Omega$ with \mathbf{n} being an outward unit normal vector to the surface.

By using the principle of virtual work and Green's divergence theorem, Eq. (2.1) can be stated in the weak form as:

$$\int_{\Omega} \boldsymbol{\sigma} : \nabla \mathbf{u}^* d\Omega - \int_{\Omega} \rho \mathbf{b} \cdot \mathbf{u}^* d\Omega = 0 \quad (2.2)$$

for every arbitrary kinematically admissible \mathbf{u}^* such that $\mathbf{u}^* = 0$ on $\partial_d\Omega$.

Using the symmetry property of the Cauchy stress tensor ($\boldsymbol{\sigma} = \boldsymbol{\sigma}^T$) given by the principle of conservation of angular momentum, Eq. (2.2) can also be expressed as:

$$\int_{\Omega} \boldsymbol{\sigma} : \boldsymbol{\varepsilon}^* d\Omega - \int_{\Omega} \rho \mathbf{b} \cdot \mathbf{u}^* d\Omega = 0 \quad (2.3)$$

where $\boldsymbol{\varepsilon}^* = \frac{1}{2} (\nabla \mathbf{u}^* + \nabla \mathbf{u}^{*T})$ is the infinitesimal (virtual) strain.

INCOMPRESSIBILITY

The principle of conservation of mass states that if the density of the domain remains constant, then

$$\text{div} \mathbf{u} = 0 \quad (2.4)$$

This divergence free behaviour of the domain can be considered to be an incompressibility constraint that can be modeled by stating that, the volume changes during deformation should be equal to zero or that the volumetric strains have to be equal to zero. In other words, incompressibility poses a restriction on the admissible modes of deformation and a way of incorporating such divergence free behaviour must be included in the development of an appropriate formulation. Several alternatives have been proposed in the literature [Jinka & Lewis, 1994] and amongst these, the predominant ones are the *Lagrange Multiplier method*,

Mixed Formulation and Penalty Formulation.

The Lagrange Multiplier method [Fosdick & Royer-Carfagni, 1999] removes the incompressibility constraint on admissible displacement fields by introducing a Lagrange multiplier λ and modifying the weak form in Eq. (2.3) to a constrained variational problem of the type in [Washizu, 1974] such that for any kinematically admissible displacement \mathbf{u}^* ,

$$\int_{\Omega} \boldsymbol{\sigma} : \nabla \mathbf{u}^* d\Omega - \int_{\Omega} \lambda \operatorname{div} \mathbf{u}^* d\Omega - \int_{\Omega} \rho \mathbf{b} \cdot \mathbf{u}^* d\Omega = 0$$

and for any arbitrary Lagrange multiplier λ^* ,

$$\int_{\Omega} \lambda^* \operatorname{div} \mathbf{u} d\Omega = 0$$

The Mixed formulation to deal with incompressibility in the context of a variational problem was first discussed by [Herrmann, 1965]. In this $\mathbf{u} - p$ formulation, the variables are the displacement with an associated Lagrange multiplier identified as the mean stress (pressure). The finite element approximation in this case requires independent interpolation of both the pressure and displacement fields and should satisfy the Babuzka_Brezzi conditions [Babuška, 1971, Brezzi, 1974] for non-locking element behaviour.

Both the Lagrange multiplier methods described above suffers from the inconvenience of increasing the number of unknowns to be solved for. The penalty formulation was developed by considering that the problem of minimizing a variational problem subject to constraints can be changed into one of minimizing a modified functional that is free of constraints. This introduces a penalization term K , such that when K is a large positive number, the satisfaction of the constraint is achieved [Zienkiewicz, 1974]. Thus, Eq. (2.3) can be modified to include the incompressibility constraint as,

$$\int_{\Omega} \boldsymbol{\sigma} : \nabla \mathbf{u}^* d\Omega + \int_{\Omega} K \operatorname{div} \mathbf{u} \operatorname{div} \mathbf{u}^* d\Omega - \int_{\Omega} \rho \mathbf{b} \cdot \mathbf{u}^* d\Omega = 0 \quad (2.5)$$

Using the infinitesimal strain tensor introduced in Eq. (2.3), we can express Eq. (2.5) as,

$$\int_{\Omega} \boldsymbol{\sigma} : \boldsymbol{\varepsilon}^* d\Omega + \int_{\Omega} K \varepsilon_v \varepsilon_v^* d\Omega - \int_{\Omega} \rho \mathbf{b} \cdot \mathbf{u}^* d\Omega = 0 \quad (2.6)$$

where ε_v is the volumetric strain given as the trace of the strain tensor and ε_v^* is the virtual volumetric strain. Due to the compactness of this form, we use this form of the mechanical equilibrium equation in the rest of this work.

In the case of penalty formulation, care should be taken to perform reduced integration on the elements as given in [Hughes, 2000] to obtain satisfactory results. For an isotropic material case, K can be easily identified as the Bulk Modulus of the material and the method can be shown to be as equally effective as the methods in which the incompressibility is enforced with the help of Lagrange multipliers.

If the deformation of the body is infinitesimally small, then the deformed configuration Ω can be considered to be essentially the same as the initial stress-free undeformed configuration Ω^0 . Thus, the direct application of Eq. (2.3) is limited to linear problems where the deformation is small and the stress-strain response of the material is linear. When the deformation is finite, Ω is, in general, considerably different from the initial configuration Ω^0 and is one of the unknowns to be determined. Therefore for the analysis of non-linear problems it is advantageous to express Eq. (2.3) in a reference configuration Ω^R and also derive an incremental formulation of the deformation.

2.1.2 MATHEMATICAL PRELIMINARIES - NONLINEAR ANALYSIS

The linear analysis of structural problems using Eq. (2.3) is based upon the assumption that the deformation is small and the stress-strain response is linear. But in a general non-linear analysis, as in the case of a practical metal forming analysis, we encounter finite deformation and also non-linear relations in the stress-strain response. Moreover, if, during loading, the displacement boundary conditions are subject to change (ie, a degree of freedom which was free becomes constrained or vice-versa), the response can be considered linear only prior to

the change in boundary condition. In metal-forming analysis, this is also a source of non-linearity due to the changing contact conditions between the work-piece and the tools.

The basic problem in a general non-linear analysis is to find the state of equilibrium of a body corresponding to the applied loads and configuration at a specified time t . For a materially and geometrically non-linear analysis which includes path-dependent or time dependent phenomena, the equilibrium relations in Eq. (2.3) need to be solved for the complete time range of interest. The effective computation of this response can be carried out by a step-by-step incremental analysis. The basic approach in an incremental step-by-step solution is to assume that the solution at time t is known and the solution at time $t + \Delta t$ is required where Δt is a suitably chosen time increment.

DESCRIPTION OF MOTION

To develop an appropriate formalism of the incremental approach, a proper description of the motion is necessary [Bonet & Wood, 2008]. Fig. (2.3) shows the general motion of a deforming body from its configuration at time $t = 0$ to time t . Generally the current positions of these particles at time t is denoted by the coordinates \boldsymbol{x} and their corresponding initial coordinates are represented by \boldsymbol{X} . Then, the motion can be mathematically described by a mapping between the initial and current particle positions as,

$$\boldsymbol{x} = \phi(\boldsymbol{X}, t) \tag{2.7}$$

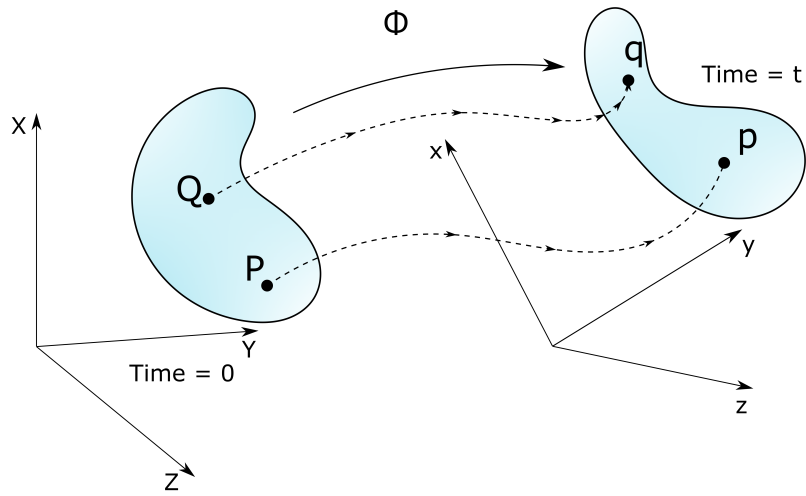


Figure 2.3: General motion of a deformable body [Bonet & Wood, 2008]

A relevant description of quantities associated with the material is possible based on where the body was before deformation and where it is on completion of the deformation. The former is called a *material (Lagrangian)* description and the latter is called a *spatial (Eulerian)* description. Often it is necessary to transform between the material and spatial description for relevant quantities. For example for a given quantity such as density, a spatial description can be easily obtained from a material description by using Eq. (2.7) as,

$$\rho(\boldsymbol{x}, t) = \rho(\phi(\boldsymbol{X}, t), t) \quad (2.8)$$

DEFORMATION GRADIENT AND STRAIN MEASURES

One of the key quantities involved in describing the motion of a body between different configurations is the deformation gradient \mathbf{F} which relates quantities before deformation to corresponding quantities after (or during) deformation. Confining attention to the elemental

vectors $d\mathbf{x}$ and $d\mathbf{X}$ in the deformed and initial configurations respectively, the deformation gradient tensor can be conveniently written as,

$$d\mathbf{x} = \frac{\partial \mathbf{x}}{\partial \mathbf{X}} d\mathbf{X} = \mathbf{F} d\mathbf{X} \quad (2.9)$$

or, more clearly as,

$$\mathbf{F} = \frac{\partial \mathbf{x}}{\partial \mathbf{X}} = \nabla_0 \mathbf{x} \quad \text{and} \quad \mathbf{F}^{-1} = \frac{\partial \mathbf{X}}{\partial \mathbf{x}} = \nabla \mathbf{X} \quad (2.10)$$

The deformation gradient tensor \mathbf{F} can be considered as the *push forward* operator and \mathbf{F}^{-1} can be considered as the *pull back* operator for different quantities in the material and spatial configuration.

The description of motion is incomplete without a measure of the deformation of the deforming body. If we consider an elemental vector $d\mathbf{X}$ which transforms to $d\mathbf{x}$ in the deformed configuration, using Eq. (2.9) the scalar product of the deformed elemental vector can be written as,

$$d\mathbf{x} \cdot d\mathbf{x} = d\mathbf{X} \cdot \mathbf{F}^T \mathbf{F} d\mathbf{X} = d\mathbf{X} \cdot \mathbf{C} d\mathbf{X} \quad (2.11)$$

where \mathbf{C} is the *right Cauchy-Green deformation tensor* and is given in terms of the deformation gradient as,

$$\mathbf{C} = \mathbf{F}^T \mathbf{F} \quad (2.12)$$

Alternatively, the scalar product of the undeformed elemental vector can be given as,

$$d\mathbf{X} \cdot d\mathbf{X} = d\mathbf{x} \cdot \mathbf{F}^{-T} \mathbf{F}^{-1} d\mathbf{x} = d\mathbf{x} \cdot \mathbf{B}^{-1} d\mathbf{x} \quad (2.13)$$

where \mathbf{B} is the *left Cauchy-Green deformation tensor* and is given in terms of the deforma-

tion gradient as:

$$\mathbf{B} = \mathbf{F}\mathbf{F}^T \quad (2.14)$$

A measure of strain in the body can then be found from the change in the scalar product as,

$$\frac{1}{2}(d\mathbf{x} \cdot d\mathbf{x} - d\mathbf{X} \cdot d\mathbf{X}) = d\mathbf{X} \cdot \mathbf{E} d\mathbf{X} = d\mathbf{x} \cdot \mathbf{e} d\mathbf{x} \quad (2.15)$$

where \mathbf{E} is the *Lagrangian* or *Green strain tensor* defined as,

$$\mathbf{E} = \frac{1}{2}(\mathbf{C} - \mathbf{I}) = \frac{1}{2}(\mathbf{F}^T\mathbf{F} - \mathbf{I}) \quad (2.16)$$

and \mathbf{e} is the *Eulerian* or *Almansi strain tensor* defined as,

$$\mathbf{e} = \frac{1}{2}(\mathbf{I} - \mathbf{B}^{-1}) = \frac{1}{2}(\mathbf{I} - \mathbf{F}^{-T}\mathbf{F}^{-1}) \quad (2.17)$$

where \mathbf{I} is the identity matrix.

The deformation gradient \mathbf{F} defined in Eq. (2.10) can also be expressed as a product of an orthogonal *rotation tensor* \mathbf{R} such that $\mathbf{R}^T\mathbf{R} = \mathbf{I}$ and *stretch tensors* \mathbf{U} or \mathbf{V} to define the polar decomposition of \mathbf{F} as,

$$\mathbf{F} = \mathbf{R}\mathbf{U} = \mathbf{V}\mathbf{R} \quad (2.18)$$

Recalling the definition of the *right* and *left Cauchy-Green deformation tensors* in Eqs. (2.12,2.14),

$$\mathbf{C} = \mathbf{F}^T \mathbf{F} = \mathbf{U}^T \mathbf{R}^T \mathbf{R} \mathbf{U} = \mathbf{U}^T \mathbf{U} = \mathbf{U}^2 \quad (2.19)$$

$$\mathbf{B} = \mathbf{F} \mathbf{F}^T = \mathbf{V} \mathbf{R} \mathbf{R}^T \mathbf{V}^T = \mathbf{V} \mathbf{V}^T = \mathbf{V}^2 \quad (2.20)$$

By performing an eigen value decomposition, the two deformation tensors can be resolved into their corresponding eigen vector triads and eigen values as,

$$\mathbf{C} = \sum_{\alpha=1}^3 \lambda_{\alpha}^2 \mathbf{N}_{\alpha} \otimes \mathbf{N}_{\alpha} \quad (2.21)$$

$$\mathbf{B} = \sum_{\alpha=1}^3 \bar{\lambda}_{\alpha}^2 \mathbf{n}_{\alpha} \otimes \mathbf{n}_{\alpha} \quad (2.22)$$

Because of the symmetry of \mathbf{C} and \mathbf{B} , the eigen vector triads are orthogonal unit vectors and hence the *material* and *spatial stretch tensors* \mathbf{U} and \mathbf{V} can be easily obtained as,

$$\mathbf{U} = \sum_{\alpha=1}^3 \lambda_{\alpha} \mathbf{N}_{\alpha} \otimes \mathbf{N}_{\alpha} \quad (2.23)$$

$$\mathbf{V} = \sum_{\alpha=1}^3 \bar{\lambda}_{\alpha} \mathbf{n}_{\alpha} \otimes \mathbf{n}_{\alpha} \quad (2.24)$$

But, from Eq. (2.18) we can deduce that,

$$\mathbf{V} = \mathbf{R} \mathbf{U} \mathbf{R}^T \quad (2.25)$$

Using Eq. (2.23) and Eq. (2.25), we can infer that,

$$\mathbf{V} = \sum_{\alpha=1}^3 \lambda_{\alpha} (\mathbf{R} \mathbf{N}_{\alpha}) \otimes (\mathbf{R} \mathbf{N}_{\alpha}) \quad (2.26)$$

Hence by comparison of Eq. (2.24) and Eq. (2.26), and noting that $(\mathbf{R}\mathbf{N}_\alpha)$ remains unit vectors, we conclude that,

$$\lambda_\alpha = \bar{\lambda}_\alpha; \quad \mathbf{n}_\alpha = \mathbf{R}\mathbf{N}_\alpha; \quad \alpha = 1 : 3 \quad (2.27)$$

implying that the *rotation tensor* \mathbf{R} rotates the principal directions in the initial configuration (\mathbf{N}_α) to the corresponding principal directions in the spatial configuration (\mathbf{n}_α) , while the unique eigen values λ_α^2 are the squares of the stretches in the principal directions. Thus the stretch tensors \mathbf{U} and \mathbf{V} in the principal directions can be easily evaluated from the eigen values of the *right* and *left Cauchy-Green deformation tensors*. The principal values of the stretch tensors in the principal directions are equal to the material stretch λ_α in the principal directions. The Lagrangian and Eulerian strain tensors defined in Eq. (2.16) and Eq. (2.17) can now be expressed in terms of \mathbf{U} and \mathbf{V} as,

$$\begin{aligned} \mathbf{E} &= \frac{1}{2} (\mathbf{U}^2 - \mathbf{I}) \\ \mathbf{e} &= \frac{1}{2} (\mathbf{I} - \mathbf{V}^{-2}) \end{aligned}$$

This leads to the definition of the Seth-Hill [Hill, 1968] family of generalized strains defined as,

$$\mathbf{E}^{(m)} = \begin{cases} \frac{1}{2m} (\mathbf{U}^{2m} - \mathbf{I}) & m \neq 0 \\ \ln (\mathbf{U}) & m = 0 \end{cases} \quad (2.28)$$

The Seth-Hill family of generalized strains are dependent only on the stretch tensor and hence are objective strain tensors that do not depend on rigid body motions.

2.1.3 INCREMENTAL DEFORMATION PROBLEM

Consider the motion of a general body in a stationary Cartesian coordinate system that can undergo finite displacements, strains and a non-linear constitutive response as shown in Fig (2.4).

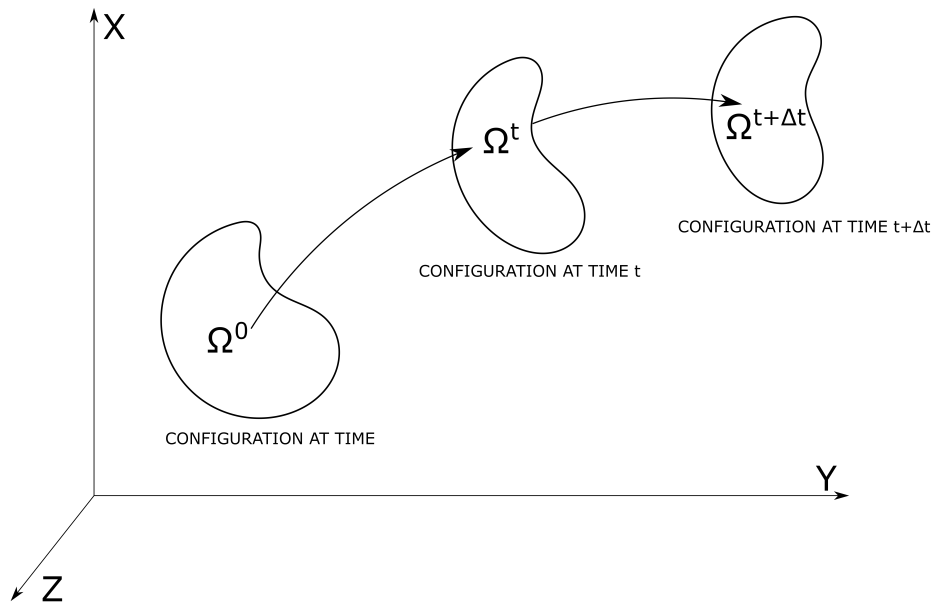


Figure 2.4: Motion of a body[Bathe et al., 1975]

The solution of the incremental deformation problem necessitates that the equilibrium position of the body at discrete time points $0, \Delta t, 2\Delta t, 3\Delta t, \dots$, is known, where Δt is an increment in time. The incremental solution strategy assumes that the static and kinematic variables for all time steps from time 0 to time t is known. This information is then used to evaluate the equilibrium position and the corresponding static and kinematic variable at time $t + \Delta t$ and is applied repetitively till the complete solution path has been solved for. Using Eq. (2.6) the equilibrium state of the body at time $t + \Delta t$ can be expressed as,

$$\int_{\Omega^{t+\Delta t}} \boldsymbol{\sigma}^{t+\Delta t} : \boldsymbol{\varepsilon}^* d\Omega + \int_{\Omega^{t+\Delta t}} K (\varepsilon_v^{t+\Delta t}) \varepsilon_v^* d\Omega - \int_{\Omega^{t+\Delta t}} \rho^{t+\Delta t} \mathbf{b}^{t+\Delta t} \cdot \mathbf{u}^* d\Omega = 0 \quad (2.29)$$

$$\int_{\Omega^{t+\Delta t}} \boldsymbol{\sigma}^{t+\Delta t} : \boldsymbol{\varepsilon}^* d\Omega = \mathfrak{R}^{t+\Delta t} \quad (2.30)$$

where, $\mathfrak{R}^{t+\Delta t} = \int_{\Omega^{t+\Delta t}} \rho^{t+\Delta t} \mathbf{b}^{t+\Delta t} \cdot \mathbf{u}^* d\Omega - \int_{\Omega^{t+\Delta t}} K (\varepsilon_v^{t+\Delta t}) \varepsilon_v^* d\Omega$.

2.1.4 THERMODYNAMICS

The work-ability of the workpiece during a metal forming process is highly dependent on the flow-stress of the material used. This flow-stress is dependent on the temperature of the work-piece and in hot and warm-forming simulations it is imperative to consider the thermal state of the workpiece both at the beginning and also during the transformation. The principal modes of heat transfer in a metal forming process are:

- Heat conduction / diffusion within the workpiece
- Conductive heat flux between the work-piece and the tools from the part of the boundary in contact
- Convective heat flux between the free surface boundary of the work-piece and the ambient atmosphere
- Radiative heat transfer from the work-piece to the surroundings from the free surface boundary
- Mechanical dissipation converted to heat within the work-piece

The unsteady heat transfer problem associated with the metal forming process can thus be expressed mathematically as,

$$\begin{aligned}
\rho c \dot{T} - \operatorname{div}(k \nabla T) &= r \quad \text{in } \Omega \\
-k \nabla T &= h_{wd} (T - T_d) \quad \text{on } \partial_d \Omega \\
-k \nabla T &= h_{wa} (T - T_a) + \epsilon \sigma (T^4 - T_a^4) \quad \text{on } \partial_f \Omega
\end{aligned} \tag{2.31}$$

where ρ is the density, c is the specific heat capacity, k is the thermal conductivity, r is the volumetric heat source, T is the unknown temperature field, h_{wd} is the heat transfer coefficient at the interface between the work-piece and the die, T_d is the temperature of the die, h_{wa} is the heat transfer coefficient at the interface between the work-piece and the ambient environment, T_a is the temperature of the ambient environment, ϵ is the emissivity, σ is the Stefan-Boltzmann constant and \mathbf{n} is an outward unit normal to the surface.

By using the principle of virtual work and Green's divergence theorem, the weak form of Eq. (2.31) for isotropic materials can be written as:

$$\int_{\Omega} k \nabla T \nabla T^* d\Omega + \int_{\Omega} \rho c \dot{T} T^* d\Omega - \int_{\Omega} r T^* d\Omega - \int_{\partial \Omega} k \nabla T T^* d\Gamma = 0 \tag{2.32}$$

where,

$$\begin{aligned}
- \int_{\partial \Omega} k \nabla T T^* d\Gamma &= \int_{\partial_d \Omega} h_{wd} (T - T_d) T^* d\Gamma + \int_{\partial_f \Omega} h_{wa} (T - T_a) T^* d\Gamma \\
&\quad + \int_{\partial_f \Omega} \epsilon \sigma (T^4 - T_a^4) T^* d\Gamma
\end{aligned}$$

Considering that there are no other volumetric heat source terms other than the mechanical dissipation and that the mechanical dissipation is equivalent to the heat released due to

the plastic work, Eq. (2.32) can be expressed as,

$$\int_{\Omega} k \nabla T \nabla T^* d\Omega + \int_{\Omega} \rho c \dot{T} T^* d\Omega - \int_{\Omega} \kappa \boldsymbol{\sigma} : \dot{\boldsymbol{\epsilon}} T^* d\Omega - \int_{\partial\Omega} k \nabla T T^* d\Gamma = 0 \quad (2.33)$$

where κ represents the fraction of the mechanical dissipation converted to heat (Taylor-Quinney coefficient [Taylor & Quinney, 1934, Rittel et al., 2017]), $\boldsymbol{\sigma}$ is the Cauchy stress tensor and $\dot{\boldsymbol{\epsilon}}$ is the strain rate.

2.1.5 FINITE ELEMENT METHOD

In the continuum approach, the body under consideration is considered as an infinite media. Since the partial differential equations generated by the complex interactions do not have an easy closed form analytical solution, one needs to resort to approximate numerical methods which can solve the numerical problem with ease and necessary accuracy. A particular property of a continuum body is that even if the body is broken into different pieces, the body tends to retain the characteristics of the material with each part. For example, a steel rod can be broken into many pieces but each broken piece will still remain to be a steel part.

Supposing that the problem to be solved is defined in the geometric domain Ω , it can be discretized by cutting it into a number of non-overlapping subdomains. These are called element domains or simply elements and behave in a similar manner to the real material and are assumed to be interconnected to each other at a discrete number of nodal points on their boundaries. The displacements (or any other field variable like temperature) of these nodal points will be the basic unknowns of the problem. A suitable basis function (shape functions) is chosen to define uniquely the state of displacement (or other field variables like velocity, temperature etc) within each element and on its boundaries in terms of the nodal values. These shape functions relate nodal values to the function values (which approximate the exact solution) inside an element. This helps in expressing the partial differential equa-

tions in the form of a sum over all the elements and therefore an integral solution. Thus, the finite element model has two essential characteristics: It fills space corresponding to a physical part of the body being modeled and it has an associated integral form in its interior that approximates the variation of a quantity sought in the solution [Wagoner & Chenot, 2005]. A detailed description of the Finite Element method maybe found in [Zienkiewicz & Taylor, 2000a,b] and their implementation in a computer program maybe found in [Smith et al., 2013].

2.2 METAL FORMING ANALYSIS BY THE FINITE ELEMENT METHOD

2.2.1 TOTAL LAGRANGIAN AND UPDATED LAGRANGIAN FORMULATIONS

A fundamental difficulty in the general direct application of Eq. (2.29) is that the deformed configuration of the body is an unknown that needs to be evaluated and is not known *a priori*. Also, care should be taken to use appropriate objective strain and stress measures for the evaluation of the deformed configuration of the body due to the significant changes in the configuration of the body.

For greater clarity in the mathematical expressions, the following notation convention is used. A right superscript indicates the time at which the quantity occurs/is measured and a right subscript indicates the configuration with respect to which the quantity is measured. For example the body force component at time $t + \Delta t$ measured at configuration time $t = 0$ will be represented as $\mathbf{b}_0^{t+\Delta t}$. If the quantity under consideration occurs in the same configuration in which it is also measured, the right subscript may not be used. For example the Cauchy stress measured in configuration $t + \Delta t$ will be represented as $\boldsymbol{\sigma}^{t+\Delta t}$.

Since the configuration at time $t + \Delta t$ is not known, all forces, stresses and strains will be referred to a known configuration. This change in configuration can be dealt with in an elegant manner using the deformation gradient tensor and the strain measures defined previously. The objective of their definition is to express the virtual work equation expressed in Eq. (2.29) in terms of an integral over a volume that is known, and to incrementally de-

compose the stresses and strains. A stress measure that aids in the proper description of this transformation is the symmetric *Second Piola-Kirchhoff stress tensor*. At time t , the second Piola-Kirchhoff stress referred to the configuration at time 0 is defined as,

$$\mathbf{S}_0^t = J (\mathbf{F}_0^t)^{-1} \boldsymbol{\sigma}^t (\mathbf{F}_0^t)^{-T} \quad (2.34)$$

where $J = \det(\mathbf{F})$. However it should be noted that even though it is possible to relate the Cauchy stress tensor to the second Piola-Kirchhoff stress tensor by the above transformation, it holds little physical meaning and in practice, Cauchy stresses must be calculated. The objective Green-Lagrange strain tensor defined in Eq. (2.16) is work-conjugate to the second Piola-Kirchhoff stress tensor and hence the equilibrium configuration defined by Eq. (2.29) can be expressed in terms of the configuration at time 0 as,

$$\int_{\Omega^0} \mathbf{S}_0^{t+\Delta t} : (\mathbf{E}^*)_0^{t+\Delta t} d\Omega = \mathfrak{R}_0^{t+\Delta t} \quad (2.35)$$

where $\mathfrak{R}_0^{t+\Delta t}$ is the external work at time $t + \Delta t$ referred to the undeformed configuration.

Using the incremental additive decomposition of the second Piola-Kirchhoff stress tensor as $\mathbf{S}_0^{t+\Delta t} = \mathbf{S}_0^t + \Delta \mathbf{S}_0$ and appropriate linearizations, an approximate equation of motion can be written in terms of the initial configuration at time $t = 0$. This is generally referred to as the *Total Lagrangian (TL)* formulation. If instead of referring to the configuration at time $t = 0$, the quantities are referred to the previous known configuration at time t , then we can obtain the *Updated Lagrangian (UL)* formulation which can be expressed as,

$$\int_{\Omega^t} \mathbf{S}_t^{t+\Delta t} : (\mathbf{E}^*)_t^{t+\Delta t} d\Omega = \mathfrak{R}_t^{t+\Delta t} \quad (2.36)$$

where $\mathbf{S}_t^{t+\Delta t} = \mathbf{S}_t^t + \Delta \mathbf{S}_t = \boldsymbol{\sigma}^t + \Delta \mathbf{S}_t$.

Both the formulations include all kinematic nonlinear effects attributed to large displacements, rotations and strains if appropriate constitutive relations are used since the only theoretical difference between the two formulations lies in the choice of the reference configura-

tions for the kinematic and static variables. The choice of using the TL or UL formulation in a finite element solution depends on their relative numerical efficiency. The incremental strains in the TL formulation contains an initial displacement term that leads to a more complex strain-displacement matrix than the UL formulation. It should also be noted that the incremental decomposition of the stresses as shown above is only possible because they are all referred to the same configuration. A detailed description of the various formulations may be found in any standard textbook on non-linear analysis using Finite Element Methods [Bathe et al., 1975, Bathe, 1996, Bonet & Wood, 2008].

2.2.2 DRAWBACKS OF THE LAGRANGIAN FORMULATIONS

Although an appropriate mathematical description of the metal-forming process can be given by a Total Lagrangian formulation or Updated Lagrangian formulation based on the incremental deformation approach, the numerical analysis based upon these formulations are time-consuming. Even though no assumptions regarding deformation is made in the formulation, due to the assumptions used in the linearization of different variables, the step-sizes used in an incremental approach remain relatively small. Moreover, to account for the evolution of the contact interface and the associated non-linear effect and change in boundary conditions, suitable step-sizes have to be taken. Another major limitation comes into account from the choice of the second Piola-Kirchhoff stress tensor for the transformations. The objective strain measure that is work conjugate to the second Piola-Kirchhoff stress tensor is the Green-Lagrange strain tensor. Even though the Green-Lagrange strain tensor is an objective strain tensor it is not easy to decompose it in an additive or multiplicative manner unless suitable assumptions are made. This also imposes a limitation in terms of the step-size that can be considered without deteriorating the accuracy of the results. This makes the incremental deformation analysis a computationally costly affair that requires small steps.

A major objective in metal-forming processing is the optimum selection of process conditions in the design stage of processes, given the material state and the geometry of the final

product, conditions on the initial work-piece and possibly some restrictions on the processes. Since the required process conditions are required inputs for the direct analysis, the design of forming processes usually consists of the repeated trial and error use of direct modeling techniques where the initial shape forms are defined by qualitative guidelines which have been derived mainly from experience or experimental studies. The preform design and the die design problems can be formulated under a rigorous mathematical basis by posing them as optimization problems and can be solved with forward analysis methods to find optimal solutions. Approaches based on sensitivity analysis [Badrinarayanan & Zabararas, 1996], parameter-based B-spline optimization [Fourment & Chenot, 1996, Fourment et al., 1996] and parameter free shape optimization [Steinmann & Landkammer, 2014] among others have been employed in this regard. More recently meta-model assisted methods [Ejday & Fourment, 2010] and approaches based on neural networks [Ciancio et al., 2015, D'Addona & Antonelli, 2018] have also been proposed. Although simplistic in nature, the widespread use of such optimization techniques has been limited due to the computational expenses of the forward analysis for each design iteration.

2.2.3 INVERSE FORMULATIONS

Process design in forging is concerned with finding the optimal reference geometry. This, in essence, is an inverse shape finding problem. The inverse form finding problem can be stated as: for a given deformed shape parameterized by the spatial coordinates \boldsymbol{x} , and associated boundary data, find the material configuration, i.e. the undeformed shape \boldsymbol{X} such that $\boldsymbol{X} = \Phi(\boldsymbol{x})$, where $\Phi = \phi^{-1}$ (From Eq. (2.7)), satisfies the equilibrium requirement for the spatial configuration [Germain et al., 2010]. This type of inverse problems have been extensively studied starting from the works of [Yamada, 1995, Govindjee & Mihalic, 1996, 1998] who applied it to problems in hyperelasticity.

The Backward tracing method can thus be described as follows. Consider that at time $t = t$, the geometrical configuration \boldsymbol{x}_t of a deforming body is represented by a point Q .

The point Q is arrived at from the point P whose configuration at time $t = t - \Delta t$ is given by $\mathbf{x}_{t-\Delta t}$ through the displacement \mathbf{u} during a time step Δt such that $\mathbf{x}_t = \mathbf{x}_{t-\Delta t} + \mathbf{u}$. The solution consists of finding the displacement \mathbf{u} which satisfies the equilibrium configuration. The solution scheme consists of taking an initial guess of \mathbf{u}^0 to get an initial estimate P^1 such that $P^1 = \mathbf{x}_t - \mathbf{u}^0$. Then the loading solution \mathbf{u}^1 is computed using P^1 as the reference. Q^1 can now be computed as $Q^1 = P^1 + \mathbf{u}^1$ and compared with Q . If Q and Q^1 are not sufficiently close to each other, a new estimate of P is made as $P^2 = \mathbf{x}_t - \mathbf{u}^1$ to obtain a new estimate Q^2 and the process is continued iteratively till $Q^n = P^n + \mathbf{u}^n$ is sufficiently close to Q [Park et al., 1983].

In the case of bodies undergoing plastic deformation, the problem is ill-posed and the inverse solution is not unique unless the loading history or the plastic strain in the deformed state is known. Solving the elasto-plastic inverse shape-finding problem was demonstrated in [Germain et al., 2014, Landkammer et al., 2014, Steinmann & Landkammer, 2014] using a recursive method consisting of iterative loops of inverse and forward analyses to find the plastic variables. In each loop, an inverse step is carried out first, with plastic variables fixed at their current value. This is followed by a forward step applied on the predicted reference geometry to generate the plastic variables. In essence, this is an operator-splitting scheme which splits the inverse problem into two sub-problems: determining the reference geometry and determining the plastic variables. The plastic flow is introduced in the forward step to recover the loading path. A direct method limited to monotonic loading and moderately large deformations was proposed in [Lu & Li, 2017].

2.2.4 DRAWBACKS OF THE BACKWARD TRACING METHODS

Ignoring the non-physical nature of the inverse loading path, the principal drawback of the backward tracing method in metal forming analysis stems from the ill-posedness of the problem and the recursive formulation needed for the prediction of the plastic variables. Since the forward step relies on the classical incremental deformation formulation, the backward

tracing method ends up being an extremely time consuming method for predicting the initial shape for the desired deformed shape. Another more important drawback of the backward tracing method is its unsuitability for being used in hot-forging simulations since the thermal field at the end of the deformation process in the final forged is completely unknown.

One cannot escape the feeling that these mathematical formulae have an independent existence and an intelligence of their own, that they are wiser than we are, wiser even than their discoverers

Heinrich Hertz

3

Pseudo Inverse Approach for Metal Forming Analysis

THE fundamental problem that needs to be analyzed for a proper metal forming analysis has been discussed in the previous chapter. Even though the backward tracing schemes show promise at finding an optimal initial shape, it is bogged down by the extensive computational requirements of the forward steps in the recursive formulation needed for a plastic deformation analysis. Thus, the inverse methods can only become of practical use if a scheme is devised to compute the forward deformation robustly and with enough accuracy at reduced computational costs.

3.1 PSEUDO INVERSE APPROACH

At its most basic, the Pseudo Inverse Approach is an extension of the single-step Inverse Approach first applied in sheet metal forming [Guo et al., 1990, 2004]. This single step method was extended to bulk metal forging in [Halouani et al., 2010], but multiple analysis indicated that the stresses predicted by the single step method was poor since the deformation paths and the accumulated plastic strains were not being taken into account. A way to improve the results is to do a multi-step inverse simulation with intermediate shapes predicted from the knowledge of the final shape and the initial shape. This was attempted in [Halouani et al., 2012b] in the case of cold forging and was found to provide accurate enough predictions of the stresses where geometrically predicted intermediate shapes were used to speed up the multi-step computation. This works in a similar way to the Backward Tracing Method using a recursive analysis, but is faster due to the use of the geometrically predicted intermediate shapes resulting in large time steps and consequently fewer steps needed for the computation of the entire process. Since these inverse methods are incapable of incorporating the effects of the accumulated plastic work *a priori* at each step, a forward analysis method which effectively takes into account the accumulated plastic work, while being much faster than the incremental deformation approach, is required. This is where the PIA proves itself useful and it is based on three main postulates

1. The governing equations of the metal forming simulation are inherently non-linear and solving these non-linear equations can be effectively done using a Newton-Raphson method. The convergence to a solution through the Newton-Raphson method is highly influenced by the initial solution that is provided and if an initial guess that is close to the final solution can be provided, then convergence to a solution is possible for even very large steps.
2. As the metal-forming processes are relatively quick, the loss of heat to the environment through convection or radiation and to the tools through conduction can be approximated reasonably well even with very large time steps.

3. Monotonic loading. In such a case there is no reverse plastic loading and though the requirement might seem stringent, most bulk forming operations fit into this category.

3.1.1 DESCRIPTION OF THE METHOD

In the previous chapter, we had discussed the reasons behind the low step sizes and the high computational requirements of the incremental deformation method. The inability to predict the deformed configuration at each time-step in an effective manner is the principal reason for the formulation in an incremental deformation formulation to be referred back to a previously known configuration and stress measures that have no direct physical meaning. The forming process is an interesting exception in this case, since, in the case of a forming operation, the final deformed shape (the target shape) is generally known. Thus, if the initial shape is also known (or if a quick approximation of the initial shape can be made) then it would be possible to predict the deformed shapes at the different time steps effectively using the geometric information from both the deformed and undeformed configuration while considering a monotonic loading path. If the deformed shape (or a close enough approximation) is known, then it would be possible to verify whether that configuration satisfies the equilibrium and contact conditions and consequently the field variables. This is the core concept that is utilized in PIA. The steps involved in the Pseudo Inverse Approach can be summarized as below:

1. A single-step Inverse Approach is used to generate or check the suitability of the assumed initial shape for the direct analysis and to transfer the mesh on the final part to the initial part
2. The entire deformation process is divided into multiple steps, based on how well the deformation path needs to be re-created and intermediate shapes are created through geometric interpolation.
3. These geometrically interpolated intermediate shapes are then corrected using a free surface method to obtain kinematically admissible intermediate shapes.

4. A finite-strain, finite-displacement forward thermo-mechanical analysis using the deformed configuration as the reference configuration is conducted at each step to check for the equilibrium. The actual deformed configuration and stresses are obtained using a Newton-Raphson algorithm and logarithmic strain increments.
5. The process is repeated till the entire range of deformation has been accounted for.

3.1.2 MATHEMATICAL FORMULATION & FINITE ELEMENT METHOD

Using the mathematical formulation of the forming process introduced in the previous chapter, the complete problem to be solved in a hot-forming analysis using Eqs. (2.1),(2.4) and (2.31) can be stated as:

For any body undergoing deformation as depicted in Fig. (2.2), find \mathbf{u} and T such that,

$$\begin{aligned}
\operatorname{div} \boldsymbol{\sigma} + \rho \mathbf{b} &= 0 \quad \text{in } \Omega \\
(\mathbf{u} - \mathbf{u}_g) \cdot \mathbf{n} &= 0 \quad \text{on } \partial_d \Omega \\
\boldsymbol{\sigma} \mathbf{n} &= \mathbf{t} = 0 \quad \text{on } \partial_f \Omega \\
\operatorname{div} \mathbf{u} &= 0 \\
\rho c \dot{T} - \operatorname{div}(k \nabla T) &= r \quad \text{in } \Omega \\
-k \nabla T &= h_{wd}(T - T_d) \quad \text{on } \partial_d \Omega \\
-k \nabla T &= h_{wa}(T - T_a) + \epsilon \sigma (T^4 - T_a^4) \quad \text{on } \partial_f \Omega
\end{aligned} \tag{3.1}$$

Using the developments detailed in the previous chapter, the weak form of Eq. (3.1) for a body in static equilibrium can be stated as,

$$\int_{\Omega} \boldsymbol{\sigma} : \boldsymbol{\varepsilon}^* d\Omega + \int_{\Omega} K \varepsilon_v \varepsilon_v^* d\Omega - \int_{\Omega} \rho \mathbf{b} \cdot \mathbf{u}^* d\Omega = 0$$

$$\int_{\Omega} k \nabla T \nabla T^* d\Omega + \int_{\Omega} \rho c \dot{T} T^* d\Omega - \int_{\Omega} r T^* d\Omega - \int_{\partial\Omega} k \nabla T T^* d\Gamma = 0 \quad (3.2)$$

Using a finite element discretization, the displacement field inside an element can be interpolated from the position of the element nodes as,

$$\mathbf{x} = \sum_{i=1}^n N_i \mathbf{x}_i \quad (3.3)$$

where \mathbf{x}_i are the position of the element nodes, N_i are the element shape functions and n is the number of nodes in the element.

Using a similar discretization, the displacement and temperature fields in an element can be interpolated as,

$$\mathbf{u} = \sum_{i=1}^n N_i \mathbf{u}_i; \quad T = \sum_{i=1}^n N_i T_i$$

Using this interpolation, Eq. (3.2) can be expressed in the assembled form as,

$$\sum_{e=1}^{nel} \mathbf{u}_i^* \cdot \left(\int_{\Omega^e} \mathbf{B}_m^T \boldsymbol{\sigma} d\Omega + \int_{\Omega^e} K \varepsilon_v \mathbf{B}_v d\Omega - \int_{\Omega^e} \rho N_i^T \mathbf{b} d\Omega \right) = 0$$

$$\sum_{e=1}^{nel} T_i^* \left(\int_{\Omega^e} k \mathbf{B}_t \mathbf{B}_t^T T_i d\Omega + \int_{\Omega^e} \rho c N_i N_i^T T_i d\Omega - \int_{\Omega^e} r N_i d\Omega + \int_{\partial\Omega^e} q_i N_i d\Gamma \right) = 0 \quad (3.4)$$

where $\boldsymbol{\varepsilon}^* = \mathbf{B}_m \mathbf{u}_i^*$, $\mathbf{B}_v = \mathbf{B}_m \mathbf{I}$, $\mathbf{B}_t = \nabla N_i$ and $q = -k \nabla T$. Eq. (3.4) can be alternatively expressed as,

$$\begin{aligned}
\sum_{e=1}^{nel} \mathbf{u}_i^* \cdot (\mathbf{F}_{int}^e - \mathbf{F}_{ext}^e) &= \sum_{e=1}^{nel} \mathbf{u}_i^* \cdot \mathbf{R}^e = 0 \\
\sum_{e=1}^{nel} T_i^* \left(\mathbf{C}^e \dot{\mathbf{T}} + \mathbf{K}_c^e \mathbf{T} - \mathbf{Q}^e \right) &= 0
\end{aligned} \tag{3.5}$$

where

$$\begin{aligned}
\mathbf{F}_{int}^e &= \int_{\Omega^e} \mathbf{B}_m^T \boldsymbol{\sigma} d\Omega; & \mathbf{F}_{ext}^e &= \int_{\Omega^e} \rho N_i^T \mathbf{b} d\Omega - \int_{\Omega^e} K \varepsilon_v \mathbf{B}_v d\Omega \\
\mathbf{C}^e &= \int_{\Omega^e} \rho c N_i N_i^T d\Omega; & \mathbf{K}_c^e &= \int_{\Omega^e} k \mathbf{B}_t \mathbf{B}_t^T d\Omega
\end{aligned}$$

$$\begin{aligned}
\mathbf{Q}^e &= \int_{\Omega^e} \kappa \boldsymbol{\sigma} : \dot{\boldsymbol{\varepsilon}} N_i d\Omega - \int_{\partial_f \Omega^e} \sigma \epsilon (T^4 - T_a^4) N_i d\Gamma - \int_{\partial_f \Omega^e} h_{wa} (T - T_a) N_i d\Gamma \\
&\quad - \int_{\partial_a \Omega^e} h_{wd} (T - T_d) N_i d\Gamma
\end{aligned}$$

Since Eq. (3.5) should be valid for all admissible \mathbf{u}^* and T^* , we have,

$$\mathbf{F}_{int} - \mathbf{F}_{ext} = \mathbf{R} = 0 \tag{3.6}$$

and

$$\mathbf{C} \dot{\mathbf{T}} + \mathbf{K}_c \mathbf{T} - \mathbf{Q} = 0 \tag{3.7}$$

where \mathbf{F}_{int} and \mathbf{F}_{ext} represents the global internal and external forces, \mathbf{R} is the global residual force vector, \mathbf{C} is the heat capacity matrix, \mathbf{K}_c is the heat conduction matrix, \mathbf{Q} is the heat flux vector and \mathbf{T} and $\dot{\mathbf{T}}$ are the vectors of nodal temperatures and nodal temperature rates respectively.

3.1.3 FEM SOLUTION OF THE COUPLED PROBLEM

If in case, the configuration is not in static equilibrium, then Eq. (3.6) becomes,

$$\mathbf{F}_{int} - \mathbf{F}_{ext} = \mathbf{R} \neq 0 \quad (3.8)$$

In such a scenario, the equilibrium configuration and the solution of the problem involves finding a displacement \mathbf{u} such that $\mathbf{R} \rightarrow 0$. This can be solved very efficiently using a Newton-Raphson algorithm. The Newton-Raphson procedure in this context can be summarized by the following algorithm.

Algorithm 1 Newton-Raphson Algorithm - Mechanical sub-problem

- For a given \mathbf{u} , find $\mathbf{R} = \mathbf{F}_{int}(\mathbf{u}) - \mathbf{F}_{ext}(\mathbf{u})$
 - While ($\|\mathbf{R}\| > \text{tolerance}$)
 - Find tangent stiffness matrix $\mathbf{K} = \frac{\partial \mathbf{R}}{\partial \mathbf{u}}$
 - Solve $\mathbf{K} \delta \mathbf{u} = -\mathbf{R}$
 - Update \mathbf{x} and \mathbf{u} such that: $\mathbf{x} = \mathbf{x} + \delta \mathbf{u}$; $\mathbf{u} = \mathbf{u} + \delta \mathbf{u}$
 - For the updated displacement \mathbf{u} , find $\mathbf{R} = \mathbf{F}_{int}(\mathbf{u}) - \mathbf{F}_{ext}(\mathbf{u})$
-

The thermal equation given in Eq. (3.7) is a transient equation and has to be integrated over time using a one-step method like the generalized trapezoidal method [Hughes, 2000] given by,

$$T_{t+\Delta t} = T_t + \left[\beta \dot{T}_{t+\Delta t} + (1 - \beta) \dot{T}_t \right] \Delta t \quad (3.9)$$

or,

$$\dot{T}_{t+\Delta t} = \frac{(T_{t+\Delta t} - T_t)}{\beta \Delta t} - \frac{(1 - \beta)}{\beta} \dot{T}_t \quad (3.10)$$

Using Eq. (3.10), Eq. (3.7) can be written as,

$$\mathbf{C} \left(\frac{(T_{t+\Delta t} - T_t)}{\beta \Delta t} - \frac{(1 - \beta)}{\beta} \dot{T}_t \right) + \mathbf{K}_c T_{t+\Delta t} - \mathbf{Q} = 0 \quad (3.11)$$

or more concisely,

$$\left(\mathbf{K}_c + \frac{1}{\beta \Delta t} \mathbf{C} \right) T_{t+\Delta t} = \mathbf{Q} + \frac{1}{\beta \Delta t} \mathbf{C} T_t + \frac{(1 - \beta)}{\beta} \mathbf{C} \dot{T}_t \quad (3.12)$$

The parameter β can vary from 0 to 1. Unconditional stability is obtained if $\beta \geq 0.5$ and is important in our case due to the large deformations being considered. An algorithm for the solution of the transient thermal problem can be given as,

Algorithm 2 Thermal transient solution

- From the known temperature field T at time t , compute initial temperature rate \dot{T}_t using Eq. (3.7).
 - Using an initial assumption for $\dot{T}_{t+\Delta t}$, compute $T_{t+\Delta t}^{trial}$
 - Using $T_{t+\Delta t}^{trial}$, compute \mathbf{Q}
 - Solve for $T_{t+\Delta t}$ using Eq. (3.12)
 - While ($(T_{t+\Delta t}^{trial} - T_{t+\Delta t}) > \text{tolerance}$)
 - $T_{t+\Delta t}^{trial} = T_{t+\Delta t}$
 - recompute \mathbf{Q}
 - Solve for $T_{t+\Delta t}$ using Eq. (3.12)
-

Eqs. (3.6) and (3.7) are coupled and thus a complete simulation requires the simultaneous solution of both. Different coupling strategies have been explored for the solution of the thermo-mechanically coupled problem including the monolithic schemes as well as operator-

splitting schemes (staggered schemes) like iso-thermal split and adiabatic split [Armero & Simo, 1993]. The monolithic scheme is computationally more expensive and for a forming process simulation it has been found that an iterative staggered scheme is both computationally efficient while being accurate enough [Vaz & Lange, 2016] and offering unconditional stability. The iterative scheme solves iteratively the individual mechanical and thermal problems at each time step (or selected solution intervals) so that fully converged, cross-dependent temperature and displacement solutions are obtained at the end of each solution increment (or selected solution intervals).

3.1.4 FINITE DEFORMATION STRESS UPDATES

In the case of finite deformation problems it is important to have a consistent scheme for the updation of stresses that respects the restrictions on the configurations in which the different stress and strain measures are defined. In our case, the mathematical equations are completely defined on the deformed configuration and hence we need to compute the Cauchy stresses ($\boldsymbol{\sigma}$) in the deformed configuration. The Cauchy stresses are work-conjugate to the logarithmic strain measure [Xiao et al., 1997] given by the family of Seth-Hill strains defined in Eq. (2.28) with $m = 0$. Thus the consistent Eulerian strain tensor in the deformed configuration can be given as,

$$\boldsymbol{\varepsilon} = \ln(\mathbf{V}) \quad (3.13)$$

From the discussions in Sec. (2.1.2) we know that the principal values of the stretch tensor \mathbf{V} is given by the principal stretches. The logarithmic strains have the property that the strain at an unknown configuration can be easily given from the expression,

$$\boldsymbol{\varepsilon}_{t+\Delta t} = \boldsymbol{\varepsilon}_t + \Delta\boldsymbol{\varepsilon} \quad (3.14)$$

where $\Delta\boldsymbol{\varepsilon}$ corresponds to the logarithmic strain increase in that time step.

The movement of a material point between two successive configurations Ω^t and $\Omega^{t+\Delta t}$ can be expressed as $\mathbf{x}^{t+\Delta t} = \mathbf{x}^t + \mathbf{u}$ where \mathbf{x}^t and $\mathbf{x}^{t+\Delta t}$ are the position vectors in Ω^t and $\Omega^{t+\Delta t}$ and \mathbf{u} is the displacement increment vector expressed in the local reference coordinates corresponding to the configuration $\Omega^{t+\Delta t}$. Using Eq. (2.10) the local inverse deformation gradient tensor \mathbf{F}^{-1} can be defined as,

$$\mathbf{F}^{-1} = \frac{\partial \mathbf{x}^t}{\partial \mathbf{x}^{t+\Delta t}} = \left[\mathbf{I} - \frac{\partial \mathbf{u}}{\partial \mathbf{x}^{t+\Delta t}} \right] \quad (3.15)$$

and the deformation gradient tensor \mathbf{F} as,

$$\mathbf{F} = \frac{\partial \mathbf{x}^{t+\Delta t}}{\partial \mathbf{x}^t} = \left[\mathbf{I} + \frac{\partial \mathbf{u}}{\partial \mathbf{x}^t} \right] \quad (3.16)$$

Using Eq. (2.14) inverse of the left Cauchy-Green tensor can then be expressed as,

$$\mathbf{B}^{-1} = \mathbf{F}^{-T} \mathbf{F}^{-1} \quad (3.17)$$

By doing a spectral decomposition the the left Cauchy-Green tensor the eigenvalues ($\lambda_1^{-2}, \lambda_2^{-2}, \lambda_3^{-2}$) of the tensor \mathbf{B}^{-1} can be found out. These can be found to be of the form,

$$\mathbf{B}^{-1} = \mathbf{M} \begin{bmatrix} \lambda_1^{-2} & 0 & 0 \\ 0 & \lambda_2^{-2} & 0 \\ 0 & 0 & \lambda_3^{-2} \end{bmatrix} \mathbf{M}^T \quad (3.18)$$

where \mathbf{M} is an appropriate orthogonal matrix. From these principal eigen values, the principal logarithmic strain increment can be given by,

$$\Delta \boldsymbol{\varepsilon}_{princ} = \begin{Bmatrix} \Delta \boldsymbol{\varepsilon}_1 \\ \Delta \boldsymbol{\varepsilon}_2 \\ \Delta \boldsymbol{\varepsilon}_3 \end{Bmatrix} = \begin{Bmatrix} \ln(\lambda_1) \\ \ln(\lambda_2) \\ \ln(\lambda_3) \end{Bmatrix} \quad (3.19)$$

The logarithmic strains in the global reference can then be obtained by the transformation,

$$\Delta \boldsymbol{\varepsilon} = \mathbf{M} \Delta \boldsymbol{\varepsilon}_{princ} \mathbf{M}^T \quad (3.20)$$

The stress at the current configuration $\Omega^{t+\Delta t}$ can be found out from the stress at the previous configuration Ω^t using an incremental approach as,

$$\boldsymbol{\sigma}^{t+\Delta t} = \boldsymbol{\sigma}_{t+\Delta t}^t + \Delta \boldsymbol{\sigma} \quad (3.21)$$

where $\boldsymbol{\sigma}_{t+\Delta t}^t$ is the Cauchy stress at time t represented in the current configuration $\Omega^{t+\Delta t}$.

From the definition of the Second Piola-Kirchhoff stress tensor \mathbf{S} , we know that

$$\mathbf{S}_t^{t+\Delta t} = J \mathbf{F}^{-1} \boldsymbol{\sigma}^{t+\Delta t} \mathbf{F}^{-T} \quad (3.22)$$

Using the increment of stresses, we also know that,

$$\mathbf{S}_t^{t+\Delta t} = \mathbf{S}_t^t + \Delta \mathbf{S} = \boldsymbol{\sigma}^t + \Delta \mathbf{S} \quad (3.23)$$

Substituting Eq. (3.22) in Eq. (3.23) we have,

$$J \mathbf{F}^{-1} \boldsymbol{\sigma}^{t+\Delta t} \mathbf{F}^{-T} = \boldsymbol{\sigma}^t + J \mathbf{F}^{-1} \Delta \boldsymbol{\sigma} \mathbf{F}^{-T} \quad (3.24)$$

which implies that,

$$\boldsymbol{\sigma}^{t+\Delta t} = \frac{1}{J} \mathbf{F} \boldsymbol{\sigma}^t \mathbf{F}^T + \Delta \boldsymbol{\sigma} \quad (3.25)$$

or

$$\boldsymbol{\sigma}_{t+\Delta t}^t = \frac{1}{J} \mathbf{F} \boldsymbol{\sigma}^t \mathbf{F}^T \quad (3.26)$$

3.1.5 THERMO-VISCOPLASTIC STRESS UPDATES

The rate-dependent behaviour of the material is of particular concern in a hot-forming analysis and it necessitates the use of a thermo-viscoplastic constitutive model to accurately capture the material behaviour.

From the definition of the stretch-ratio, we have that,

$$\begin{aligned}\lambda_i &= \frac{l^{t+\Delta t}}{l^t} = \frac{l^t + \Delta l_{mech}^{t+\Delta t} + \Delta l_{th}^{t+\Delta t}}{l^t} \\ &= \frac{l^t + \Delta l_e^{t+\Delta t}}{l^t} \cdot \frac{l^t + \Delta l_e^{t+\Delta t} + \Delta l_{vp}^{t+\Delta t}}{l^t + \Delta l_e^{t+\Delta t}} \cdot \frac{l^t + \Delta l_e^{t+\Delta t} + \Delta l_{vp}^{t+\Delta t} + \Delta l_{th}^{t+\Delta t}}{l^t + \Delta l_e^{t+\Delta t} + \Delta l_{vp}^{t+\Delta t}}\end{aligned}\quad (3.27)$$

Taking logarithms on both sides, we have,

$$\ln(\lambda_i) = \ln\left(\frac{l^t + \Delta l_e^{t+\Delta t}}{l^t}\right) + \ln\left(\frac{l^t + \Delta l_e^{t+\Delta t} + \Delta l_{vp}^{t+\Delta t}}{l^t + \Delta l_e^{t+\Delta t}}\right) + \ln\left(1 + \frac{\Delta l_{th}^{t+\Delta t}}{l_{mech}^{t+\Delta t}}\right)\quad (3.28)$$

where $l_{mech}^{t+\Delta t} = l^t + \Delta l_e^{t+\Delta t} + \Delta l_{vp}^{t+\Delta t}$. Thus using Eq. (3.19), we can have an additive decomposition of the strains, similar to the Prandtl-Reuss equations in the case of inviscid plasticity, as

$$\Delta \boldsymbol{\varepsilon} = \Delta \boldsymbol{\varepsilon}_e + \Delta \boldsymbol{\varepsilon}_{vp} + \Delta \boldsymbol{\varepsilon}_{th}\quad (3.29)$$

where the logarithmic thermal strain in the case of an isotropic material can be defined from Eq. (3.28) as,

$$\Delta \boldsymbol{\varepsilon}_{th} = \ln(1 + \alpha_{th} \Delta T) \mathbf{I}\quad (3.30)$$

where α_{th} is the coefficient of thermal expansion. The stress increment in this case can be

found using the relation,

$$\Delta\boldsymbol{\sigma} = \mathbf{H}^e \Delta\boldsymbol{\varepsilon}_e = \mathbf{H}^e (\Delta\boldsymbol{\varepsilon} - \Delta\boldsymbol{\varepsilon}_{vp} - \Delta\boldsymbol{\varepsilon}_{th}) \quad (3.31)$$

where \mathbf{H}^e is the elasticity tensor.

Strain rate-dependent plasticity models can be classified into two main categories, namely the over-stress models and the consistency model. The over-stress models (Perzyna model [Perzyna, 1966], Duvaut-Lions model, etc) allow the stress state to be outside the yield surface and directly define the plastic relaxation equations in the stress space. Consistency models first proposed by Wang [Wang et al., 1997] and used by others [Wang & Sluys, 2000, Carosio et al., 2000] obtain the viscoplastic regularization by introducing a rate-dependent yield surface. The yield function can expand and shrink not only by hardening or softening effects, but also by hardening rate or softening rate effects. The consistency conditions (or more popularly known as the Karush-Kuhn-Tucker conditions) are not fulfilled in the over-stress models, but is fully satisfied in the consistency model. A comparison of the over-stress models and the consistency models [Heeres et al., 2002, Zaera & Fernández-Sáez, 2006] have shown that :

- The plastic multiplier evolution is explicitly defined in the Perzyna model while its given by a second order differential equation in the consistency model
- During plastic loading both models lead to identical results provided certain conditions are satisfied
- During unloading the Perzyna model leads to plastic deformation since the stress states are allowed to be outside the yield function whereas the consistency model always unloads elastically.
- The consistency model leads to a somewhat higher convergence rate than that derived by the Perzyna model, mainly due to the different unloading characteristics of the models.

In the consistency model, the yield function for a rate-dependent material considering isotropic constitutive law and Von-Mises plasticity can be written as,

$$f(\boldsymbol{\sigma}, \bar{\boldsymbol{\varepsilon}}_{vp}, \dot{\boldsymbol{\varepsilon}}_{vp}, T) = \bar{\sigma} - \sigma_Y(\bar{\boldsymbol{\varepsilon}}_{vp}, \dot{\boldsymbol{\varepsilon}}_{vp}, T) = 0 \quad (3.32)$$

where $\bar{\sigma}$ is the equivalent stress given by $\bar{\sigma} = (\boldsymbol{\sigma}^T \mathbf{P} \boldsymbol{\sigma})^{\frac{1}{2}}$ where $\mathbf{P} =$

$$\begin{bmatrix} 1 & -0.5 & -0.5 & 0 & 0 & 0 \\ -0.5 & 1 & -0.5 & 0 & 0 & 0 \\ -0.5 & -0.5 & 1 & 0 & 0 & 0 \\ 0 & 0 & 0 & 3 & 0 & 0 \\ 0 & 0 & 0 & 0 & 3 & 0 \\ 0 & 0 & 0 & 0 & 0 & 3 \end{bmatrix}$$

and $\sigma_Y(\bar{\boldsymbol{\varepsilon}}_{vp}, \dot{\boldsymbol{\varepsilon}}_{vp}, T)$ is the flow stress corresponding to the accumulated equivalent viscoplastic strain $\bar{\boldsymbol{\varepsilon}}_{vp}$, the equivalent viscoplastic strain rate $\dot{\boldsymbol{\varepsilon}}_{vp}$ and the temperature T .

Similar to the case of inviscid plasticity, the viscoplastic strain rate and the change in viscoplastic strain can be defined as,

$$\begin{aligned} \dot{\boldsymbol{\varepsilon}}_{vp} &= \dot{\lambda} \frac{\partial f}{\partial \boldsymbol{\sigma}} \\ \Delta \boldsymbol{\varepsilon}_{vp} &= \Delta \lambda \frac{\partial f}{\partial \boldsymbol{\sigma}} \end{aligned} \quad (3.33)$$

where $\dot{\lambda}$ is the plastic multiplier rate and can be determined by the consistency condition of the yield surface. In the case of Von-Mises yield criterion, it can be demonstrated that

$$\dot{\bar{\boldsymbol{\varepsilon}}}_{vp} = (\dot{\boldsymbol{\varepsilon}}_{vp}^T \mathbf{A} \dot{\boldsymbol{\varepsilon}}_{vp})^{\frac{1}{2}} = \dot{\lambda} \quad (3.34)$$

where $\mathbf{A} = \frac{4}{9} \begin{bmatrix} 1 & -0.5 & -0.5 & 0 & 0 & 0 \\ -0.5 & 1 & -0.5 & 0 & 0 & 0 \\ -0.5 & -0.5 & 1 & 0 & 0 & 0 \\ 0 & 0 & 0 & 0.75 & 0 & 0 \\ 0 & 0 & 0 & 0 & 0.75 & 0 \\ 0 & 0 & 0 & 0 & 0 & 0.75 \end{bmatrix}$. Using Eqs. (3.31), (3.33) and (3.30), we have,

$$\Delta \boldsymbol{\sigma} = \mathbf{H}^e (\Delta \boldsymbol{\varepsilon} - \Delta \lambda \frac{\partial f}{\partial \boldsymbol{\sigma}} - \ln(1 + \alpha_{th} \Delta T) \mathbf{I}) \quad (3.35)$$

Using an incremental approach as outlined in Eq. (3.25), the stress in the configuration $\Omega^{t+\Delta t}$ can then be computed as,

$$\boldsymbol{\sigma}^{t+\Delta t} = \boldsymbol{\sigma}_{t+\Delta t}^t + \mathbf{H}^e (\Delta \boldsymbol{\varepsilon} - \frac{\Delta \lambda}{\bar{\boldsymbol{\sigma}}_\beta} \mathbf{P} \boldsymbol{\sigma}_\beta - \ln(1 + \alpha_{th} \Delta T) \mathbf{I}) \quad (3.36)$$

where $\boldsymbol{\sigma}_\beta = (1 - \beta) \boldsymbol{\sigma}^t + \beta \boldsymbol{\sigma}^{t+\Delta t}$; β is a parameter between 0 and 1 such that $\beta = 0$ gives an explicit scheme and $\beta = 1$ gives an implicit scheme. The implicit scheme is unconditionally stable and using the implicit scheme, we have,

$$\begin{aligned} \boldsymbol{\sigma}^{t+\Delta t} &= \boldsymbol{\sigma}_{t+\Delta t}^t + \mathbf{H}^e (\Delta \boldsymbol{\varepsilon} - \frac{\Delta \lambda}{\bar{\boldsymbol{\sigma}}^{t+\Delta t}} \mathbf{P} \boldsymbol{\sigma}^{t+\Delta t} - \ln(1 + \alpha_{th} \Delta T) \mathbf{I}) \\ &= \left(\mathbf{I} + \frac{\Delta \lambda}{\bar{\boldsymbol{\sigma}}^{t+\Delta t}} \mathbf{H}^e \mathbf{P} \right)^{-1} (\boldsymbol{\sigma}_{t+\Delta t}^t + \mathbf{H}^e (\Delta \boldsymbol{\varepsilon} - \ln(1 + \alpha_{th} \Delta T) \mathbf{I})) \end{aligned} \quad (3.37)$$

3.1.6 SOLVING ALGORITHM (RETURN MAPPING / DIRECT SCALAR ALGORITHM)

The non-linear problem defined in Eq. (3.37) can be solved using a Return Mapping Algorithm [Simo & Taylor, 1986] or by a Direct Scalar Algorithm [Li et al., 2007, Abbes et al., 2014] extended to the thermo-viscoplastic regime.

The Return Mapping Algorithm based on the Newton-Raphson method is the most widely

used scheme for the plastic integration of constitutive equations. This algorithm follows an elastic-prediction followed by a plastic-correction if $f > 0$. Eq. (3.32) can then be recast into a non-linear function in terms of $\Delta\lambda$ and can be written as $f(\Delta\lambda) = 0$. The Return Mapping Algorithm is computationally expensive due to the iterative process and as is usual for Newton-Raphson iterative schemes, can lead to convergence issues in the case of large increments if a suitable initial value is not assumed.

The Direct Scalar Algorithm proposes a direct scheme for evaluating the plastic integration rate by using the notion of the equivalent stresses. By changing the constitutive equations in terms of unknown stress vectors into scalar equations in terms of equivalent stresses, which can be directly obtained using the tensile curves / plasticity models, we can directly calculate $\Delta\lambda$ without the need for an iterative solution. The direct scalar algorithm is also based upon the elastic-prediction plastic-correction principle.

Assuming that there is no plastic/thermal deformation, a trial stress state can be directly calculated as

$$\boldsymbol{\sigma}_{tr}^{t+\Delta t} = \boldsymbol{\sigma}_{t+\Delta t}^t + \mathbf{H}^e \Delta \boldsymbol{\varepsilon} \quad (3.38)$$

If $f(\bar{\sigma}_{tr}^{t+\Delta t}) \leq 0$, then the elastic prediction is true ($\Delta\lambda = 0$) and plastic correction is not needed; ie, $\boldsymbol{\sigma}^{t+\Delta t} = \boldsymbol{\sigma}_{tr}^{t+\Delta t}$. If $f(\bar{\sigma}_{tr}^{t+\Delta t}) > 0$, the strain increment has a plastic part that needs to be computed. There are different cases that needs to be considered here.

1. A material point with no plastic history passes into a plastic state
2. A material point in a plastic state gets elastically unloaded and then in a subsequent step passes into a plastic state from the elastic state.
3. A material point in a plastic state passes into a plastic state at a different rate of plasticification.

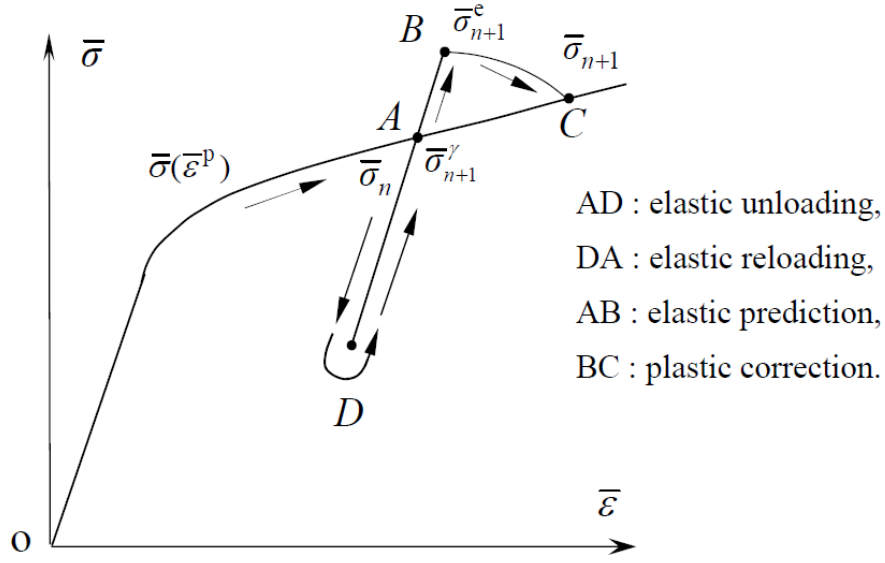


Figure 3.1: Elastic prediction and return mapping

In all the three cases, the total deformation can be split into an elastic part and a plastic part. Denoting by γ the approximate percentage of the elastic strain increment, we can write,

$$\boldsymbol{\sigma}_\gamma^{t+\Delta t} = \boldsymbol{\sigma}_{t+\Delta t}^t + \gamma \mathbf{H}^e \Delta \boldsymbol{\epsilon} \quad (3.39)$$

Using the notion of the equivalent stress, and the solution of a quadratic equation we can directly obtain γ .

$$(\bar{\sigma}_\gamma^{t+\Delta t})^2 = (\bar{\sigma}_{t+\Delta t}^t)^2 + 2\gamma (\boldsymbol{\sigma}_{t+\Delta t}^t)^T \mathbf{P} \mathbf{H}^e \Delta \boldsymbol{\epsilon} + \gamma^2 \Delta \boldsymbol{\epsilon}^T \mathbf{H}^e \mathbf{P} \mathbf{H}^e \Delta \boldsymbol{\epsilon} \quad (3.40)$$

By definition the stress state $\boldsymbol{\sigma}_\gamma^{t+\Delta t}$ should satisfy the Von-Mises criterion and lies on the yield surface at time t . Hence,

$$\bar{\sigma}_\gamma^{t+\Delta t} = \sigma_Y^t \quad (3.41)$$

where σ_Y^t is the yield stress corresponding to the configuration at time t .

Thus γ is the only unknown in (3.40) and can be easily computed from the solution of

the quadratic equation. The equivalent plastic strain in the current step can then be approximated as,

$$\bar{\varepsilon}_{vp}^{t+\Delta t} = \bar{\varepsilon}_{vp}^t + (1 - \gamma)\overline{\Delta\varepsilon} \quad (3.42)$$

The equivalent plastic strain rate can then be computed from the viscoplasticity model that is being used.

Using the notions of equivalent stresses again, from Eq. (3.37) we have,

$$\begin{aligned} (\bar{\sigma}^{t+\Delta t})^2 &= (\bar{\sigma}_{t+\Delta t}^t)^2 + 2\Delta\lambda\bar{\sigma}^{t+\Delta t}\mathbf{n}^T\mathbf{H}^e\mathbf{n} + \Delta\lambda^2\mathbf{n}^T\mathbf{H}^e\mathbf{P}\mathbf{H}^e\mathbf{n} \\ &+ \theta\bar{\sigma}^{t+\Delta t}(\mathbf{n}^T\mathbf{H}^e + \mathbf{H}^e\mathbf{n}) + \Delta\lambda\theta(\mathbf{n}^T\mathbf{H}^e\mathbf{P}\mathbf{H}^e + \mathbf{H}^e\mathbf{P}\mathbf{H}^e\mathbf{n}) + \theta^2\mathbf{H}^e\mathbf{P}\mathbf{H}^e \end{aligned} \quad (3.43)$$

where $\theta = \ln(1 + \alpha_{th}\Delta T)$, \mathbf{n} is the normal to the yield surface at the end of step $t + \Delta t$ and is given as

$$\mathbf{n} = \frac{1}{\bar{\sigma}^{t+\Delta t}} \left[\mathbf{P} \right] \boldsymbol{\sigma}^{t+\Delta t} \approx \frac{1}{\bar{\sigma}_{tr}^{t+\Delta t}} \left[\mathbf{P} \right] \boldsymbol{\sigma}_{tr}^{t+\Delta t}$$

and $\bar{\sigma}^{t+\Delta t} = \sigma_Y^{t+\Delta t}$. With these approximations, the only unknown in Eq. (3.43) becomes $\Delta\lambda$ and can be computed easily by solving Eq. (3.43).

Clearly the $\Delta\lambda$ obtained by this method is an approximation, but an analysis of the results from the Direct algorithm and the Return Mapping Algorithm indicate that the difference between the two methods is negligible especially in cases of proportional loading. For higher accuracy, the $\Delta\lambda$ obtained can be taken as an initial value for the classical return mapping algorithm and solved iteratively using a Newton-Raphson method.

3.2 PRACTICAL IMPLEMENTATION

In the previous section, the mathematical basis of the Pseudo Inverse Approach has been established. The practical implementation of the Pseudo Inverse Approach can be described

succinctly in the flowchart in Fig. (3.2).

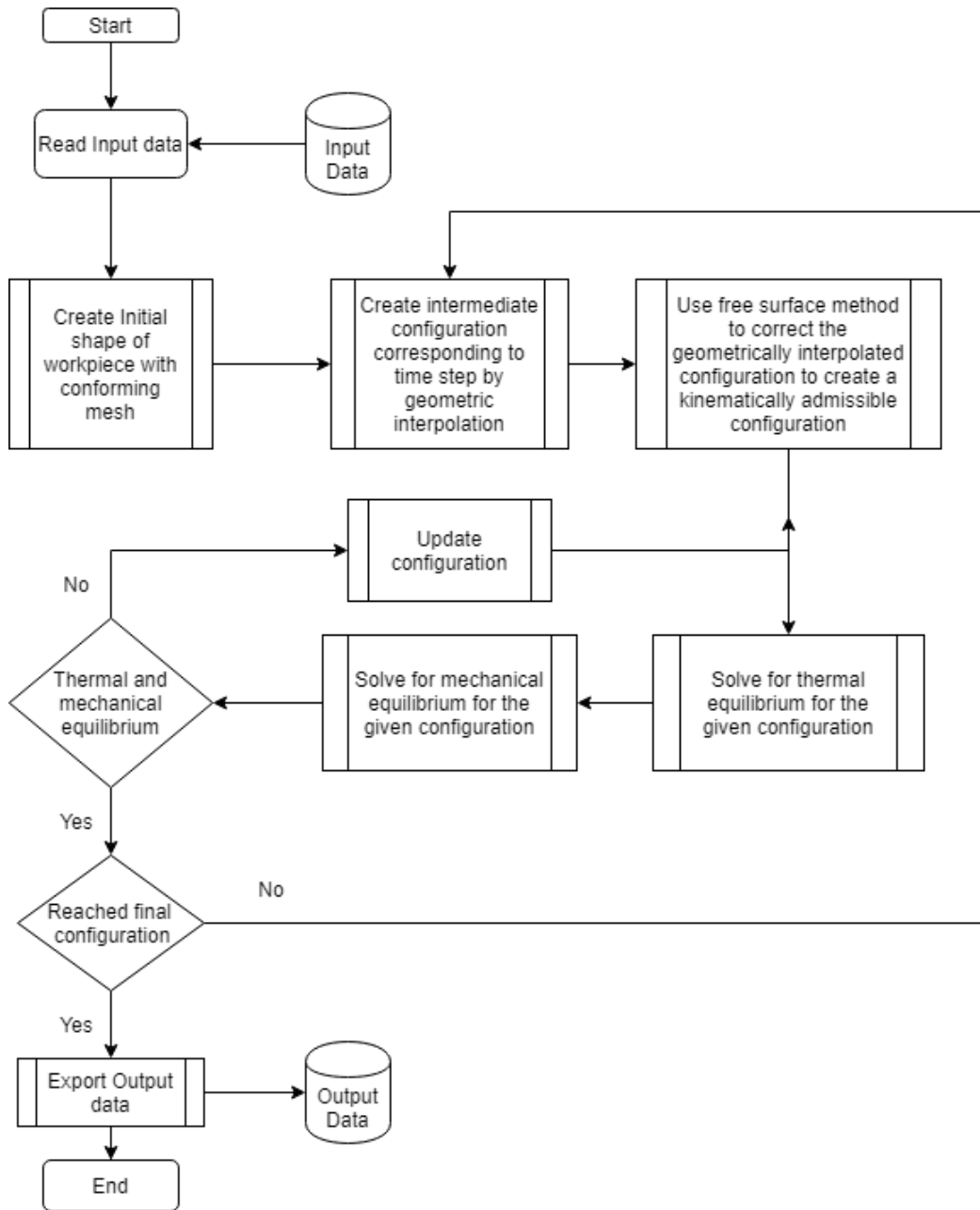


Figure 3.2: Flowchart - PIA

The entire process can be split into mainly three phases:

- I. Generation of intermediate configurations

2. Free surface correction of geometrically interpolated configurations to obtain kinematically admissible configurations
3. Searching a statically admissible solution for the equilibrium based upon the kinematically admissible configuration that has been computed.

3.2.1 GENERATION OF INTERMEDIATE CONFIGURATIONS

The creation of intermediate shapes in the Pseudo Inverse Approach is based on a geometrical interpolation between the initial/intermediate shapes and the target shape. This imposes a restriction that the finite element meshes used in both the target shape and the initial shape should be consistent (equal number of nodes and the same element connectivity). The initial shape is either assumed or found out from a single-step inverse approach. The shape obtained from the single step inverse approach has been shown to have a good approximation for shapes and strains even though the stress predictions are not quite accurate. The finite element mesh of the desired part is then mapped onto the initial shape. This is done by mapping the contour nodes of the mesh M^{fin} of the desired shape onto the contour C^0 of the initial shape. This can be efficiently done using mesh morphing algorithms in use. The interior nodes of the mesh M^0 can then be determined by a linear solution of the mechanical equilibrium with the imposed displacements on the boundary nodes as the boundary conditions.

Once the conforming meshes have been created in the initial shape, the intermediate configuration can be created by using a geometric proportional interpolation of the form,

$$\mathbf{x}^{t+\Delta t} = \mathbf{x}^t + \eta (\mathbf{x}^{fin} - \mathbf{x}^t) \quad (3.44)$$

where $\mathbf{x}^{t+\Delta t}$ is the nodal position of the configuration at time $t + \Delta t$, \mathbf{x}^t is the nodal position of the configuration at time t , \mathbf{x}^{fin} is the nodal positions of the final configuration

and η is a constant between $[0,1]$ and is dependent on the total no. of steps that is considered in the simulation.

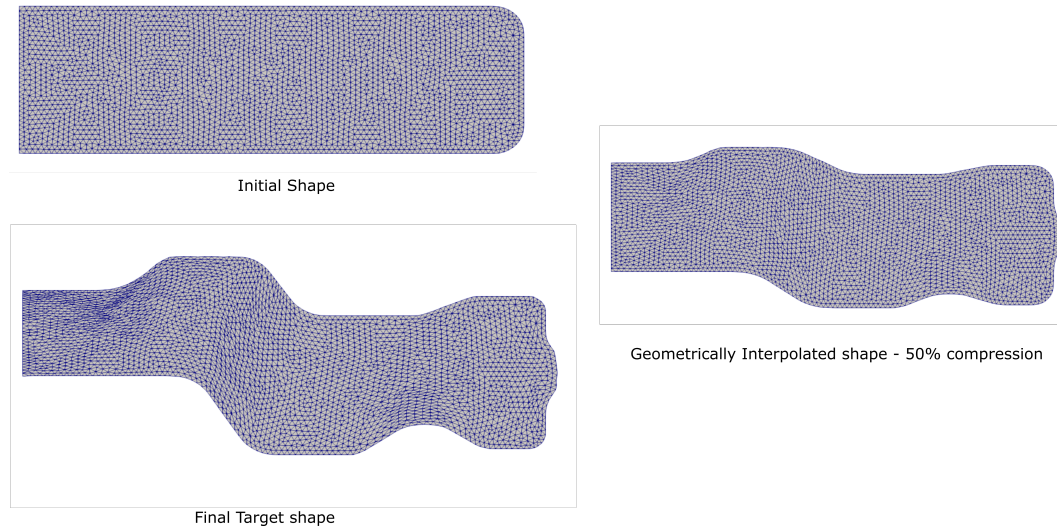


Figure 3.3: Generation of a geometrically proportionate intermediate configuration

3.2.2 FREE SURFACE CORRECTION AND BOUNDARY CONDITIONS

One limitation of this geometrically interpolated configuration is that the boundary conditions (contact conditions) with respect to the tool positions may not be respected on the contour. To correct this limitation and to obtain a kinematically admissible solution that is close to the statically admissible solution, the boundary nodes of the workpiece that penetrate the tool surface are projected back onto the tool surface using a node-to-element projection and subsequently a linear solution is carried out to determine the new positions of the internal nodes. Assuming rigid tools, it is trivial to compute the tool position corresponding to the time-step under consideration. Since these nodes are projected onto the tool surface, these are implicitly assumed to be in contact with the tool. But in a practical situation this need not be true and the contact conditions at the surface nodes needs to be verified. For this, we make use of the free-surface method. In a metal-forming operation simulation, for any

configuration Ω , the free-surface condition can be expressed as,

$$\boldsymbol{\sigma} \mathbf{n} = \mathbf{t} \leq 0 \quad \text{on } \partial\Omega \quad (3.45)$$

where \mathbf{t} is the traction force in the outward normal direction from the workpiece surface. This means that there is a compressive loading on the boundary in contact with the tool and no loading on the surface that is free from contact with the tool surface. To verify that the free surface conditions are respected, the nodal forces are computed on the geometrically interpolated/corrected configuration. Using u , v and w to denote the components of the nodal displacement in the normal and tangential directions respectively, the following cases can be considered.

1. If $t_u \geq 0$, then the node belongs to the free surface and the boundary conditions on the node can be represented as $u \neq 0$; $v \neq 0$; $w \neq 0$
2. If $t_u < 0$, then the node is in contact with the tool surface (compressive force) and the boundary conditions on the node can be represented as $u = 0$; $v \neq 0$; $w \neq 0$

The linear solution is done iteratively till the contact conditions are also satisfied and the kinematically admissible configuration is obtained.

Once a kinematically admissible configuration is obtained, the statically admissible equilibrium configuration that satisfies both the thermal and mechanical equilibrium is found out using the mathematical formulation of the PIA. For maintaining the accuracy, verification of the contact conditions using the free surface method is conducted during the mechanical equilibrium computations also.

3.2.3 CO-ORDINATE TRANSFORMATIONS

Since the boundary conditions and the free surface correction conditions are defined in the normal directions at every boundary node, it is imperative to define the normals and tangents to the boundary nodes. This is made possible by defining the spherical-polar coordinates (in

3D) and the cylindrical-polar local co-ordinates (in 2D axisymmetric) at the boundary nodes as shown in Fig. (3.4).

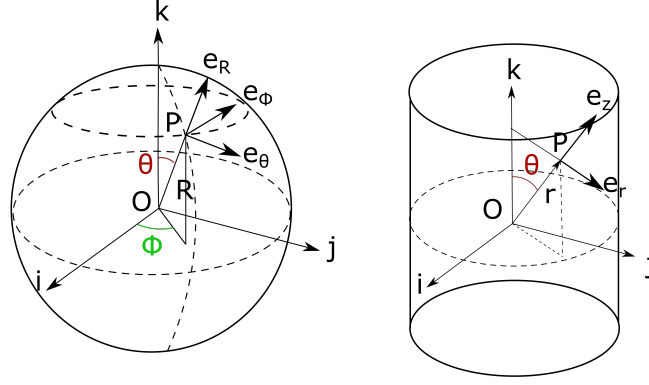


Figure 3.4: Spherical-polar and Cylindrical-polar Coordinates

For every boundary node in contact with the tool surface, the normal at the node is taken to be pointing in the opposite direction to the surface normal at the tool and the tangents lie on the surface of the tool. Subsequently a rotation matrix can be defined for rotating any vector component at the node into the Cartesian basis such that, if

$\mathbf{a} = a_R \mathbf{e}_R + a_\theta \mathbf{e}_\theta + a_\phi \mathbf{e}_\phi$ is a vector in the local with components (a_R, a_θ, a_ϕ) in the spherical-polar basis $\{\mathbf{e}_R, \mathbf{e}_\theta, \mathbf{e}_\phi\}$ and its corresponding components in the Cartesian basis $\{\mathbf{i}, \mathbf{j}, \mathbf{k}\}$ is given by (a_x, a_y, a_z) , then the relation between the two sets of components can be given by,

$$\begin{bmatrix} a_x \\ a_y \\ a_z \end{bmatrix} = \begin{bmatrix} \sin\theta \cos\phi & \cos\theta \cos\phi & -\sin\phi \\ \sin\theta \sin\phi & \cos\theta \sin\phi & \cos\phi \\ \cos\theta & -\sin\theta & 0 \end{bmatrix} \begin{bmatrix} a_R \\ a_\theta \\ a_\phi \end{bmatrix} \quad (3.46)$$

while the inverse relationship is given by,

$$\begin{bmatrix} a_R \\ a_\theta \\ a_\phi \end{bmatrix} = \begin{bmatrix} \sin\theta\cos\phi & \sin\theta\sin\phi & \cos\theta \\ \cos\theta\cos\phi & \cos\theta\sin\phi & -\sin\theta \\ -\sin\phi & \cos\phi & 0 \end{bmatrix} \begin{bmatrix} a_x \\ a_y \\ a_z \end{bmatrix} \quad (3.47)$$

Note that the 3×3 matrices involved in this transformation are orthogonal satisfying $\mathbf{Q}\mathbf{Q}^T = \mathbf{I}$, where \mathbf{I} denotes the identity matrix.

The equivalent transformation in the cylindrical-polar co-ordinate system is given by,

$$\begin{bmatrix} a_x \\ a_y \\ a_z \end{bmatrix} = \begin{bmatrix} \cos\theta & -\sin\theta & 0 \\ \sin\theta & \cos\theta & 0 \\ 0 & 0 & 1 \end{bmatrix} \begin{bmatrix} a_r \\ a_\theta \\ a_z \end{bmatrix} \quad (3.48)$$

and the inverse transformation is given by,

$$\begin{bmatrix} a_r \\ a_\theta \\ a_z \end{bmatrix} = \begin{bmatrix} \cos\theta & \sin\theta & 0 \\ -\sin\theta & \cos\theta & 0 \\ 0 & 0 & 1 \end{bmatrix} \begin{bmatrix} a_x \\ a_y \\ a_z \end{bmatrix} \quad (3.49)$$

where (a_r, a_θ, a_z) are the components in the cylindrical-polar basis $\{\mathbf{e}_r, \mathbf{e}_\theta, \mathbf{e}_z\}$ and (a_x, a_y, a_z) are the components in the Cartesian basis $\{\mathbf{i}, \mathbf{j}, \mathbf{k}\}$.

Since the boundary conditions are defined in the local co-ordinate system, the computations are carried out in the local system and the stresses and strains are computed in the local co-ordinate systems, it is necessary to define the transformation of the tensors as well. If \mathbf{S} is a tensor with components,

$$\mathbf{S} \equiv \begin{bmatrix} S_{RR} & S_{R\theta} & S_{R\phi} \\ S_{\theta R} & S_{\theta\theta} & S_{\theta\phi} \\ S_{\phi R} & S_{\phi\theta} & S_{\phi\phi} \end{bmatrix} \equiv \begin{bmatrix} S_{xx} & S_{xy} & S_{xz} \\ S_{yx} & S_{yy} & S_{yz} \\ S_{zx} & S_{zy} & S_{zz} \end{bmatrix}$$

in the spherical-polar basis $\{\mathbf{e}_R, \mathbf{e}_\theta, \mathbf{e}_\phi\}$ and the Cartesian basis $\{\mathbf{i}, \mathbf{j}, \mathbf{k}\}$ respectively. The two sets of components are related by,

$$\begin{bmatrix} S_{xx} & S_{xy} & S_{xz} \\ S_{yx} & S_{yy} & S_{yz} \\ S_{zx} & S_{zy} & S_{zz} \end{bmatrix} = [\mathbf{R}_M] \begin{bmatrix} S_{RR} & S_{R\theta} & S_{R\phi} \\ S_{\theta R} & S_{\theta\theta} & S_{\theta\phi} \\ S_{\phi R} & S_{\phi\theta} & S_{\phi\phi} \end{bmatrix} [\mathbf{R}_M] \quad (3.50)$$

and

$$\begin{bmatrix} S_{RR} & S_{R\theta} & S_{R\phi} \\ S_{\theta R} & S_{\theta\theta} & S_{\theta\phi} \\ S_{\phi R} & S_{\phi\theta} & S_{\phi\phi} \end{bmatrix} = [\mathbf{R}_M^T] \begin{bmatrix} S_{xx} & S_{xy} & S_{xz} \\ S_{yx} & S_{yy} & S_{yz} \\ S_{zx} & S_{zy} & S_{zz} \end{bmatrix} [\mathbf{R}_M^T] \quad (3.51)$$

where $[\mathbf{R}_M] = \begin{bmatrix} \sin\theta\cos\phi & \cos\theta\cos\phi & -\sin\phi \\ \sin\theta\sin\phi & \cos\theta\sin\phi & \cos\phi \\ \cos\theta & -\sin\theta & 0 \end{bmatrix}$ is the orthogonal rotation matrix.

Similarly for the cylindrical-polar basis, the two components are related by,

$$\begin{bmatrix} S_{xx} & S_{xy} & S_{xz} \\ S_{yx} & S_{yy} & S_{yz} \\ S_{zx} & S_{zy} & S_{zz} \end{bmatrix} = [\mathbf{R}_M] \begin{bmatrix} S_{rr} & S_{r\theta} & S_{rz} \\ S_{\theta r} & S_{\theta\theta} & S_{\theta z} \\ S_{zr} & S_{z\theta} & S_{zz} \end{bmatrix} [\mathbf{R}_M] \quad (3.52)$$

and,

$$\begin{bmatrix} S_{rr} & S_{r\theta} & S_{rz} \\ S_{\theta r} & S_{\theta\theta} & S_{\theta z} \\ S_{zr} & S_{z\theta} & S_{zz} \end{bmatrix} = [\mathbf{R}_M^T] \begin{bmatrix} S_{xx} & S_{xy} & S_{xz} \\ S_{yx} & S_{yy} & S_{yz} \\ S_{zx} & S_{zy} & S_{zz} \end{bmatrix} [\mathbf{R}_M^T] \quad (3.53)$$

where $[\mathbf{R}_M] = \begin{bmatrix} \cos\theta & -\sin\theta & 0 \\ \sin\theta & \cos\theta & 0 \\ 0 & 0 & 1 \end{bmatrix}$.

Those who claim to discover everything but produce no proofs of the same may be confuted as having actually pretended to discover the impossible.

Aristotle

4

Simulation Results & Discussion

FROM the theoretical basis of the Pseudo Inverse Approach that has been introduced in the previous chapter, we have proposed a method that is able to handle finite deformations that are not limited by the limitations of a conventional incremental method. Also, since the PIA takes into account the incremental strain hardening, it should be able to ensure the accuracy of the results as well. For confirming this hypothesis, forging simulations of various parts have been done and the results obtained from the PIA is compared with those obtained from commercial software for the validation of the results. The results primarily focus on the thermo-viscoplastic behaviour and the computational efficiency of the procedure. Forging simulations of both 2D axisymmetric and general 3D components are considered.

4.1 THERMO-VISCOPLASTIC MODELS

For the hot forging analysis, it is imperative to consider the thermo-viscoplastic behaviour of the material. Various empirical and semi-empirical models are in use in the industry for modelling the thermo-viscoplastic behaviour and one of the most popular models is the Johnson-Cook model [Johnson & Cook, 1983]. The empirical formulation proposed by Johnson and Cook is used in all the examples treated in this work although the formulations can be valid for any hardening rule of the form $\sigma_Y(\bar{\varepsilon}_{vp}, \dot{\varepsilon}_{vp}, T)$. The Johnson-Cook model can be stated as,

$$\sigma_Y(\bar{\varepsilon}_{vp}, \dot{\varepsilon}_{vp}, T) = [A + B(\bar{\varepsilon}_{vp})^n] \left[1 + C \log \left(\frac{\dot{\varepsilon}_{vp}}{\dot{\varepsilon}_0} \right) \right] \left[1 - \left(\frac{T - T_0}{T_m - T_0} \right)^m \right] \quad (4.1)$$

where A, B, C, m and n are the Johnson-Cook model parameters, $\dot{\varepsilon}_0$ is the reference viscoplastic strain rate, T_m is the melting temperature of the material and T_0 is the reference temperature.

It has to be noted that for $\dot{\varepsilon}_{vp} < \dot{\varepsilon}_0$, rate sensitivity need not be taken into account [Zaera & Fernández-Sáez, 2006]. Hence the Johnson-Cook relation should be more properly defined as

$$\sigma_Y = \begin{cases} [A + B(\bar{\varepsilon}_{vp})^n] \left[1 + C \log \left(\frac{\dot{\varepsilon}_{vp}}{\dot{\varepsilon}_0} \right) \right] \left[1 - \left(\frac{T - T_0}{T_m - T_0} \right)^m \right] & \text{if } \dot{\varepsilon}_{vp} \geq \dot{\varepsilon}_0 \\ [A + B(\bar{\varepsilon}_{vp})^n] \left[1 - \left(\frac{T - T_0}{T_m - T_0} \right)^m \right] & \text{if } \dot{\varepsilon}_{vp} < \dot{\varepsilon}_0 \end{cases} \quad (4.2)$$

This leads to a discontinuity in the hardening relation and has to be kept in mind when using iterative return mapping methods for the solution process, to guarantee convergence.

When $\bar{\epsilon}_{vp}$ and σ are known, the plastic strain rate can be computed using this relation as,

$$\dot{\bar{\epsilon}}_{vp} = \dot{\bar{\epsilon}}_0 \exp \left[\frac{1}{C} \frac{\sigma_P - \bar{\sigma}}{\sigma_P} \right] \quad (4.3)$$

where, $\sigma_P = A + B(\bar{\epsilon}_{vp})^n$. When using other models that cannot give a direct empirical formula to compute the plastic strain rate, it can be estimated as $\dot{\bar{\epsilon}}_{vp} = \Delta\bar{\epsilon}_{vp}/\Delta t$.

4.2 SIMULATION RESULTS

4.2.1 2D AXISYMMETRIC SCREW

It is a common practice in academia as well as the industry to use the symmetric properties of the problem being considered to reduce the computational effort. Axisymmetric analysis are often conducted for components that have at least one axis of symmetry. For our initial comparison, we make use of the forming analysis of an axisymmetric screw. The target shape and the initial shape of the workpiece and the tools used can be seen in Fig. (4.1).

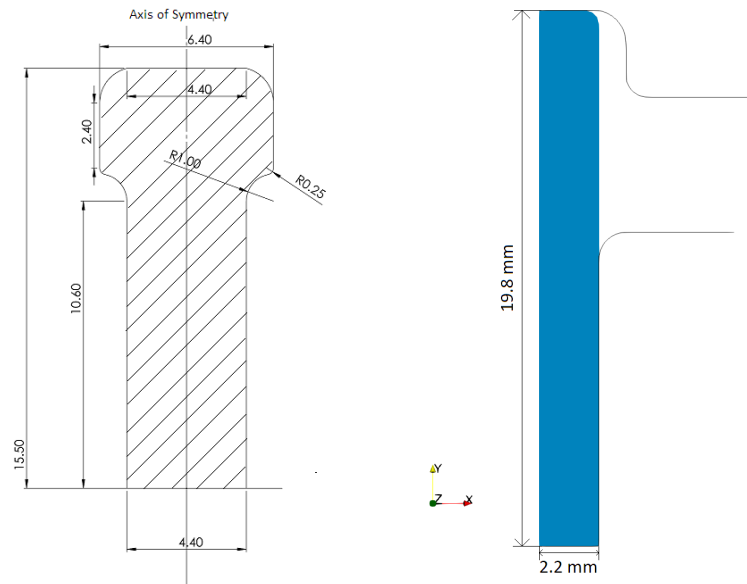


Figure 4.1: Forging of a screw a) Target shape b) Initial billet and tools

For the purposes of the simulation, the workpiece is discretised using 878 nodes and 1578 elements (Type CAX3T, Abaqus). The tools are considered to be rigid and the contact between the tools and the workpiece are assumed to be friction-less.

The workpiece is considered to be made of 12Kh18Ni0T steel with the following properties [Stankus et al., 2008, Sobolev & Radchenko, 2016].

Density, $\rho = 7930 \text{ Kg m}^{-3}$, Young's Modulus, $E = 195 \text{ GPa}$, Poisson's ratio, $\nu = 0.28$, Specific heat capacity, $c = 462 \text{ J Kg}^{-1} \text{ K}^{-1}$, Conductivity, $k = 25 \text{ W m}^{-1} \text{ K}^{-1}$, Melting temperature, $T_m = 1300^\circ\text{C}$, initial temperature of the workpiece, $T = 1000^\circ\text{C}$. The workpiece material is considered to follow a Johnson-Cook viscoplastic model with parameters $A = 196 \text{ MPa}$, $B = 615.5 \text{ MPa}$, $n = 0.7005$, $C = 0.04071$, $m = 1.479$ and $\dot{\epsilon}_0 = 0.0001 \text{ s}^{-1}$. The tools are considered to be iso-thermal with a constant temperature of $T_d = 750^\circ\text{C}$ while the ambient temperature T_a is considered to be 20°C . The workpiece material is considered to have a heat transfer coefficient $h_{wd} = 310 \text{ W m}^{-2} \text{ K}^{-1}$ with respect to the tools and $h_{wa} = 50 \text{ W m}^{-2} \text{ K}^{-1}$ with respect to the ambient environment. Radiation effects and inelastic heat fraction is not taken into consideration for the initial analysis.

The punch is given a movement of 4.4mm in the negative Y-direction while the bottom die is considered to be stationary. The process time is considered to be 1 second and the results obtained from ABAQUS[®]/Explicit and PIA are compared below. For the purpose of having a one-to-one comparison of the results, the target shape used in PIA is the final deformed shape obtained from the reference simulation.

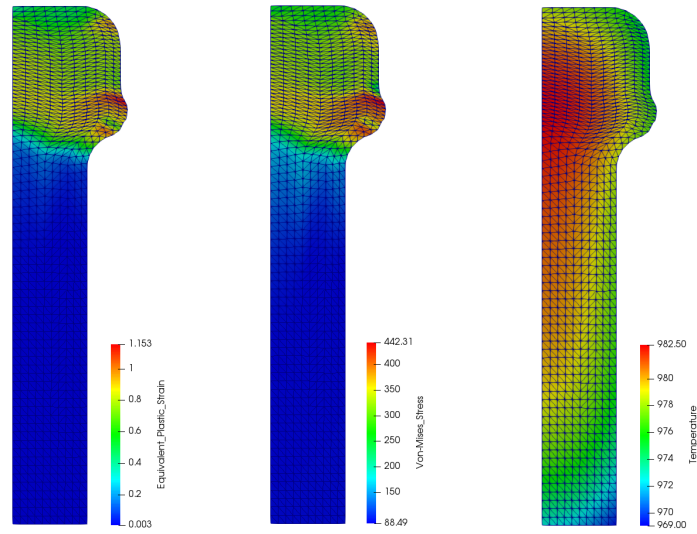


Figure 4.2: Reference results obtained from ABAQUS® Explicit- Axisymmetric Screw

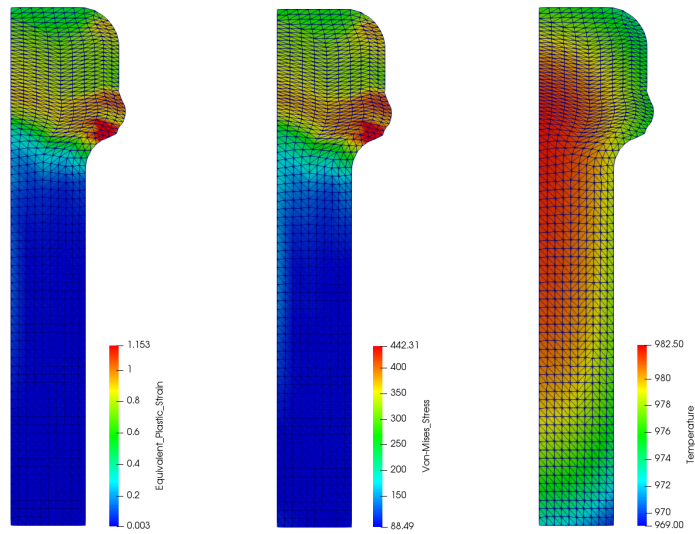


Figure 4.3: Results obtained from PIA - Axisymmetric Screw (15 steps)

As can be seen from the results presented in Fig. (4.2) and Fig. (4.3), the results obtained from PIA compare very favourably with the reference results. The average percentage error in the results maybe computed by considering that the $error \% = \frac{Reference\ value - PIA\ result}{Reference\ value}$. The error in the maximum value of the computed stress is 6.35% , in maximum equivalent

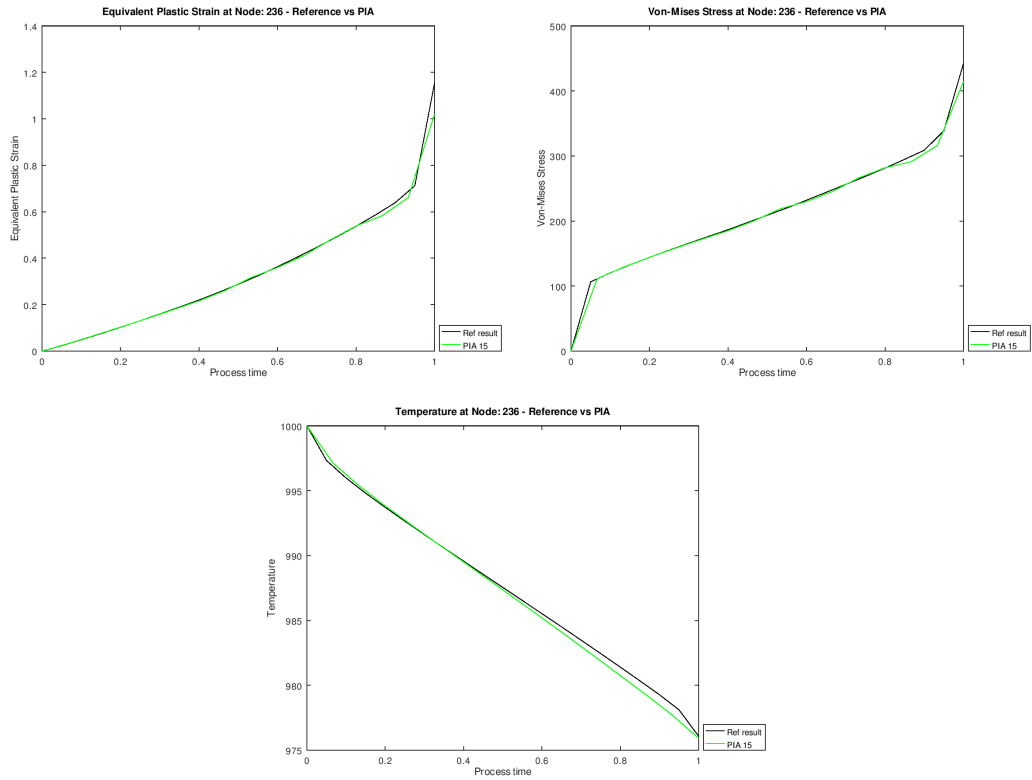


Figure 4.4: Evolution of field values at Node 236 - Axisymmetric Screw. a) Equivalent Plastic Strain b) Von-Mises Stress c) Temperature

plasticity is 11.65% and in maximum temperature value is 0.05%. It is also seen that the PIA captures the evolution of the stress, strain and temperature quite well. This is illustrated in Fig. (4.4) where we compare the evolution of the equivalent plastic strain, Von-Mises Stress and temperature at node 236, which is the node where we have the maximum stress/equivalent plastic strain.

One important effect in the hot forging process is the conversion of plastic work into thermal energy. If we consider a Taylor-Quinney coefficient (inelastic heat fraction) of 0.9, we get results as seen in Fig. (4.5).

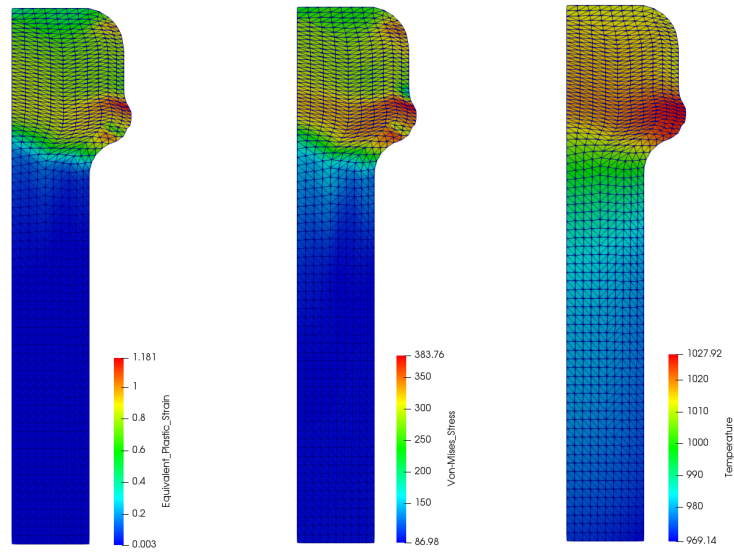


Figure 4.5: Reference results obtained from ABAQUS[®] Explicit- Axisymmetric screw with Inelastic heat fraction

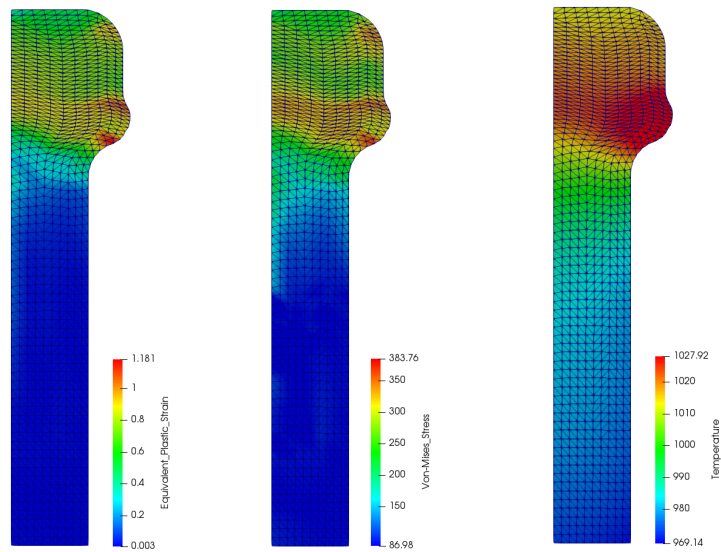


Figure 4.6: Results obtained from PIA - Axisymmetric screw with Inelastic heat fraction (30steps)

As can be immediately inferred from the results presented in Fig. (4.5) and Fig. (4.6), the temperature values predicted from the PIA is much higher than the reference results. A proportionate effect is seen in the predicted stress values also due to the effect of the predicted

temperature. Also it is seen that for convergence, a higher number of steps (30 steps) is required, mainly due to the effects of the temperature. The error in the maximum value of the computed stress is 9.27% , in maximum value of equivalent plasticity is 11.25% and in maximum temperature value is 1.12%. This higher error is due to the effect of the large step sizes used in PIA. Since we consider a larger step size, the effect of the plastic work is more prominent in that step and gets diffused throughout the body. To verify this conclusion, the same analysis was made by considering a larger number of steps (80 steps) for the PIA and the results of the same can be seen in Fig. (4.7).

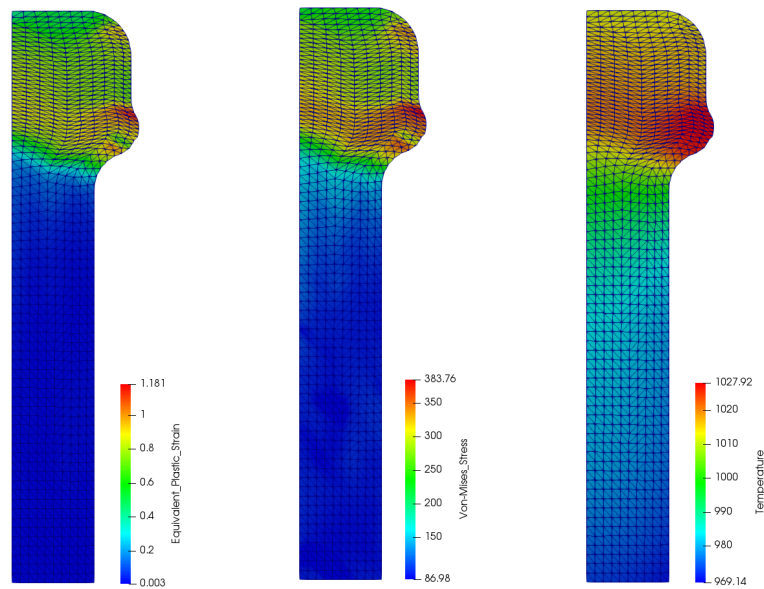


Figure 4.7: Results from 80 steps PIA - Axisymmetric Screw with Inelastic heat fraction

It is immediately evident that the results obtained from PIA with a larger number of steps compare more favourably with the reference results and confirms the hypothesis that the difference between the reference results and the results obtained from PIA with a much lower number of steps in Fig. (4.6) is indeed due to the large step size effect. The error in the maximum value of the computed stress is 0.74% , in maximum equivalent plasticity is 3.28% and in maximum temperature value is 0.23%.

The effect of the step sizes is better captured by considering the evolution of the field values

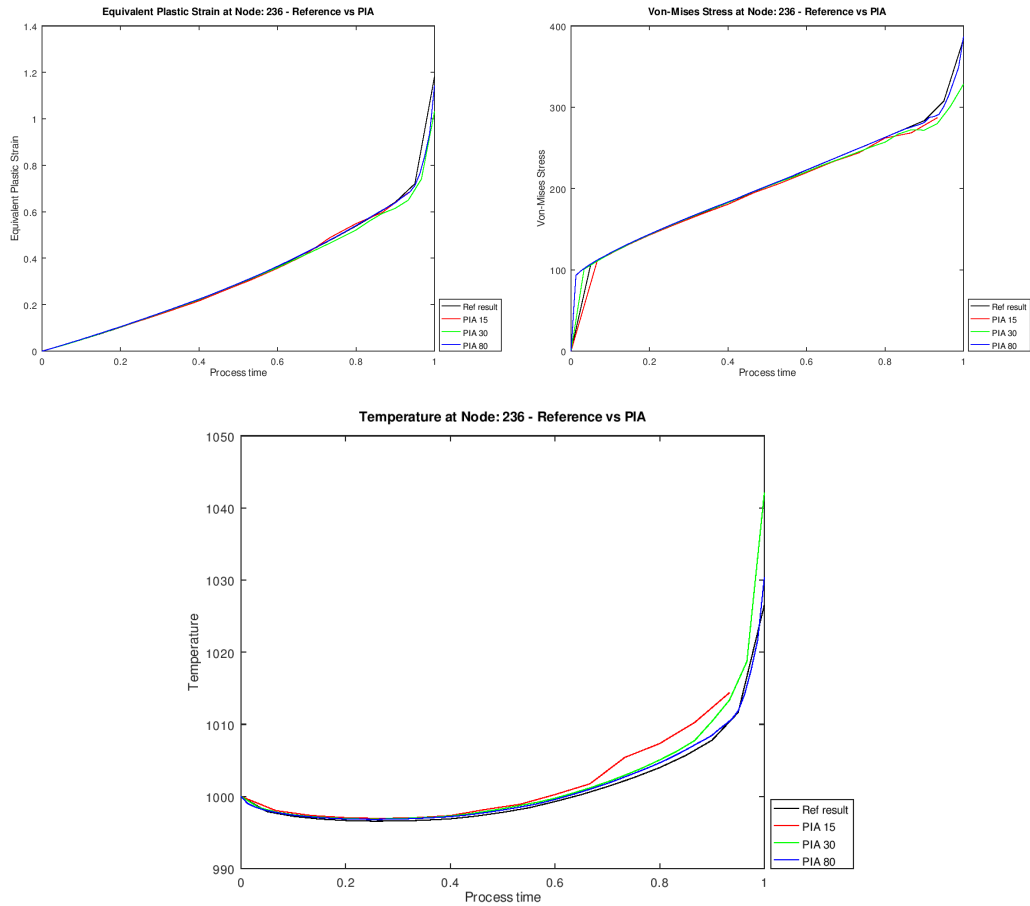


Figure 4.8: Evolution of field values at Node 236 - Axisymmetric Screw including inelastic work. a)Equivalent Plastic Strain b) Von-Mises Stress c) Temperature

at a node for the different cases. We consider 3 different case for the PIA including 15 steps, 30 steps and 80 steps and the evolution of the field variables is plotted in Fig. (4.8).

As can be seen from the plots, the analysis using 15 steps in PIA does not get completed as the simulation crashes at around 93% due to the predicted temperature exceeding the melting temperature. The simulation with 30 steps gets completed but the temperature field is over-predicted due to the large step-size effect. This in-turn affects the prediction of the stress field and consequently we see a lower stress when using just 30 steps. The simulation with 80 steps in PIA mitigates the step-size effect and hence gives results that have a very good co-relation with that of the reference results. The equivalent plastic strain predicted by PIA in all 3 cases

remain pretty much constant. This underlines the fact that the step-size effects due to the use of large steps is limited to the temperature field prediction and the consequent effect on the stress field prediction. This effect will not play a role in cold-forging simulations using PIA.

4.2.2 2D AXISYMMETRIC WHEEL

As can be seen with the model in Sec. (4.2.1) there are differences in the temperature and stress fields when the inelastic heat fraction is taken into account. The effect of contact and the large step sizes cannot be easily identified in this example since the area where an evolution of contact happens is relatively small. To investigate the effect of the contact evolution and the subsequent changes in the solution, another example of an axisymmetric wheel is taken. The target shape of the wheel is shown in Fig. (4.9). The initial shape of the workpiece used and the tools used for the process can be found in Fig. (4.10).

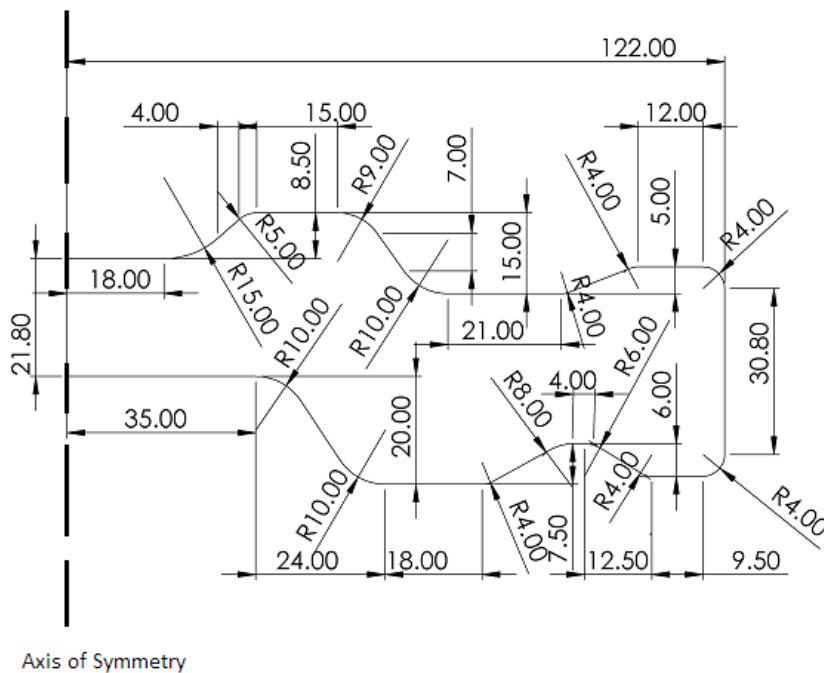


Figure 4.9: Target shape of the wheel

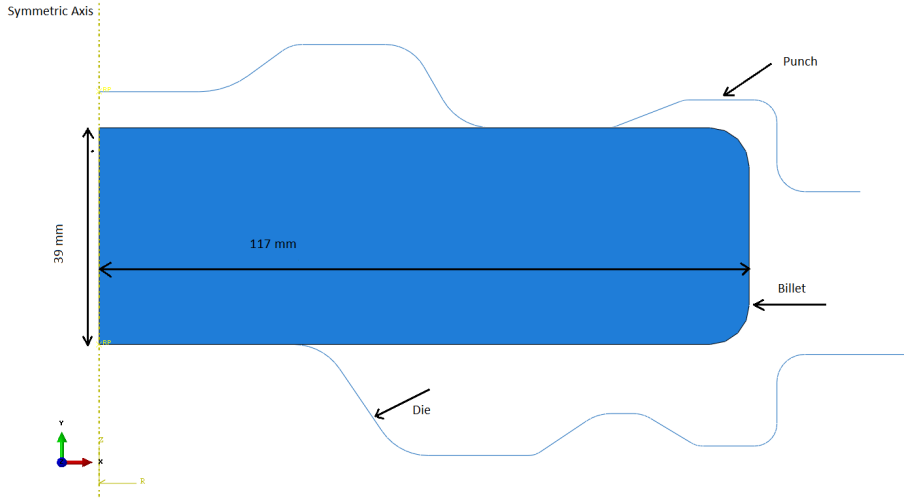


Figure 4.10: Tools and workpiece used for forging the 2D axisymmetric wheel

For the purposes of the study, the workpiece is discretised by 3123 nodes and 5999 elements (Type CAX3T, Abaqus). The tools are considered to be rigid and friction-less contact is assumed on the contact surfaces. The workpiece is considered to be made of aluminium with the following properties [Corona & Orient, 2014].

Density, $\rho = 2810 \text{ Kg m}^{-3}$, Young's Modulus, $E = 71.7 \text{ GPa}$, Poisson's ratio, $\nu = 0.33$, Specific heat capacity, $c = 960 \text{ JK g}^{-1} \text{ K}^{-1}$, Conductivity, $k = 205 \text{ W m}^{-1} \text{ K}^{-1}$, Melting temperature, $T_m = 477^\circ\text{C}$, initial temperature of the workpiece, $T = 400^\circ\text{C}$. The workpiece material is considered to follow a Johnson-Cook viscoplastic model with parameters $A = 517 \text{ MPa}$, $B = 405 \text{ MPa}$, $n = 0.41$, $C = 0.0075$, $m = 1.1$ and $\dot{\epsilon}_0 = 0.000161 \text{ s}^{-1}$. The tools are considered to be iso-thermal with a constant temperature of $T_d = 250^\circ\text{C}$ while the ambient temperature T_a is considered to be 25°C . The workpiece material is considered to have a heat transfer coefficient $h_{wd} = 310 \text{ W m}^{-2} \text{ K}^{-1}$ with respect to the tools, $h_{wa} = 50 \text{ W m}^{-2} \text{ K}^{-1}$ with respect to the ambient environment and Taylor-Quinney coefficient for the inelastic heat fraction $\kappa = 0.9$.

The punch is given a movement of 23.7mm in the negative Y-direction while the bottom die is considered to be stationary and the process time is considered to be 1 second.

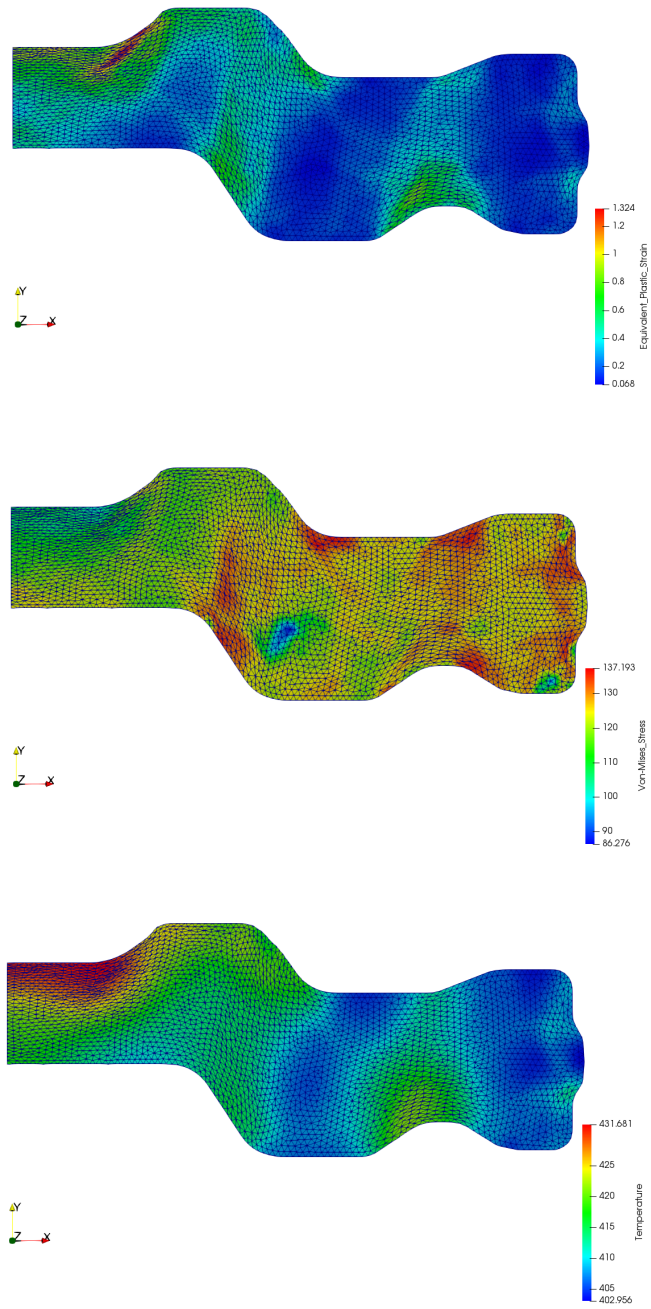


Figure 4.11: Reference results - Axisymmetric Wheel. a) Equivalent Plastic Strain b) Von-Mises Stress c) Temperature

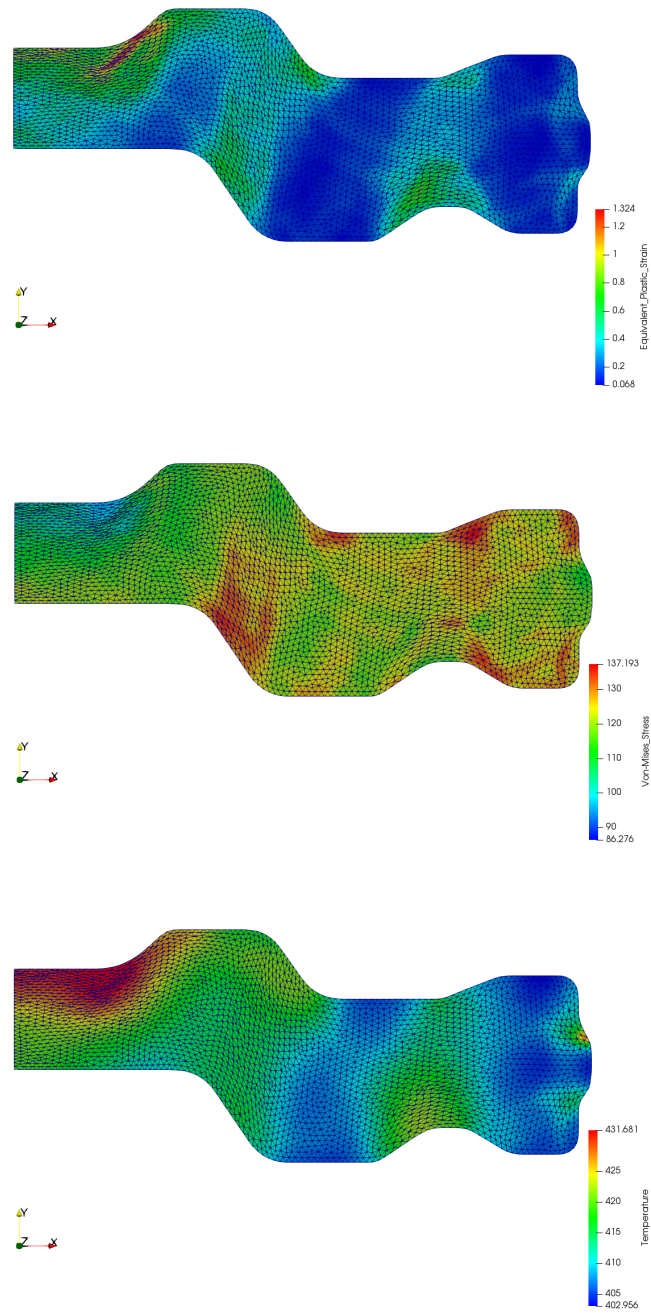


Figure 4.12: PIA results 25 steps - Axisymmetric Wheel. a) Equivalent Plastic Strain b) Von-Mises Stress c) Temperature

Fig. (4.11) shows results obtained from the reference simulation and Fig. (4.12) shows the results obtained from PIA. A comparison of the reference results and the results obtained by

PIA show that the results obtained from PIA are very close to those obtained in the reference simulation. The average error in the computed Von-Mises stress is 2.11% , in the computed Equivalent Plastic Strain is 10.99% and in the temperature value is 0.11%. As is quite evident from the comparison plots, the PIA is able to provide a good approximation of the field values accounting for the step-size effects.

EFFECT OF TIME STEPS AND INELASTIC HEAT FRACTION

To study the effects of the effect of the number of steps and the inelastic heat fraction in the prediction of the temperature and the consequent changes in the predicted Von-Mises stress and the equivalent plastic strains, the evolution of the field values at a node inside the element is done for different load cases as detailed in Table. (4.1).

Case Name	Process Time (sec)	Inelastic heat fraction
Case 1	0.1	0.9
Case 2	1	0.9
Case 3	10	0.9
Case 4	10	0.0

Table 4.1: Test cases - Specifications

The field values at node number 965 is extracted since it is the node with the highest temperature values in almost all of the case studied. The results from the Reference simulation and PIA is presented in Figs. (4.13,4.14,4.15). The solid lines represent the solution obtained from the reference simulations while the dotted lines represent the solution obtained from PIA.

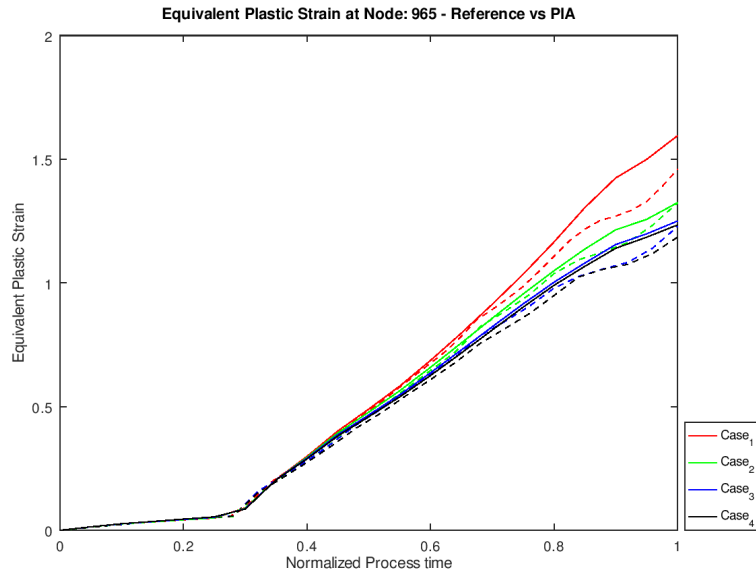


Figure 4.13: Evolution of field values at node 965 - Equivalent Plastic Strain (PEEQ)

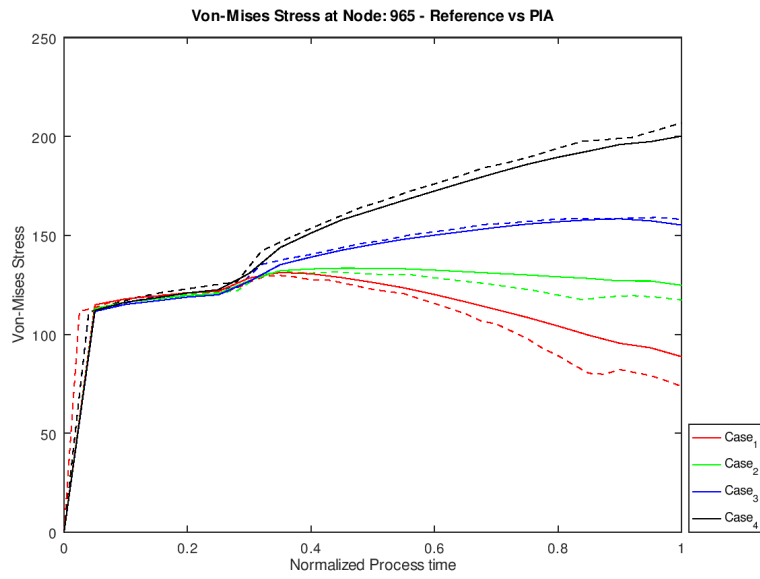


Figure 4.14: Evolution of field values at node 965- Von-Mises Stress

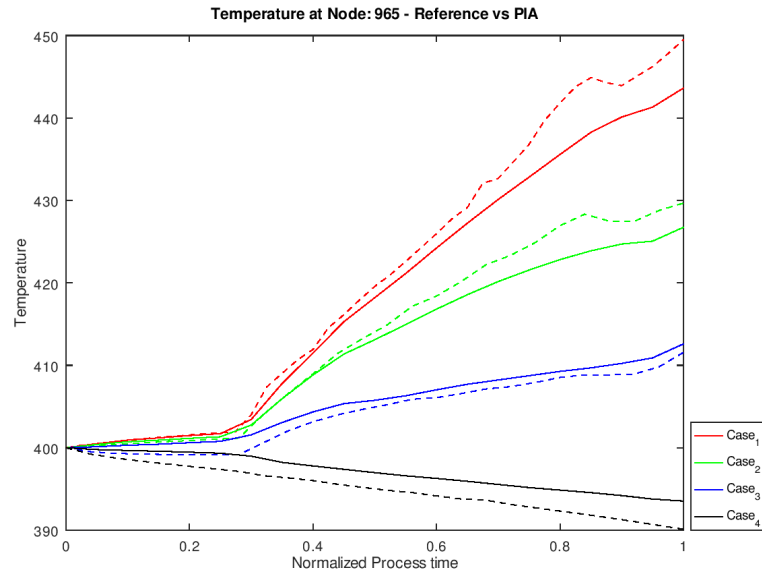


Figure 4.15: Evolution of field values at node 965 - Temperature

From Fig. (4.13) it is apparent that the equivalent plasticity values predicted by both the reference simulation and PIA are very similar except in the case when the process time is very small. This deviation could also be due to the effect of the explicit simulation employed for the reference results. The biggest differences between the results obtained from PIA and the reference simulations can be observed in the Von-Mises Stress values (Fig. (4.14)) and the Temperature values (Fig.(4.15)). These plots clearly demonstrate the effect of the large steps used in PIA. The conductive heat transfer has a higher effect than the convective heat transfer in the example that we have studied. Since PIA uses large step sizes, the elements on the surface are considered to be in contact for a larger time interval than when a smaller step-size is used. Hence this reflects as a lower temperature at the node. This effect is most prominently observed in the results obtained for case 4 where there is no volumetric heat source considered and there is only heat loss from the billet to the surrounding environment and the tools. Another consequence of the large step sizes is the larger effect of the inelastic heat fraction which has observed in the previous example of the axisymmetric screw as well. In the present example, this effect can be clearly observed in Case 1 and Case 2, while in Case 3

Case Name	Av. Error PEEQ	Av. Error Von-Mises Stress	Av. Error Temperature
Case 1	8.18%	2.63%	0.36%
Case 2	9.01%	2.45%	0.32%
Case 3	8.14%	3.49%	0.45%
Case 4	8.07%	5.02%	0.93%

Table 4.2: Accuracy of PIA v/s Reference results

the effect of the inelastic heat fraction is overshadowed by the effect of heat loss due to thermal conductance at the contact interfaces.

The accuracy of the PIA with respect to the different cases that has been studied can be seen in Table (4.2). It can be noted that the accuracy of prediction of the equivalent plasticity has a lower effect compared to the accuracy of the prediction of the temperature fields. Of particular significance is the fact that in the first three cases where the average error in the temperature fields is $\sim 0.4\%$, the average error in the computed stress is only around 2-3%. But, when the average error in the predicted temperature fields rises to $\sim 1\%$, the average error in the predicted Von-Mises stress values rises sharply to $\sim 5\%$. Thus it can be concluded from both the axisymmetric examples that have been considered that, even though PIA is able to predict the deformed shapes well, in the case of models where the effect of temperature on the material properties is high, proper care must be taken in terms of the step sizes to capture the thermal effect and the consequent effects in the stress.

PERFORMANCE

We have hypothesized that the efficiency and good performance of the PIA is due to the good prediction of the deformed shape after deformation by the combination of the geometric prediction with linear correction. This hypothesis can be validated by looking at the number of non-linear iterations that are required for convergence after the geometric prediction and linear correction step. Fig. (4.17) shows the number of non-linear iterations required at each step of PIA for Case 2, 3 and 4. It can be clearly inferred that the predicted shape (kinematically admissible shape) is very close to the actual deformed configuration as can be seen from Fig.

(4.16). This clearly illustrates the reason behind the efficiency and accuracy of the PIA. Also it can be noted that since most of the steps converges in just 2 non-linear iterations, there exists a potential to define a suitable adaptive time-stepping algorithm that can reduce the number of steps and improve the computational efficiency of PIA.

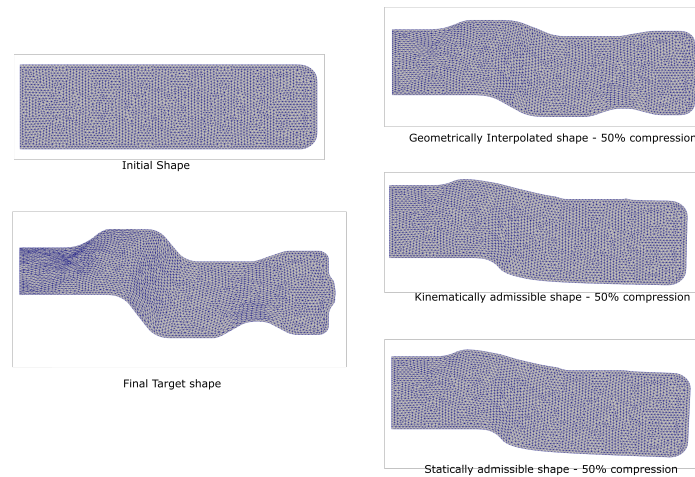


Figure 4.16: Shape prediction/correction in PIA

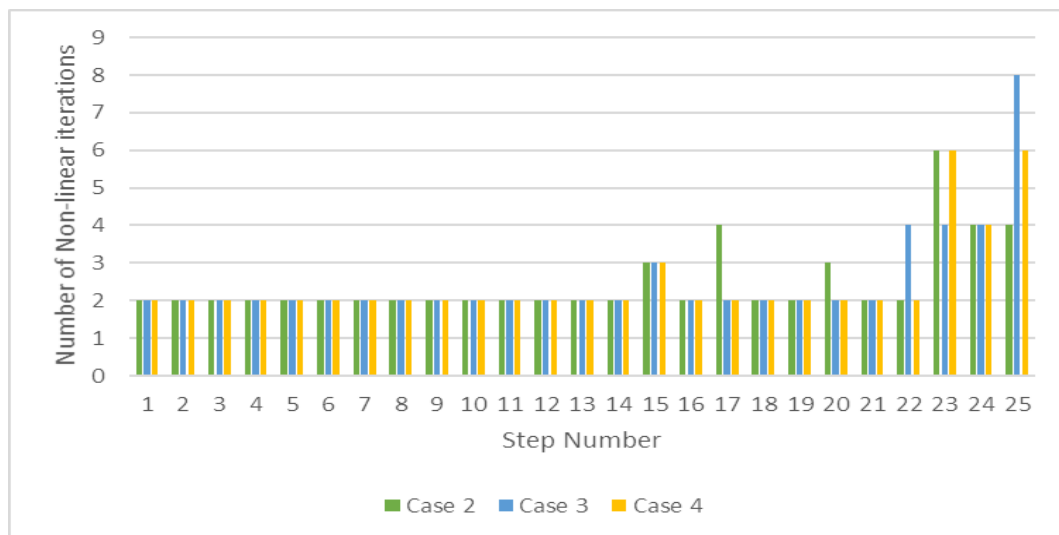


Figure 4.17: Number of Non-Linear Iterations at each step

4.2.3 3D UPSETTING

Since we have seen that the Pseudo Inverse Approach can give very good results in the case of 2D axisymmetric cases, it is interesting to also see whether the same technique can give good results in the case of 3D simulations as well. To test this, as a first case, we have studied the example of a 3D upsetting process. The upsetting process in this case consists of the flattening of a cylinder between two flat plates as shown in Fig. (4.18).

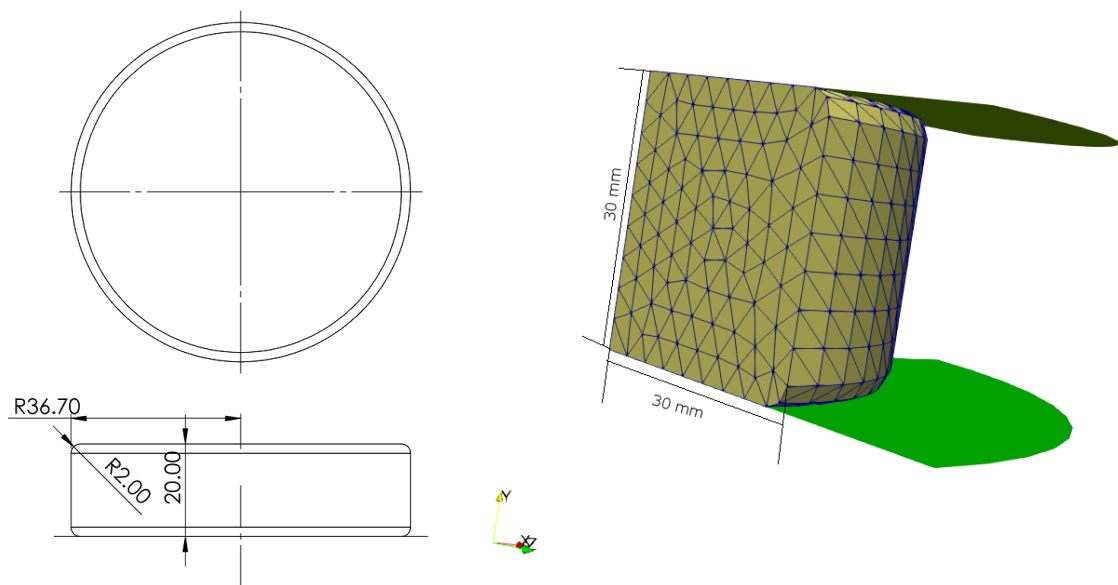


Figure 4.18: Representation of the upsetting process. a) Target shape b) Tools and Initial billet

The material is considered to be aluminium as used in the first example in Sec. (4.2.2). The tool is given a movement of 10mm in the negative Y- direction. For reducing the computational effort, a quarter-model is considered with both XY plane and the YZ plane becoming planes of symmetry and the temperature of the billet is assumed to be constant at 450°C (No heat exchange with the tools or the ambient environment). For keeping the simplicity of the approach, the model is discretized using 3232 linear tetrahedral elements (C3D4T). The results of the simulation can be seen in Fig. (4.19) and Fig. (4.20).

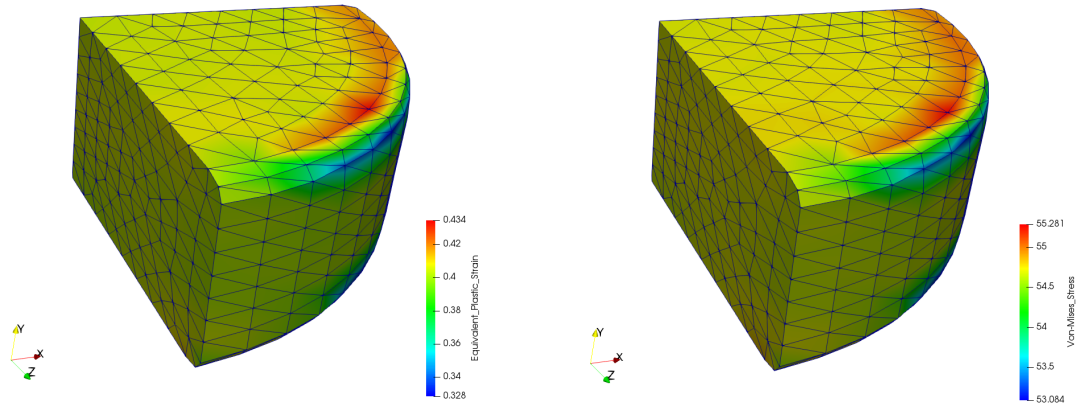


Figure 4.19: Upsetting simulation Reference Results - Quarter Model a) Equivalent Plastic Strain b) Von-Mises Stress

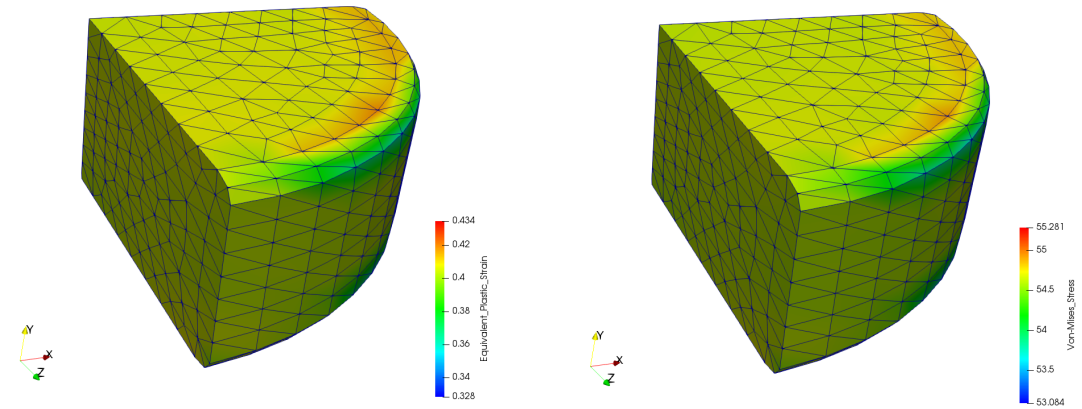


Figure 4.20: Upsetting simulation PIA Results - Quarter Model - 1 Step a) Equivalent Plastic Strain b) Von-Mises Stress

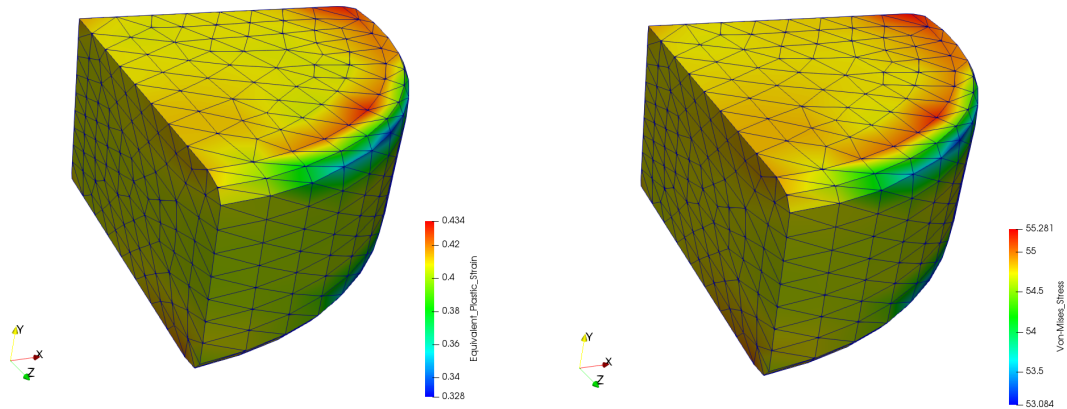


Figure 4.21: Upsetting simulation PIA Results - Quarter Model - 10 Step a) Equivalent Plastic Strain b) Von-Mises Stress

From the simulation results, we can see that the PIA gives a very good approximation of the upsetting simulation. One thing to note is that the PIA simulation is able to give a good approximation of the upsetting simulation in just one step due to the simplicity of the model being considered (a one-step Inverse Approach). But, as seen with previous 2D axisymmetric cold forging simulations, the predicted stresses and strains will not be accurate when considering more complex shapes and deformation paths. Upon plotting the evolution of the field variables at node no: 580, we are able to deduce that the ease of prediction in this case is due to the almost linear relation between the equivalent plastic strain over the process time. Fig. (4.22) highlights this relationship and the effects of varying the number of steps considered in PIA.

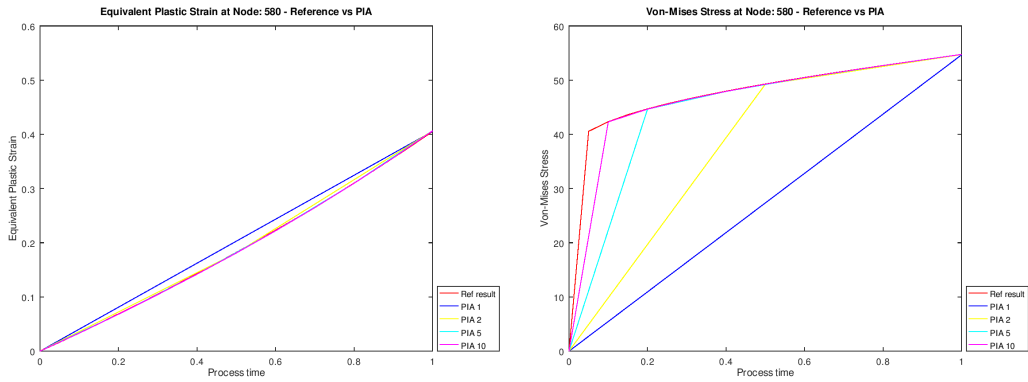


Figure 4.22: Evolution of field values at Node 580: Reference vs PIA - 3D Upsetting

We can see that all the simulations with more than 2 steps in PIA replicate the strain evolution quite well and thus aids in the accuracy of the results. The average error in the prediction of the Equivalent plastic strain between reference and results from PIA is $\sim 0.4\%$ (0.42% for 1 step and 0.49% for 10 step) while the average error in the predicted Von-Mises stress values is $\sim 0.1\%$ (0.14% for 1 step and 0.07% for 10 step). The biggest difference between the number of steps used in PIA is found in the error of the maximum and minimum field values predicted. In the single step PIA, the error in the maximum and minimum value of equivalent plastic strain is 3.59% and 9.6% , which drops to 0.9% and 1.34% respectively for the 10 step PIA. Thus initial results suggest that PIA could be a very good candidate for 3D simulations as well.

4.2.4 3D CUP

Even though excellent results were observed in the 3D Upsetting case described in Sec. (4.2.3), it is a very simple example and would need to be explored further to completely establish the suitability and efficacy of PIA in full 3D simulations. To this effect, we have considered a model of the 3D Cup forging. The deformed target shape and the tools and billet used are shown in Fig. (4.23).

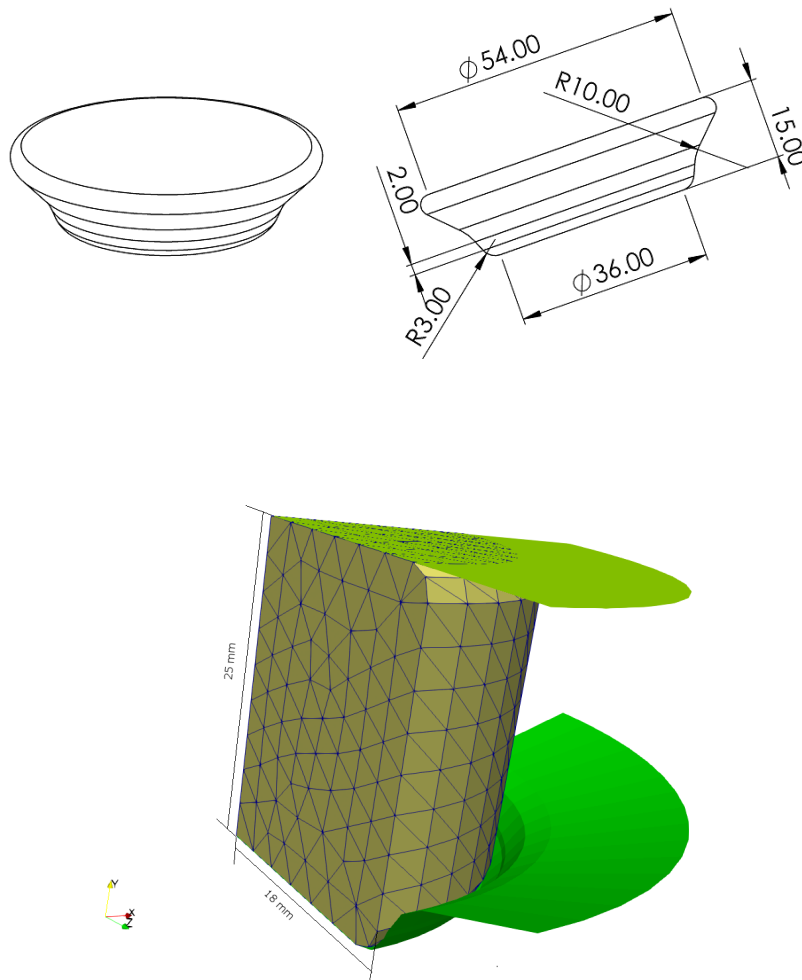


Figure 4.23: 3D Cup - a) Target shape b) Tools and Initial billet

The material is considered to be aluminium as used in the first example in Sec. (4.2.2). The tool is given a movement of 10mm in the negative Y- direction. For reducing the computational effort, a quarter-model is considered with both XY plane and the YZ plane becoming planes of symmetry and the temperature of the billet is assumed to be constant at 450°C. For keeping the simplicity of the approach, the model is discretized using 2762 linear tetrahedral elements (C3D4T). The results of the simulation can be seen in Fig. (4.24) and Fig. (4.25).

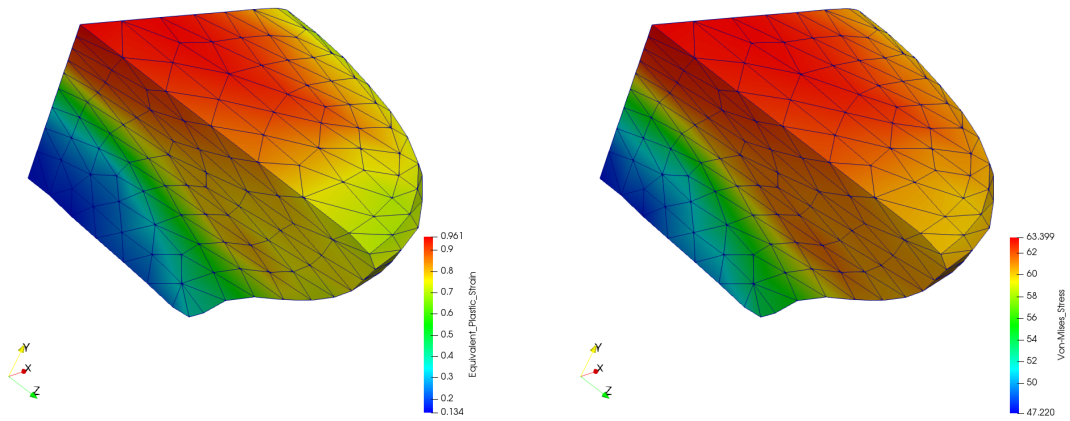


Figure 4.24: 3D Cup simulation Reference Results a) Equivalent Plastic Strain b) Von-Mises Stress

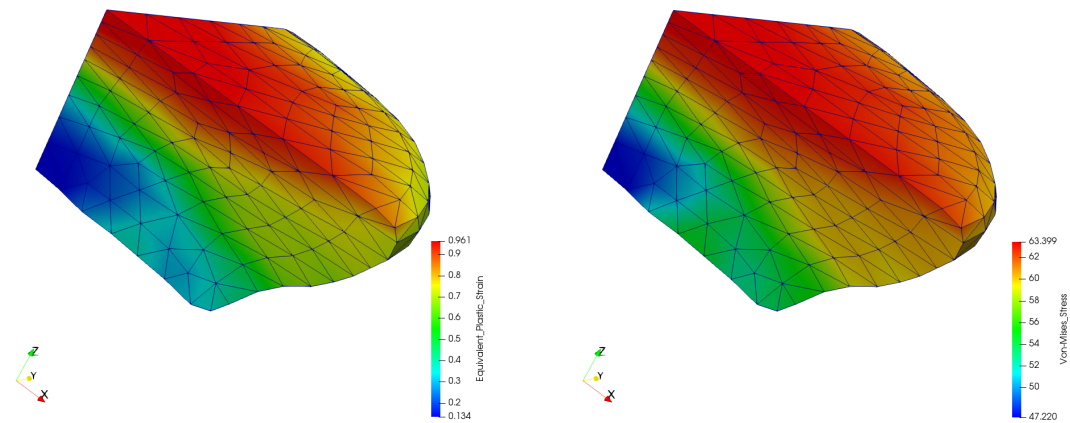


Figure 4.25: 3D Cup simulation PIA Results - 20 steps a) Equivalent Plastic Strain b) Von-Mises Stress

The evolution of the stresses and strains is demonstrated in Fig. (4.26) by following the evolution of the stresses and strains at node 580.

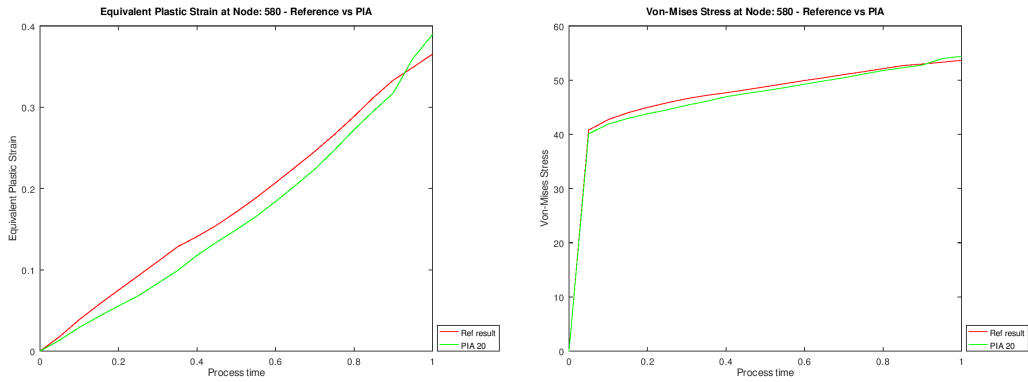


Figure 4.26: Evolution of field values at Node 580: Reference vs PIA - 3D Cup

It can be seen that the results obtained from PIA and the reference simulations show a large concurrence. On comparing the reference results and PIA results, we notice that the average error in the equivalent plasticity values is 5.88% and that in the Von-Mises Stress values is 0.88%. We also observe that the maximum and minimum values of the equivalent plasticity values predicted by PIA and the reference results shows a much higher error (~30%). One of the possible causes could be the very coarse discretization that has been used and the mass-scaling that has been used for keeping the reference simulation times low. Further investigations will be required to look into this matter further, but due to time limitations, the same has not been attempted in the present work.

4.3 COMPUTATION TIME

From the examples in 2D axisymmetric and general 3D cases presented in Sec. (4.2), we have seen that the PIA can give pretty accurate results in comparison with the conventional incremental methods. The second question that needs to be addressed is how PIA compares with the conventional methods in terms of computation time.

The PIA code that has been developed during the course of this work is predominantly an academic effort and hence it is not optimized version that can be directly used to compare with commercially available software that has been completely optimized. Moreover,

the reference results used in this work are obtained from ABAQUS[®]/ Explicit which uses an explicit formulation compared to an implicit formulation used in PIA. Nevertheless, the computation times of both the methods for the different cases that we have studied in the previous section is compared in Table (4.3) and Fig. (4.27). The computation time corresponds to the single-core performance using an Intel[®] Core[™]2 Quad CPU Q9300 @ 2.5 GHz with 8 GB system memory and full double precision. Usually in an explicit simulation, the stable step-size increments is calculated based on the element sizes and hence can cause very high computation times in cases where the process time is high. Mass-scaling is a common technique used in practice to keep computation times low and is used in the reference simulations to keep computation times low. A semi-automatic mass scaling is used in our case so that the target time increment in each step is 1e-06. Computation times for certain case without using mass scaling maybe seen in Table (4.4).

Case	No. of steps - Ref. Results	Time (seconds) - Ref Results	No. of steps - PIA	Time (seconds) - PIA	Computational Advantage with PIA
2D_Screw - Case 1	831043	1936.3	20	284.73	6.8 x
2D_Screw - Case 2	831043	1909.1	25	292.28	6.5 x
2D_Wheel - Case 1	107326	1025.6	40	1665.98	0.61 x
2D_Wheel - Case 2	1011635	9042.9	25	1113.38	8.12 x
2D_Wheel - Case 3	7939367	62970.3	25	1301.98	48.3 x
2D_Wheel - Case 4	7938144	62995.6	25	1297.58	48.5 x
3D_Upsetting	799257	6710.8	10	410.25	16.35 x
3D_Cup	872438	6420.7	20	905.32	7.09 x

Table 4.3: Computation Time - With mass scaling

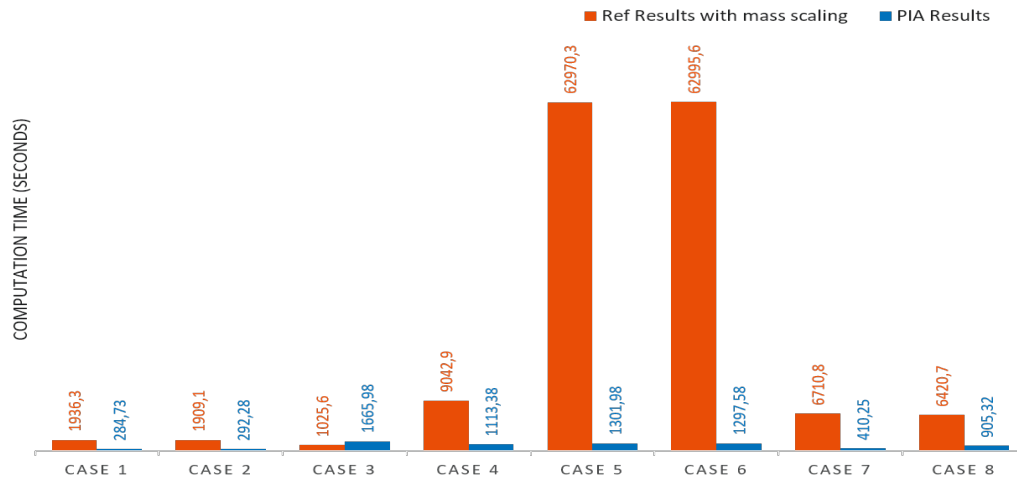


Figure 4.27: Computation Time - With Mass Scaling

Case	No. of steps - Ref. Results	Time (mins) - Ref Results	No. of steps - PIA	Time (mins) - PIA	Computational Advantage with PIA
2D_Screw - Case 2	52975195	2000.5	25	4.87	410 x
2D_Wheel - Case 1	107326	152.48	40	27.77	5.5 x
2D_Wheel - Case 2	12013335	1804.7	25	18.56	97 x
3D_Upsetting	6132010	767.42	10	6.84	112.24 x

Table 4.4: Computation Time - Without mass scaling

From the results it is clear that PIA gives a clear advantage over classical incremental methods, but for the proper quantification and comparison of the computational time advantage of using PIA, a comparison should be made with a commercially available software based on the implicit analysis like FORGE[®]NxT. Due to lack of resources, the same has not been attempted in this work.

Have I done the world good, or have I added a menace?

Guglielmo Marconi

5

Conclusions and Future perspectives

5.1 CONCLUSIONS

We have seen that the simulation of the bulk metal forging process is influenced by the effects of viscoplasticity, dependence of mechanical characteristics on temperature and contact conditions between the tool and workpiece. Numerical simulations, by existing methods, of these kind of complex relations is challenging, especially in terms of computational time.

Simulation approaches found in the engineering literature of bulk metal forming fall within two principal strategies, the direct or forward solution scheme that consists of resolving simultaneously mechanical and thermal balance equation starting from an initial shape, and backward deformation techniques, in which the the mechanical system is solved by starting from the final deformed configuration considering an inverse loading path.

The main objective of this work was the validation, analysis and improvement of the Pseudo

Inverse Approach proposed in the case of 2D axisymmetric cold forging to hot-forging simulations in both 2D and 3D via the solution of a coupled thermo-mechanical problem. It is to be noted that the presented formulation does not include frictional effects due to contact between tool and work piece surfaces, but transient thermal effects are taken into account. An iso-thermal split is utilized for the coupled thermo-mechanical problem and it is found to give results that are accurate enough.

To show the validation of the formulation and compare the efficiency with respect to the classical forward approaches, various applications of the formulation has been exposed in details, such as thermo-viscoplastic problem from 2D axisymmetric cases and simple, generalized 3D problems in bulk metal forging. The effects of heat capacity, intrinsic dissipation and the heat exchange with the environment are included in the model. The results show us that the Pseudo Inverse Approach is robust enough to handle the thermo-viscoplastic effects, but the developed code needs to be improved upon to fully investigate the performance of the method in general 3D case with thermal effects included.

Although, we have good results from the PIA, it should be noted that the results are heavily dependent on the meshes that are being used. In all the cases that we have studied in this work, we have used the meshes obtained from the reference simulations as the input for the PIA. This will not be a strategy that can be used in a practical context. Mesh-morphing procedures, especially in 3D, will have to be defined in this context. In particular, a common problem associated with meshes generated through a mesh-morphing procedure is one of that of element reversals and measures need to be taken to ensure that a robust and good enough mesh is used for the simulation. If not, it can lead to premature termination of the analysis and/or inaccuracies may creep into the results. Strategies to overcome this issue needs to be included to fully realize the potential of PIA.

Since the software developed for the PIA is predominantly an academic work, and the reference simulation is made using an explicit analysis while the PIA relies on an implicit analysis, we have not attempted here to give an exhaustive comparison of the solution times

taken by the classical approaches and PIA. Although, the time comparisons indicate that PIA is much more efficient in terms of computational time than classical approaches even while accounting for the time spent in the geometric interpolation/linear correction step. In all the models studied, the geometric interpolation/ linear correction phase uses about 15-25% of the total solution time. Considering that an implicit analysis using classical methods uses hundreds of steps while in PIA we can obtain comparable results using ~10-20 steps, PIA should be able to give a computational advantage of 5x-10x over classical implicit incremental approaches.

5.2 FUTURE PERSPECTIVES

5.2.1 OPTIMIZATION AND IMPROVEMENT OF THE CODE

The most immediate aspect that would need to be done is the optimization of the code so as to be able to perform a comparison of the solution times with that of commercially available software using implicit incremental methods. This bench-marking would ascertain the computational advantage that we could possibly gain from employing the PIA. Another important detail that we have seen during our experiments is the need for proper element formulations for the 3D simulation. Simple linear tetrahedral formulations are not optimal for the finite deformation 3D simulation of the forging process which models nearly in-compressible behaviour. Formulations presented in [Taylor, 2000, Lo & Ling, 2000, Castellazzi et al., 2015] and others will have to be explored to find out a suitable formulation that can be used for finite deformation problems with large-step size such as the ones that we use in PIA.

A second improvement that would be needed to fully realize the advantages that we can glean from PIA would be the introduction of an automatic/adaptive step-size control method. Adaptive time-stepping strategies for quasi-static problems have been discussed in [van den Boogaard et al., 1994], but is based on the arc-length method and is suitable for the displacement and load control. In our case, we have seen that the stress field predictions are heavily dependent on the proper prediction of the temperature fields and the step-size control is pri-

marily required for ensuring that the thermal computations have accurate inputs. So a new strategy for step-size control would have to be formulated to efficiently utilize the advantages proposed by PIA while being able to capture the physical effects accurately.

The first source of inaccuracy in prediction of the temperature field arises from the approximation of the contact surfaces and the subsequent thermal conduction and convection effects. One possible solution to the problem would be to multiply the coefficient of heat conduction between the tools and billet by a factor f_c that can help to linearize the contact evolution over the time step. The factor would be unity for the surfaces that were in contact with the tools in the previous step, but for the surfaces that were previously not in contact with the tools but come in to contact with the tools in the present time step, it would lie in between 0 and 1. This kind of a strategy might be able to circumvent the inaccuracies due to conductive and convective effects without affecting the step sizes or the number of steps.

The second source of inaccuracy in the prediction of the temperature field arises from the prediction of the mechanical work that gets converted into heat energy. The magnitude of this effect is based on the magnitude of the strain rate and hence, an adaptive time-stepping strategy that determines step-sizes based on a maximum allowed strain rate value would be able to effectively capture the effects of the heat generated due to mechanical work.

5.2.2 PROCESS AND PREFORM OPTIMIZATION

The first and the foremost application of PIA would be in the development of the optimal preform shapes and process parameters to produce the required deformed shape in the work-piece. Taking into account the requirement of the complex shapes for the finished product from the industry and the focus on near net-shape manufacturing to reduce costs and increase competitiveness, it is imperative that process designers have a tool that can help in designing optimal preforms and processes. The PIA promises a good improvement in the computational efficiency while retaining a good accuracy and can be a good substitute for the existing approaches. A first approach to using PIA in optimization of preform shapes was made by

[Halouani et al., 2012a, HALOUANI et al., 2012] in the case of 2D axisymmetric cold forging. In this, the optimization problem was posed as a multi-objective optimization problem that involves the minimization of the effective plastic strain in the final deformed part and the maximum forging force during the forging operations. The preform shapes can be defined by using tools defined by B-Splines. The optimization employed the NSGA-II (Elitist Non-dominated Sorting Genetic Algorithm) algorithm along with a Kriging method and was able to find the optimal set of control points to define the B-Spline shape that could produce the required deformed shape with the lowest plastic strain and forging forces.

A similar set of simulations were done for the 2D axisymmetric viscoplastic case with very positive results and were presented in international conferences [NUMIFORM 2016]. One of the next steps would be the simulation and optimization of preforms in the general 3D case. It could follow the same optimization routines based on genetic algorithms and meta-model assisted methods such as [Ejday & Fourment, 2010, Fourment & Chenot, 1996, Fourment et al., 1996], sensitivity based methods as described in [Badrinarayanan & Zabarar, 1996, Steinmann & Landkammer, 2014, Ciancio et al., 2015] or even neural-network based optimization as described in [D'Addona & Antonelli, 2018]. Due to the formulation of PIA, it provides an almost plug-and-play compatibility with existing optimization schemes. Another important thing to note with respect to the use of PIA in optimization studies is that, due to the use of the initial inverse computation between the final deformed shape and the generated initial shape, bad design iterations are eliminated quickly in the initial step due to non-convergence/slow convergence of the Newton-Raphson iterations.

5.2.3 MESH OPTIMIZATION

One particular problem that plagues the metal forming simulations is the definition of a suitable mesh for doing the FE simulations. Since the forward deformation method meshes the initial part geometry without taking into account the final desired part geometry, it is difficult to create a suitable mesh in the initial part geometry at the onset. A popular workaround

for this problem is the use of adaptive re-meshing techniques and/or the use of an ALE formulation. Though useful in terms of maintaining the accuracy of the simulation, re-meshing involves high computational overhead and can lead to higher computational time. In the case of PIA, it is the final deformed geometry that is meshed and is transferred to the initial generated shape using a PDE based mesh-morphing technique and a single-step inverse approach. This gives a better initial mesh, but is still plagued by instances of inverted elements that can lead to premature termination of the simulation. One of the possible remedies in this case has been the use of mesh smoothing as used in FEMWARP [Baker, 2002, Shontz & Vavasis, 2010]. FEMWARP uses the finite element method for mesh-morphing from a given mesh to a target shape and makes use of an optimization based untangler for making the method robust against element reversals. A comparison of different available mesh-morphing techniques has been made in [Staten et al., 2012] and multiple techniques have been proposed to preserve the quality of the mesh during the mesh-morphing operation. These techniques could help in creating good quality meshes on the initial part and avoid subsequent re-meshing during the metal forming simulation.

Another important advancement in the area of meshing for forming analysis has been proposed by [Dheeravongkit & Shimada, 2005b,a, 2007]. The proposed method uses an inverse pre-deformation method to “pre-deform” the input mesh to reduce the number of inverted and ill-shaped elements at the later stage of the analysis. The term “inverse pre-deformation” is used to illustrate the idea of this method in which, each mesh element which will be deformed during analysis is first predicted and then the new input mesh which contains elements that have approximately opposite shapes of those predicted will be created. Because overall element shape quality tends to improve along the analysis process, with this approach, the number of inverted and ill-shaped elements in the later analysis stage can be reduced. An overview of the proposed algorithm can be found in Fig 5.1. A modified version of this approach maybe employed to improve the mesh in the Pseudo Inverse Approach.

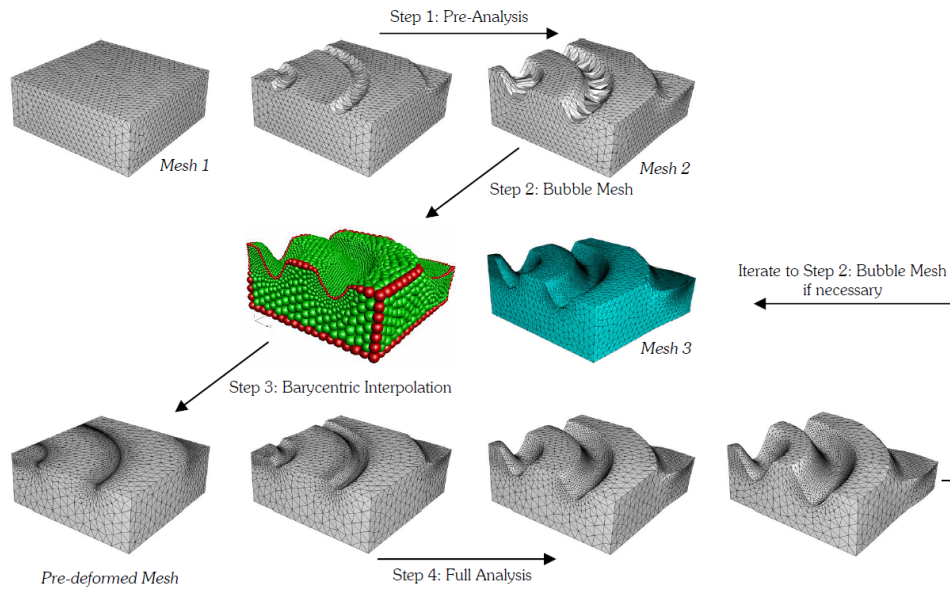


Figure 5.1: Overview of the inverse pre-deformation method[Dheeravongkit & Shimada, 2005b]

It would be interesting to see how either/both of these strategies will improve the mesh generation of the initial shape used in PIA and also how the results are affected. In the case of the inverse pre-deformation method, using PIA we would be able to eliminate the pre-analysis step altogether by defining the bubble mesh on a regular mesh of the final desired shape and then continue with the barycentric interpolation and iterative refinement of the mesh as shown in Fig 5.1. The use of PIA in step 4 for the full analysis could also reduce the total computation time to obtain a good quality mesh.

5.2.4 OTHER APPLICATIONS

In this present study, the PIA has been developed and applications have been discussed only with respect to the metal forming analysis. But, PIA is an approach that can be suitably applied to all other inverse reconstruction problems that attempt to determine a source, given a field and knowing the physical properties, satisfying a given model [Neto & da Silva Neto, 2013]. Examples of such problems include bio-mechanics simulations like the structural remodeling in the dyssynchronous failing heart [Helm et al., 2006], soft tissue bio-mechanics

and mechanobiology, etc where the effects of the deformation can be measured using electronic scans and the corresponding undeformed shape needs to be computed.

Another use case for the PIA would be in inverse parameter identification simulations where the accuracy and enhancements in the computational efficiency would put it in a very advantageous position for optimization simulations. This could lead to faster parameter identification and optimization.

6

Résumé étendu

Le forgeage des métaux est un procédé de déformation dans lequel la pièce est comprimée entre deux matrices, en utilisant soit un impact, soit une pression progressive pour réaliser la forme souhaitée. Le forgeage peut être considéré comme l'une des plus anciennes opérations de traitement des métaux et, d'après les plus anciens documents écrits de l'humanité, elle pourrait remonter à environ 5000 ans av. J.-C. [Groover, 2010]. Aujourd'hui, le forgeage est un procédé industriel important utilisé pour fabriquer divers composants de haute résistance présentant un meilleur rapport résistance / poids que ceux obtenus par d'autres opérations de fabrication telles que le moulage ou le soudage / fabrication. Le secteur automobile ainsi que les fournisseurs de systèmes de rang 1 représentent plus de 80% de la production totale de pièces forgées. En outre, de nombreuses industries utilisent la forge pour réaliser la forme de base de gros composants qui sont ensuite usinés pour obtenir la forme et les dimensions finales.

Comme la ductilité des métaux est étroitement liée à la température, le forgeage à des tem-

pératures élevées est effectué pour obtenir des pièces de formes compliquées. Les opérations de forgeage peuvent être classées comme forgeage à froid, forgeage à mi-chaud et forgeage à chaud. Bien que le forgeage ait été l'un des plus anciens procédés de traitement des métaux à être découvert, le procédé reste fortement tributaire du savoir-faire et des compétences de l'opérateur / du concepteur de processus en raison de divers facteurs. C'est un procédé complexe et les phénomènes physiques décrivant une opération de forgeage sont difficiles à exprimer par des relations quantitatives en raison de l'évolution des surfaces de contact et des relations matérielles et géométriques non linéaires. Une prévision des variables associées au procédés, telles que la température et les contraintes d'écoulement, doit être effectuée pour la conception du procédé de forgeage et la séquence des opérations. Les simulations numériques jouent un rôle important pour l'optimisation de ce procédé.

SIMULATION NUMÉRIQUE DU PROCÉDÉ DE FORGEAGE

Le développement de la méthode des éléments finis et la disponibilité d'une puissance de calcul bon marché ont contribué à la démocratisation de la simulation. Cheng & Kikuchi [Cheng & Kikuchi, 1985], Mackerle [Mackerle, 2006] et Hartley & Pillinger [Hartley & Pillinger, 2006] ont présenté une revue complète de la littérature associée à l'analyse de procédés de formage des métaux à l'aide de formulations élasto-plastiques en grandes déformations, comprenant le contact unilatéral et le frottement.

MÉCANIQUE DES MILIEUX CONTINUS

Étant donné que le forgeage implique la mise en forme d'une pièce à l'aide d'une déformation plastique, une analyse en plasticité est nécessaire pour permettre une prédiction satisfaisante des caractéristiques du procédé. Une description générale de la déformation du métal peut être donnée par la mécanique des milieux continus si nous ignorons les effets microscopiques et les vides dans la pièce. Le procédé de forgeage le plus simple peut être expliqué à l'aide de la Fig. (2.2), où nous considérons la déformation d'un corps entre une paire de matrices. En

négligeant les forces d'inertie, l'équilibre quasi-statique du domaine à tout moment t peut être exprimé par,

$$\begin{aligned}
\operatorname{div} \boldsymbol{\sigma} + \rho \mathbf{b} &= 0 \quad \text{in } \Omega \\
(\mathbf{u} - \mathbf{u}_g) \cdot \mathbf{n} &= 0 \quad \text{on } \partial_d \Omega \\
\boldsymbol{\sigma} \mathbf{n} &= \mathbf{t} = 0 \quad \text{on } \partial_f \Omega
\end{aligned} \tag{6.1}$$

où $\boldsymbol{\sigma}$ est le tenseur de contrainte de Cauchy défini dans la configuration déformée Ω , \mathbf{b} est le vecteur de forces volumiques, \mathbf{u} est le vecteur de déplacement, \mathbf{u}_g est le déplacement de l'outil donné sur la frontière $\partial_d \Omega$ et \mathbf{t} est le vecteur de traction prescrit sur la surface $\partial_f \Omega$ avec \mathbf{n} étant le vecteur normal unitaire vers l'extérieur de la surface. En utilisant le principe du travail virtuel et le théorème de divergence de Green et en incorporant la contrainte d'incompressibilité à l'aide de la formulation du pénalité, la forme faible de l'eq. (6.1) peut être exprimé par,

$$\int_{\Omega} \boldsymbol{\sigma} : \boldsymbol{\varepsilon}^* d\Omega + \int_{\Omega} K \varepsilon_v \varepsilon_v^* d\Omega - \int_{\Omega} \rho \mathbf{b} \cdot \mathbf{u}^* d\Omega = 0 \tag{6.2}$$

où ε_v est la déformation volumétrique donnée comme trace du tenseur de déformation et ε_v^* est la déformation volumétrique virtuelle et K est un grand nombre positif garantissant la satisfaction de la contrainte d'incompressibilité [Zienkiewicz, 1974].

Dans le cas d'une analyse non linéaire, nous cherchons à trouver l'état d'équilibre d'un corps correspondant aux charges appliquées à la configuration à un instant spécifié t . Pour une analyse non linéaire matérielle et géométrique, qui inclut des phénomènes liés au trajet ou au temps, il convient de résoudre les relations d'équilibre sur la période de temps complète considérée en supposant que la solution au temps t est connue et la solution au temps $t + \Delta t$. Δt est un incrément de temps choisi de manière appropriée. L'état d'équilibre du corps au temps $t + \Delta t$ peut être exprimé par,

$$\int_{\Omega^{t+\Delta t}} \boldsymbol{\sigma}^{t+\Delta t} : \boldsymbol{\varepsilon}^* d\Omega + \int_{\Omega^{t+\Delta t}} K (\varepsilon_v^{t+\Delta t}) \varepsilon_v^* d\Omega - \int_{\Omega^{t+\Delta t}} \rho^{t+\Delta t} \mathbf{b}^{t+\Delta t} \cdot \mathbf{u}^* d\Omega = 0 \quad (6.3)$$

THERMODYNAMIQUE

Le problème de transfert de chaleur associé au procédé de forgeage du métal peut être exprimé mathématiquement par,

$$\begin{aligned} \rho c \dot{T} - \operatorname{div}(k \nabla T) &= r \quad \text{in } \Omega \\ -k \nabla T &= h_{wd} (T - T_d) \quad \text{on } \partial_d \Omega \\ -k \nabla T &= h_{wa} (T - T_a) + \epsilon \sigma (T^4 - T_a^4) \quad \text{on } \partial_f \Omega \end{aligned} \quad (6.4)$$

où ρ est la masse volumique, c est la capacité thermique spécifique, k est la conductivité thermique, r est la source de chaleur volumétrique, T est le champ de température inconnu, h_{wd} est le coefficient de transfert de chaleur à l'interface entre la pièce et la matrice, T_d est la température de la matrice, h_{wa} est le coefficient de transfert de chaleur à l'interface entre la pièce et l'environnement ambiant, T_a est la température de l'environnement ambiant, ϵ est l'émissivité, σ est la constante de Stefan-Boltzmann et \mathbf{n} est la normale unitaire extérieure à la surface. Considérant qu'il n'y a pas d'autre terme de force volumique que la dissipation mécanique, et que la dissipation mécanique est équivalente à la chaleur dégagée par le travail plastique, la forme faible de l'équation. (6.4) peut être exprimée ainsi:

$$\int_{\Omega} k \nabla T \nabla T^* d\Omega + \int_{\Omega} \rho c \dot{T} T^* d\Omega - \int_{\Omega} \kappa \boldsymbol{\sigma} : \dot{\boldsymbol{\varepsilon}} T^* d\Omega - \int_{\partial \Omega} k \nabla T T^* d\Gamma = 0 \quad (6.5)$$

où κ représente la fraction de la dissipation mécanique convertie en chaleur (coefficient de

Taylor-Quinney [Taylor & Quinney, 1934, Rittel et al., 2017]), σ est le tenseur de contraintes de Cauchy et $\dot{\epsilon}$ est le taux de déformaion.

ANALYSE NUMÉRIQUE

Une difficulté fondamentale dans l'application directe de l'équation (6.3) est que la configuration déformée du corps est une inconnue qui doit être évaluée et qui n'est pas connue a priori. Comme la configuration à l'instant $t + \Delta t$ n'est pas connue, toutes les forces, contraintes et déformations seront référencées dans une configuration connue. Ce changement de configuration peut être traité de manière élégante en utilisant le tenseur de gradient de transformation et les mesures de déformation conduisant à la classe d'analyses connues sous le nom de formulations *Lagrangienne Totale* et *Lagrangienne Actualisée*. Bien que robustes, les analyses numériques basées sur ces formulations prennent beaucoup de temps. Bien qu'aucune hypothèse de déformation ne soit faite dans la formulation, du fait des hypothèses utilisées dans la linéarisation de différentes variables et la linéarisation de l'évolution des contacts, les étapes utilisées dans une approche incrémentale restent relativement petites et augmentent l'effort de calcul requis.

Comme le processus de conception dans le forgeage vise à trouver la géométrie de référence optimale, le problème peut être posé comme un problème de recherche de forme inverse, comme dans la *Méthode de Traçage Arrière*. Le principal inconvénient de la méthode de cette méthode provient de la mauvaise formulation du problème et de la formulation récursive nécessaire à la prédiction des variables plastiques. Etant donné que l'étape d'avance repose sur la formulation classique de déformation incrémentale, le procédé de traçage arrière finit par être extrêmement fastidieux pour prévoir la forme initiale de la forme déformée souhaitée.

L'APPROCHE PSEUDO-INVERSE

Bien que les schémas de traçage en amont semblent prometteurs pour trouver une forme initiale optimale, ils sont pénalisés par les exigences de calcul considérables des étapes de la

formulation récursive nécessaire pour calculer la déformation plastique. Ainsi, les méthodes inverses ne peuvent devenir pratiques que si une technique est conçue pour calculer la déformation directe de manière robuste et avec une précision suffisante à des coûts de calcul réduits. L'approche pseudo-inverse est une extension de l'approche inverse en une étape qui a été appliquée pour la première fois dans le formage de tôle [# Guo1990, # Guo2004]. Elle repose sur trois postulats principaux énumérés ci-dessous:

1. Les équations qui régissent la simulation du formage des métaux sont par nature non linéaires et la résolution de ces équations non linéaires peut être efficacement réalisée à l'aide d'une méthode de Newton-Raphson. La convergence vers une solution via la méthode Newton-Raphson est fortement influencée par la solution initiale fournie. Si une hypothèse initiale proche de la solution finale peut être fournie, la convergence vers une solution est possible, même pour de très grands pas.
2. Les procédés de formage des métaux étant relativement rapides, la perte de chaleur dans l'environnement par convection ou par rayonnement et par la conduction dans les outils peut être raisonnablement bien estimée, même pour de grands pas de temps..
3. Chargement monotone: Il n'y a pas de décharge plastique et, bien que l'exigence puisse sembler stricte, la plupart des opérations de formage en masse entrent dans cette catégorie.

Dans le cas du forgeage, la forme déformée finale est connue a priori. Si la forme initiale est également connue (ou si une approximation rapide de la forme initiale peut être rapidement réalisée), il serait alors possible de prédire les déformées aux différents pas de temps en utilisant efficacement les informations géométriques des configurations déformée et non déformée si un chemin de chargement monotone est considéré. Si la forme déformée (ou une approximation suffisamment proche) est connue, il serait alors possible de vérifier si cette configuration satisfait rapidement les conditions d'équilibre et de contact et de rechercher les variables plastiques. Les étapes de l'approche pseudo-inverse peuvent être résumées comme suit:

1. Une approche inverse en une étape pour générer ou vérifier l'adéquation de la forme initiale supposée pour l'analyse directe et pour transférer le maillage de la pièce finale à la pièce initiale
2. L'ensemble du processus de déformation est divisé en plusieurs étapes en fonction de la nécessité de recréer le chemin de déformation et de créer des formes intermédiaires par interpolation géométrique.
3. Ces formes intermédiaires interpolées géométriquement sont ensuite corrigées à l'aide d'une méthode à surface libre afin d'obtenir des formes intermédiaires cinématiquement admissibles.
4. Une analyse thermo-mécanique avancée à déformation finie et à déplacement finis est effectuée à chaque étape pour vérifier la configuration à l'équilibre et la configuration déformée réelle. Les contraintes sont obtenues à l'aide d'un algorithme de Newton-Raphson et d'incrément de déformation logarithmiques
5. Le processus est répété jusqu'à ce que toute la déformation ait été prise en compte.

FORMULATION MATHÉMATIQUE

En utilisant une discrétisation par éléments finis, le champ de déplacement à l'intérieur d'un élément peut être interpolé à partir de la position des noeuds de l'élément de la manière suivante:

$$\mathbf{x} = \sum_{i=1}^n N_i \mathbf{x}_i \quad (6.6)$$

où \mathbf{x}_i sont la position des noeuds de l'élément, N_i sont les fonctions de forme de l'élément et n est le nombre de noeuds dans l'élément.

En utilisant une discrétisation similaire, les champs de déplacement et de température dans un élément peuvent être interpolés comme suit:

$$\mathbf{u} = \sum_{i=1}^n N_i \mathbf{u}_i; \quad T = \sum_{i=1}^n N_i T_i$$

En utilisant cette interpolation, Eqs. (6.2, 6.5) peuvent être exprimées sous la forme assemblée telle que,

$$\begin{aligned} \sum_{e=1}^{nel} \mathbf{u}_i^* \cdot \left(\int_{\Omega^e} \mathbf{B}_m^T \boldsymbol{\sigma} d\Omega + \int_{\Omega^e} K \varepsilon_v \mathbf{B}_v d\Omega - \int_{\Omega^e} \rho N_i^T \mathbf{b} d\Omega \right) &= 0 \\ \sum_{e=1}^{nel} T_i^* \left(\int_{\Omega^e} k \mathbf{B}_t \mathbf{B}_t^T T_i d\Omega + \int_{\Omega^e} \rho c N_i N_i^T T_i d\Omega - \int_{\Omega^e} r N_i d\Omega + \int_{\partial\Omega^e} q_i N_i d\Gamma \right) &= 0 \end{aligned} \quad (6.7)$$

$$\text{où } \boldsymbol{\varepsilon}^* = \mathbf{B}_m \mathbf{u}_i^*, \mathbf{B}_v = \mathbf{B}_m \mathbf{I}, \mathbf{B}_t = \nabla N_i \text{ et } q = -k \nabla T.$$

SCHEMA POUR LA RÉACTUALISATION DES CONTRAINTES

Dans le cas de problèmes de déformation finie, il est important de disposer d'un schéma cohérent pour la réactualisation des contraintes qui respecte les restrictions sur les configurations dans lesquelles les différentes mesures de contrainte et de déformation sont définies. Dans notre cas, les équations mathématiques sont complètement définies sur la configuration déformée et nous devons donc calculer les contraintes de Cauchy ($\boldsymbol{\sigma}$) dans la configuration déformée. En utilisant la définition du tenseur de gradient de déformation et les développements donnés dans la Sec. (3.1.4), les contraintes de Cauchy ($\boldsymbol{\sigma}$) dans la configuration déformée peuvent être définies ainsi:

$$\boldsymbol{\sigma}_{t+\Delta t}^t = \frac{1}{J} \mathbf{F} \boldsymbol{\sigma}^t \mathbf{F}^T \quad (6.8)$$

RÉACTUALISATION DES CONTRAINTES THERMO-VISCOPLASTIQUES

Le comportement du matériau en fonction de la vitesse est particulièrement important dans une analyse de formage à chaud et nécessite l'utilisation d'un modèle de comportement thermo-viscoplastique pour capturer avec précision le comportement du matériau. En utilisant les tenseurs de déformation logarithmiques, nous pouvons avoir une décomposition additive des équations semblables aux équations de Prandtl-Reuss dans le cas de la plasticité comme,

$$\Delta \boldsymbol{\varepsilon} = \Delta \boldsymbol{\varepsilon}_e + \Delta \boldsymbol{\varepsilon}_{vp} + \Delta \boldsymbol{\varepsilon}_{th} \quad (6.9)$$

L'incrément de contrainte dans ce cas peut être trouvé en utilisant la relation,

$$\Delta \boldsymbol{\sigma} = \mathbf{H}^e \Delta \boldsymbol{\varepsilon}_e = \mathbf{H}^e (\Delta \boldsymbol{\varepsilon} - \Delta \boldsymbol{\varepsilon}_{vp} - \Delta \boldsymbol{\varepsilon}_{th}) \quad (6.10)$$

En utilisant un modèle de cohérence [Wang et al., 1997], le critère de plasticité pour un matériau dépendant de la vitesse tenant compte de la loi de comportement isotrope et critère du plasticité de Von-Mises peut être écrit ainsi:

$$f(\boldsymbol{\sigma}, \bar{\boldsymbol{\varepsilon}}_{vp}, \dot{\bar{\boldsymbol{\varepsilon}}}_{vp}, T) = \bar{\sigma} - \sigma_Y(\bar{\boldsymbol{\varepsilon}}_{vp}, \dot{\bar{\boldsymbol{\varepsilon}}}_{vp}, T) = 0 \quad (6.11)$$

où $\bar{\sigma}$ est la contrainte équivalente donnée par $\bar{\sigma} = (\boldsymbol{\sigma}^T \mathbf{P} \boldsymbol{\sigma})^{\frac{1}{2}}$, $\sigma_Y(\bar{\boldsymbol{\varepsilon}}_{vp}, \dot{\bar{\boldsymbol{\varepsilon}}}_{vp}, T)$ est la contrainte d'écoulement correspondant à la déformation viscoplastique équivalente cumulée $\bar{\boldsymbol{\varepsilon}}_{vp}$, le taux de contrainte viscoplastique équivalent $\dot{\bar{\boldsymbol{\varepsilon}}}_{vp}$ et T la température.

Comme dans le cas de la plasticité non visqueuse, le taux de déformation viscoplastique et la variation de déformation viscoplastique peuvent être définis comme suit:

$$\begin{aligned} \dot{\boldsymbol{\varepsilon}}_{vp} &= \dot{\lambda} \frac{\partial f}{\partial \boldsymbol{\sigma}} \\ \Delta \boldsymbol{\varepsilon}_{vp} &= \Delta \lambda \frac{\partial f}{\partial \boldsymbol{\sigma}} \end{aligned} \quad (6.12)$$

où $\dot{\lambda}$ est le multiplicateur plastique et peut être déterminé par les conditions de consistance

de la surface de plasticité. Dans le cas du critère de plasticité de Von-Mises, il peut être démontré que,

$$\dot{\bar{\varepsilon}}_{vp} = (\dot{\boldsymbol{\varepsilon}}_{vp}^T \mathbf{A} \dot{\boldsymbol{\varepsilon}}_{vp})^{\frac{1}{2}} = \dot{\lambda} \quad (6.13)$$

En utilisant les equations (6.10), (6.12) nous obtenons,

$$\Delta \boldsymbol{\sigma} = \mathbf{H}^e (\Delta \boldsymbol{\varepsilon} - \Delta \lambda \frac{\partial f}{\partial \boldsymbol{\sigma}} - \ln(1 + \alpha_{th} \Delta T) \mathbf{I}) \quad (6.14)$$

où α_{th} est le coefficient de dilatation thermique. En utilisant une approche incrémentale, la contrainte dans la configuration $\Omega^{t+\Delta t}$ peut alors être calculée comme suit:

$$\boldsymbol{\sigma}^{t+\Delta t} = \boldsymbol{\sigma}_{t+\Delta t}^t + \mathbf{H}^e (\Delta \boldsymbol{\varepsilon} - \frac{\Delta \lambda}{\bar{\boldsymbol{\sigma}}_\beta} \mathbf{P} \boldsymbol{\sigma}_\beta - \ln(1 + \alpha_{th} \Delta T) \mathbf{I}) \quad (6.15)$$

où $\boldsymbol{\sigma}_\beta = (1 - \beta) \boldsymbol{\sigma}^t + \beta \boldsymbol{\sigma}^{t+\Delta t}$; β est un paramètre compris entre 0 et 1 tel que $\beta = 0$ donne un schéma explicite et $\beta = 1$ donne un schéma implicite. Le schéma implicite est inconditionnellement stable et en utilisant le schéma implicite, nous avons,

$$\begin{aligned} \boldsymbol{\sigma}^{t+\Delta t} &= \boldsymbol{\sigma}_{t+\Delta t}^t + \mathbf{H}^e (\Delta \boldsymbol{\varepsilon} - \frac{\Delta \lambda}{\bar{\boldsymbol{\sigma}}^{t+\Delta t}} \mathbf{P} \boldsymbol{\sigma}^{t+\Delta t} - \ln(1 + \alpha_{th} \Delta T) \mathbf{I}) \\ &= \left(\mathbf{I} + \frac{\Delta \lambda}{\bar{\boldsymbol{\sigma}}^{t+\Delta t}} \mathbf{H}^e \mathbf{P} \right)^{-1} (\boldsymbol{\sigma}_{t+\Delta t}^t + \mathbf{H}^e (\Delta \boldsymbol{\varepsilon} - \ln(1 + \alpha_{th} \Delta T) \mathbf{I})) \end{aligned} \quad (6.16)$$

MISE EN OEUVRE PRATIQUE

La mise en oeuvre pratique de la base mathématique de l'API décrite précédemment peut être divisée en trois phases principales:

1. Génération de configurations intermédiaires
2. Correction des surfaces libres des configurations interpolées géométriquement pour obtenir des configurations admissibles cinématiquement

3. Recherche d'une solution statiquement admissible pour l'équilibre basée sur la configuration cinématiquement admissible qui a été calculée.

GÉNÉRATION DES CONFIGURATIONS INTERMÉDIAIRES

La création de formes intermédiaires dans l'approche pseudo-inverse repose sur une interpolation géométrique entre les formes initiale / intermédiaire et la forme finale. Cela impose une restriction selon laquelle les maillages d'éléments finis utilisés à la fois dans la forme finale et dans la forme initiale doivent être cohérents (nombre égal de noeuds et même connectivité d'élément). La forme initiale est obtenue à partir d'une approche inverse en une étape. Il a été démontré que la forme obtenue à partir de l'approche inverse en une étape permet une bonne approximation des formes et des déformations, même si la prévision de la contrainte n'est pas très précise. Le maillage d'éléments finis de la pièce souhaitée est ensuite mappé sur la forme initiale. Ceci est effectué en mappant les noeuds de contour du maillage M^{fin} de la forme souhaitée sur le contour C^0 de la forme initiale. Cela peut être fait efficacement en utilisant les algorithmes de morphing utilisés dans la vision par ordinateur. Les noeuds intérieurs du maillage M^0 peuvent ensuite être déterminés par une solution linéaire de l'équilibre mécanique avec les déplacements imposés sur les noeuds du bord en tant que conditions aux limites.

Une fois que le maillage est créé sur la configuration initiale, on peut créer la configuration intermédiaire en utilisant une interpolation proportionnelle géométrique de la forme,

$$\mathbf{x}^{t+\Delta t} = \mathbf{x}^t + \eta (\mathbf{x}^{fin} - \mathbf{x}^t) \quad (6.17)$$

où $\mathbf{x}^{t+\Delta t}$ est la position nodale de la configuration à l'instant $t + \Delta t$, \mathbf{x}^t est la position nodale de la configuration à l'instant t , \mathbf{x}^{fin} est la position nodale de la configuration finale et η est une constante entre $[0,1]$ dépendant du nombre total des étapes qui est considéré dans la simulation.

Une limite de cette configuration interpolée géométriquement est que les conditions aux limites (conditions de contact) par rapport aux positions de l'outil peuvent ne pas être respectées sur le contour. Pour corriger cette limitation et obtenir une solution cinématiquement admissible proche de la solution statiquement admissible, les noeuds limites de la pièce qui pénètrent dans la surface de l'outil sont projetés sur la surface de l'outil. Puis une solution linéaire est effectuée pour déterminer les nouvelles positions des noeuds internes. En supposant des outils rigides, il est trivial de calculer la position de l'outil correspondant au pas de temps considéré. Étant donné que ces noeuds sont projetés sur la surface de l'outil, ils sont implicitement supposés être en contact avec l'outil. Mais dans la pratique, cela n'est pas nécessairement vrai et les conditions de contact aux noeuds de surface doivent être vérifiées. Pour cela, nous utilisons la méthode de la surface libre. Dans une simulation d'opération de forgeage, pour toute configuration Ω , la condition de surface libre peut être exprimée par,

$$\boldsymbol{\sigma} \mathbf{n} = \mathbf{t} \leq 0 \quad \text{on } \partial\Omega \quad (6.18)$$

où \mathbf{t} est la force de traction perpendiculaire à la surface de la pièce. Cela signifie qu'il y a un chargement en compression sur la limite en contact avec l'outil et aucun chargement sur la surface sans contact avec la surface de l'outil. Pour vérifier que les conditions de surface libre sont respectées, les forces nodales sont calculées sur la configuration interpolée / corrigée géométriquement. En utilisant u, v et w pour désigner les composantes du déplacement nodal dans les directions normale et tangentielle, les cas suivants peuvent être considérés:

1. Si $t_u \geq 0$, le noeud appartient à la surface libre et les conditions aux limites sur le noeud peuvent être représentées par $u \neq 0; v \neq 0; w \neq 0$.
2. Si $t_u < 0$, le noeud est en contact avec la surface de l'outil (force de compression) et les conditions aux limites sur le noeud peuvent être représentées sous la forme $u = 0; v \neq 0; w \neq 0$.

La solution linéaire est effectuée de manière itérative jusqu'à ce que les conditions de contact soient également satisfaites et que la configuration cinématiquement admissible soit obtenue.

Une fois que la configuration cinématiquement admissible est obtenue, la configuration d'équilibre statiquement acceptable qui satisfait à la fois l'équilibre thermique et mécanique est déterminée à l'aide de la formulation mathématique de l'API. La vérification des conditions de contact en utilisant la méthode de la surface libre est effectuée lors des calculs d'équilibre mécanique, également pour maintenir la précision.

RÉSULTATS DE LA SIMULATION ET DISCUSSION

En utilisant la formulation empirique proposée par Johnson et Cook [Johnson & Cook, 1983] pour modéliser le comportement thermo-viscoplastique, la limite d'élasticité peut être définie comme suit:

$$\sigma_Y (\bar{\varepsilon}_{vp}, \dot{\varepsilon}_{vp}, T) = [A + B (\bar{\varepsilon}_{vp})^n] \left[1 + C \log \left(\frac{\dot{\varepsilon}_{vp}}{\dot{\varepsilon}_0} \right) \right] \left[1 - \left(\frac{T - T_0}{T_m - T_0} \right)^m \right] \quad (6.19)$$

À l'aide de ce modèle, nous avons simulé le processus de forgeage de 4 modèles différents et comparé les résultats obtenus avec l'API et les simulations de référence réalisées avec ABAQUS®Explicit.

Le pourcentage d'erreur moyen dans les résultats est calculé en considérant que, $l'erreur \% = \frac{Valeur\ Référence - résultat\ API}{Valeur\ Référence}$.

VIS 2D AXISYMÉTRIQUE

Le cas considéré de la vis axisymétrique est détaillé dans la Sec. (4.2.1) et les formes finale et initiale de la pièce et des outils sont donnés à la fig. (4.1). En comparant les résultats obtenus par l'API et les simulations de référence, nous pouvons voir que l'API permet une bonne approximation des résultats avec un petit nombre de pas (~ 15-30 pas) même avec une analyse couplée température-déplacement. L'erreur dans la valeur maximale de la déformation plas-

tique équivalente calculée est d'environ 12%, celle de la contrainte de Von-Mises est d'environ 9% et celle de la température est environ 1%. Nous constatons également que les tailles de pas utilisées dans l'API jouent un rôle important dans la prévision des températures et, par conséquent, des contraintes en cas de variation importante de la vitesse de déformation plastique. Les grands pas de temps entraînent un effet plus important de la fraction de chaleur inélastique et par conséquent des températures plus élevées. Il faut veiller à ce que les pas de temps soient suffisamment fins pour capturer les effets de la transformation du travail plastique en chaleur. Cet effet peut être mieux exprimé à l'aide de la figure (6.1) qui suit l'évolution des variables de champ au noeud 236.

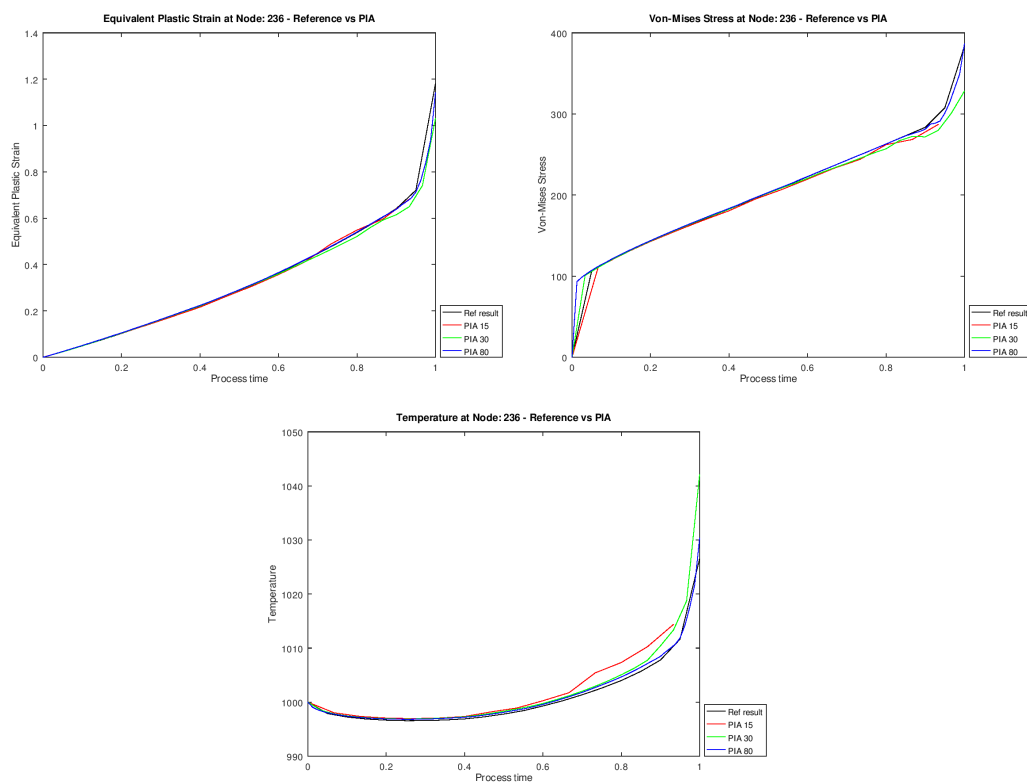


Figure 6.1: Evolution des valeurs de champ au noeud 236 - Vis Axisymétrique, travail inélastique compris. a) Déformation plastique équivalente b) Contrainte de Von-Mises c) Température

Il est facile de constater que la simulation à 30 pas surestime le champ de température en raison de l'effet important de la taille des pas, tandis que la simulation à 80 pas dans l'API

atténue l'effet de la taille des pas et donne donc des résultats comparables aux résultats de référence alors que la déformation plastique équivalente dans les deux cas reste à peu près constante.

ROUE 2D AXISYMETRIQUE

Le modèle de la roue 2D axisymétrique est un modèle capable de capturer les effets de l'évolution des contacts et l'effet de la taille des pas dans l'API. La forme de la pièce finale, le lopin initiale et les outils utilisés pour les besoins de la simulation sont illustrés aux fig. (4.9) et fig. (4.10). Les résultats de la simulation sont illustrés sur les fig. (6.2) et fig. (6.3).

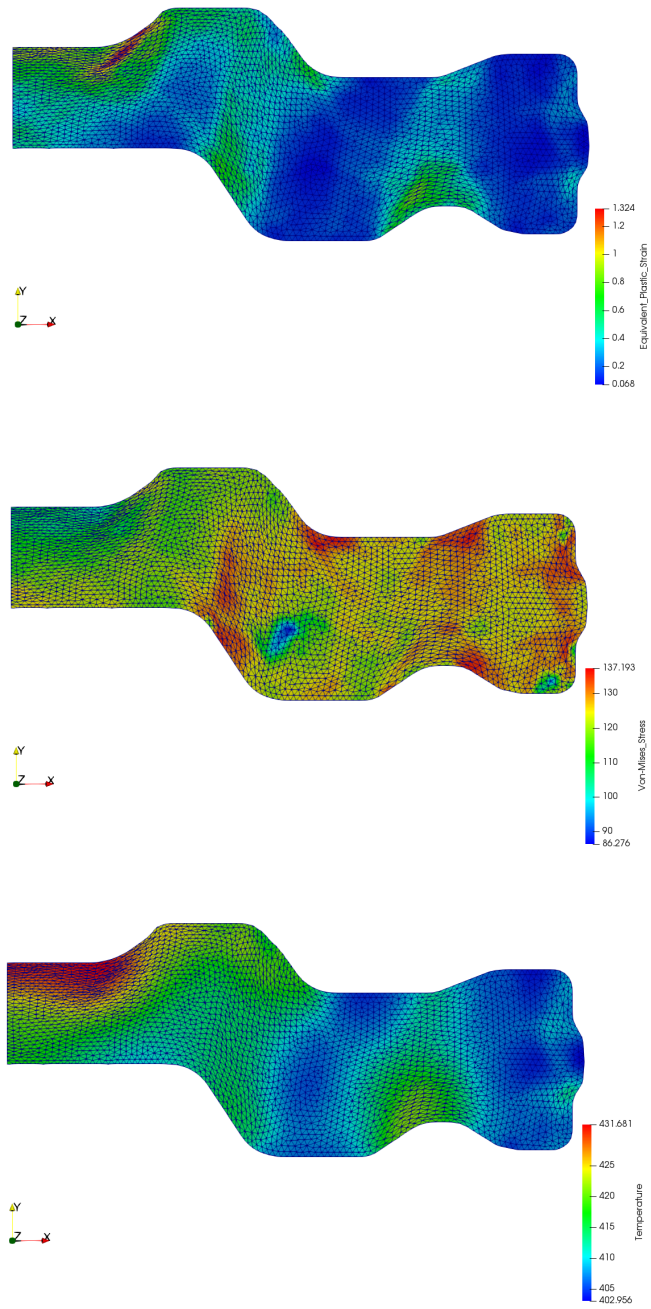


Figure 6.2: Résultats de référence - Roue Axisymétrique. a) Déformation plastique équivalente b) Contrainte équivalente de Von-Mises c) Température

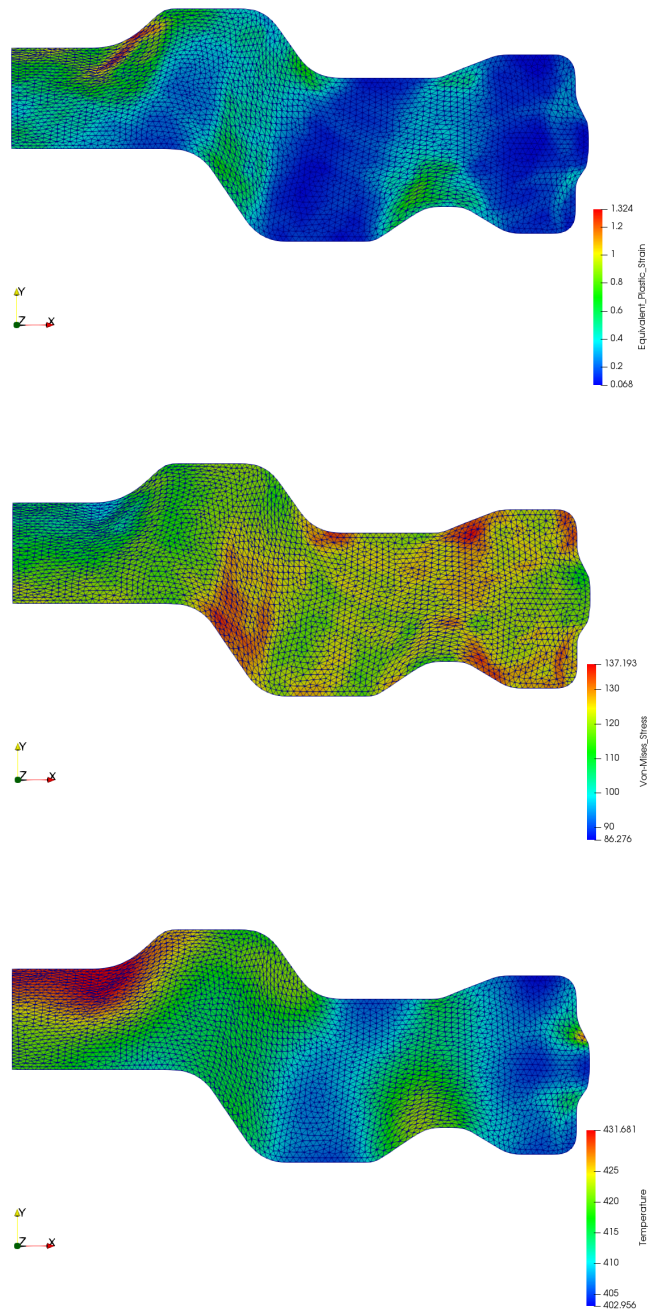


Figure 6.3: Résultats API - Roue Axisymétrique. a) Déformation plastique équivalente b) Contrainte équivalente de Von-Mises c) Température

En comparant les résultats, on constate que l'API produit des résultats très proches de ceux

de la simulation de référence. La taille des pas a un effet notable, en raison duquel le champ de température peut être surestimé ou sous-estimé en raison des grands intervalles de temps utilisés. Les grands pas de temps peuvent entraîner des pertes plus importantes en raison de la conduction entre la pièce et la surface de l'outil, ainsi que des gains plus importants en raison de l'effet plus important du travail plastique.

ÉCRASEMENT D'UN LOPIN 3D

Le premier modèle 3D complet que nous avons envisagé est celui de l'écrasement d'un lopin. Les détails de la simulation peuvent être vus dans la Sec. (4.2.3). Les résultats montrent qu'en raison de la simplicité du modèle, nous pouvons obtenir de bons résultats même avec une approche à un pas (AI), mais pour capturer correctement les effets du travail plastique accumulé dans des modèles plus complexes, plusieurs pas seront nécessaires. Les résultats de la simulation peuvent être analysés en comparant l'évolution des valeurs de champ au noeud 580 comme indiqué sur la figure (6.4).

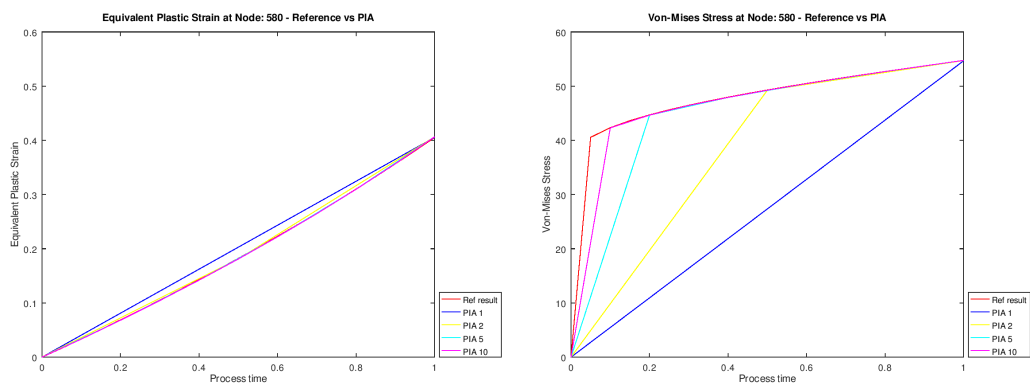


Figure 6.4: Evolution des valeurs de champ au noeud 580: Référence vs API - Ecrasement 3D

COUPE 3D

En raison de la simplicité du modèle d'écrasement 3D, nous avons un modèle légèrement plus compliqué de forgeage d'une coupe 3D. Les détails des paramètres de simulation peuvent être trouvés dans Sec. (4.2.4). Comme dans les cas précédents, l'API montre son efficacité dans la

prédiction des déformées et des valeurs de champ avec une erreur minimale. Les deux modèles 3D que nous avons considérés dans ce manuscrit ont été considérés comme isothermes. Des études complémentaires comprenant le contact thermique complet et le travail plastique doivent être envisagées pour établir la robustesse de l'API pour les simulations complètes de forgeage à chaud en 3D, mais n'ont pas été tentées dans ce travail en raison des contraintes de temps. Néanmoins, les résultats des simulations axisymétriques 2D sont très encourageants et nous nous attendons à ce que l'API soit un outil très puissant pour la simulation plus rapide du procédé de forgeage à chaud.

References

Abbes, B., Li, Y. M., Halouani, A., & Guo, Y. Q. (2014). Fast plastic integration algorithms for forming process simulations. In *Material Forming ESAFORM 2014*, volume 611 of *Key Engineering Materials* (pp. 1336–1343).: Trans Tech Publications.

Ali Halouani, Yuming Li, B. A. & Guo, Y.-Q. (2010). An axisymmetric inverse approach for cold forging modeling. In *Proceedings of the World Congress on Engineering*, volume 2 (pp. 1230–1235).

Altan, T. (1983). *Metal Forming: Fundamentals and Applications (ASM Series in Metal Processing)*. ASM International.

Argyris, J. . H. (1965). Elasto-plastic matrix displacement analysis of three-dimensional continua. *The Journal of the Royal Aeronautical Society*, 69(657), 633–636.

Armero, F. & Simo, J. (1993). A priori stability estimates and unconditionally stable product formula algorithms for nonlinear coupled thermoplasticity. *International Journal of Plasticity*, 9(6), 749–782.

Babuška, I. (1971). Error-bounds for finite element method. *Numerische Mathematik*, 16(4), 322–333.

Badrinarayanan, S. & Zabaras, N. (1996). A sensitivity analysis for the optimal design of metal-forming processes. *Computer Methods in Applied Mechanics and Engineering*, 129(4), 319 – 348.

- Baker, T. J. (2002). Mesh movement and metamorphosis. *Engineering with Computers*, 18(3), 188–198.
- Bathe, K.-J. (1996). *Finite Element Procedures*. Prentice Hall.
- Bathe, K.-J., Ramm, E., & Wilson, E. L. (1975). Finite element formulations for large deformation dynamic analysis. *International Journal for Numerical Methods in Engineering*, 9(2), 353–386.
- Black, J. T. & Kohser, R. A. (2011). *DeGarmo's Materials and Processes in Manufacturing*. Wiley.
- Bonet, J. & Wood, R. D. (2008). *Nonlinear Continuum Mechanics for Finite Element Analysis*. Cambridge University Press.
- Brezzi, F. (1974). On the existence, uniqueness and approximation of saddle-point problems arising from lagrangian multipliers. *ESAIM: Mathematical Modelling and Numerical Analysis - Modélisation Mathématique et Analyse Numérique*, 8(R2), 129–151.
- Carosio, A., Willam, K., & Etse, G. (2000). On the consistency of viscoplastic formulations. *International Journal of Solids and Structures*, 37(48-50), 7349–7369.
- Castellazzi, G., Artioli, E., & Krysl, P. (2015). Linear tetrahedral element for problems of plastic deformation. *Meccanica*, 50(12), 3069–3086.
- Cheng, J.-H. & Kikuchi, N. (1985). An analysis of metal forming processes using large deformation elastic-plastic formulations. *Computer Methods in Applied Mechanics and Engineering*, 49(1), 71 – 108.
- Chenot, J.-L. (1998). New trends in finite element modelling of metal forming processes. In *Advances in Computational Structural Mechanics*: Civil-Comp Press.

- Ciancio, C., Citrea, T., Ambrogio, G., Filice, L., & Musmanno, R. (2015). Design of a high performance predictive tool for forging operation. *Procedia CIRP*, 33, 173–178.
- Corona, E. & Orient, G. E. (2014). *An evaluation of the Johnson-Cook model to simulate puncture of 7075 aluminum plates*. Technical report, Sandia National Laboratories.
- D'Addona, D. M. & Antonelli, D. (2018). Neural network multiobjective optimization of hot forging. *Procedia CIRP*, 67, 498–503.
- Dheeravongkit, A. & Shimada, K. (2005a). Inverse pre-deformation of finite element mesh for large deformation analysis. *Journal of Computing and Information Science in Engineering*, 5(4), 338.
- Dheeravongkit, A. & Shimada, K. (2005b). Inverse pre-deformation of tetrahedral mesh for large deformation finite element analysis. *Computer-Aided Design and Applications*, 2(6), 805–814.
- Dheeravongkit, A. & Shimada, K. (2007). Inverse adaptation of a hex-dominant mesh for large deformation finite element analysis. *Computer-Aided Design*, 39(5), 427–438.
- Douglas, R. & Kuhlmann, D. (2000). Guidelines for precision hot forging with applications. *Journal of Materials Processing Technology*, 98(2), 182 – 188.
- Ejday, M. & Fourment, L. (2010). Metamodel assisted evolutionary algorithm for multi-objective optimization of non-steady metal forming problems. *International Journal of Material Forming*, 3(S1), 5–8.
- FIA (2019). Forging Industry Association. <https://www.forging.org/forging/design/product-design-guide-forging.html>. [Online; accessed 6-January-2019].
- Fosdick, R. & Royer-Carfagni, G. (1999). The lagrange multiplier in incompressible elasticity theory. *Journal of Elasticity*, 55(3), 193–200.

- Fourment, L. & Chenot, J. L. (1996). Optimal design for non-steady-state metal forming processes i. shape optimization method. *International Journal for Numerical Methods in Engineering*, 39(1), 33–50.
- Fourment, L., Chenot, J. L., & Balan, T. (1996). Optimal design for non-steady-state metal forming processes ii. application of shape optimization in forging. *International Journal for Numerical Methods in Engineering*, 39(1), 51–65.
- Gati, W., Guo, Y. Q., Naceur, H., & Batoz, J.-L. (2003). Approche pseudo inverse pour estimation des contraintes dans les pieces embouties axisymetriques. *Revue Europeenne des Elements Finis*, 12(7-8), 863–886.
- Germain, S., Landkammer, P., & Steinmann, P. (2014). On a recursive formulation for solving inverse form finding problems in isotropic elastoplasticity. *Advanced Modeling and Simulation in Engineering Sciences*, 1(1), 10.
- Germain, S., Scherer, M., & Steinmann, P. (2010). On inverse form finding for anisotropic hyperelasticity in logarithmic strain space. *International Journal of Structural Changes in Solids – Mechanics and Applications*, 2(2), 1–16.
- Govindjee, S. & Mihalic, P. A. (1996). Computational methods for inverse finite elastostatics. *Computer Methods in Applied Mechanics and Engineering*, 136(1-2), 47–57.
- Govindjee, S. & Mihalic, P. A. (1998). Computational methods for inverse deformations in quasi-incompressible finite elasticity. *International Journal for Numerical Methods in Engineering*, 43(5), 821–838.
- Groover, M. P. (2010). *Fundamentals of Modern Manufacturing*. John Wiley and Sons Ltd.
- Guo, Y., Li, Y., Bogard, F., & Debray, K. (2004). An efficient pseudo-inverse approach for damage modeling in the sheet forming process. *Journal of Materials Processing Technology*, 151(1-3), 88–97.

- Guo, Y. Q., Batoz, J. L., Detraux, J. M., & Duroux, P. (1990). Finite element procedures for strain estimations of sheet metal forming parts. *International Journal for Numerical Methods in Engineering*, 30(8), 1385–1401.
- Halouani, A., Li, Y., Abbès, B., Guo, Y., Meng, F., Labergère, C., & Lafon, P. (2012a). Optimization of forging preforms by using pseudo inverse approach. *Key Engineering Materials*, 504-506, 613–618.
- Halouani, A., Li, Y., Abbas, B., & Guo, Y.-Q. (2010). An efficient axi-symmetric element based on inverse approach for cold forging modeling. *Engineering Letters*, 18(4).
- Halouani, A., Li, Y. M., Abbès, B., & Guo, Y. (2011a). Simulation of axi-symmetrical forging process by “inverse approach”. *Materials Science Forum*, 675-677, 1007–1010.
- Halouani, A., Li, Y. M., Abbas, B., & Guo, Y. Q. (2011b). Numerical modeling of axi-symmetrical cold forging process by pseudo inverse approach. In *AIP Conference Proceedings*: AIP.
- Halouani, A., Li, Y. M., Abbas, B., & Guo, Y. Q. (2011c). A pseudo inverse approach with kinematically admissible intermediate configurations for the axi-symmetrical cold forging modelling. *Advanced Materials Research*, 399-401, 1832–1837.
- Halouani, A., Li, Y. M., Abbas, B., & Guo, Y. Q. (2011d). A simplified inverse approach for the simulation of axi-symmetrical cold forging process. In *International Conference on Advances in Materials and Process Technologies*, volume 1315 (pp. 297–302): AIP.
- Halouani, A., Li, Y. M., Abbas, B., & Guo, Y. Q. (2012b). Simulation of axi-symmetrical cold forging process by efficient pseudo inverse approach and direct algorithm of plasticity. *Finite Elements in Analysis and Design*, 61, 85–96.

- Halouani, A., Li, Y. M., Abbès, B., & Guo, Y. Q. (2015). Fast plastic integration algorithm for damage prediction in forming process simulations. *Applied Mechanics and Materials*, 784, 342–349.
- HALOUANI, A., ming LI, Y., ABBES, B., & qiao GUO, Y. (2012). Optimization of cold forging perform tools using pseudo inverse approach. *Transactions of Nonferrous Metals Society of China*, 22, s207–s213.
- Hartley, P. & Pillinger, I. (2006). Numerical simulation of the forging process. *Computer Methods in Applied Mechanics and Engineering*, 195(48-49), 6676–6690.
- Heeres, O. M., Suiker, A. S., & de Borst, R. (2002). A comparison between the perzyna viscoplastic model and the consistency viscoplastic model. *European Journal of Mechanics - A/Solids*, 21(1), 1–12.
- Helm, P. A., Younes, L., Beg, M. F., Ennis, D. B., Leclercq, C., Faris, O. P., McVeigh, E., Kass, D., Miller, M. I., & Winslow, R. L. (2006). Evidence of structural remodeling in the dyssynchronous failing heart. *Circulation Research*, 98(1), 125–132.
- Herrmann, L. R. (1965). Elasticity equations for incompressible and nearly incompressible materials by a variational theorem. *AIAA Journal*, 3(10), 1896–1900.
- Hibbitt, H., Marcal, P., & Rice, J. (1970). A finite element formulation for problems of large strain and large displacement. *International Journal of Solids and Structures*, 6(8), 1069–1086.
- Hill, R. (1968). On constitutive inequalities for simple materials—i. *Journal of the Mechanics and Physics of Solids*, 16(4), 229–242.
- Hughes, T. J. R. (2000). *The Finite Element Method: Linear Static and Dynamic Finite Element Analysis*. DOVER PUBN INC.

- Jinka, A. G. K. & Lewis, R. W. (1994). Incompressibility and axisymmetry: A modified mixed and penalty formulation. *International Journal for Numerical Methods in Engineering*, 37(10), 1623–1649.
- Johnson, G. & Cook, W. (1983). A constitutive model and data for metals subjected to large strains, high strain rates, and high temperatures. In *Proceedings of the 7th International Symposium on Ballistics* (pp. 541–547). The Hague.
- Karbasian, H. & Tekkaya, A. (2010). A review on hot stamping. *Journal of Materials Processing Technology*, 210(15), 2103–2118.
- Landkammer, P., Germain, S., & Steinmann, P. (2014). On inverse form finding for orthotropic plasticity. *Computer Assisted Mechanics and Engineering Sciences*, 20, 337–348. UnivIS-Import:2015-03-09:Pub.2013.tech.FT.FT-TM.oninve.
- Li, Y. M., Abbas, B., & Guo, Y. Q. (2007). Two efficient algorithms of plastic integration for sheet forming modeling. *Journal of Manufacturing Science and Engineering*, 129(4), 698.
- Liu, W., Zhang, X., & Hu, P. (2017). Developments of multi-step simulations in sheet metal forming processes. *The International Journal of Advanced Manufacturing Technology*, 93(1-4), 1379–1397.
- Lo, S. & Ling, C. (2000). Improvement on the 10-node tetrahedral element for three-dimensional problems. *Computer Methods in Applied Mechanics and Engineering*, 189(3), 961–974.
- Lu, J. & Li, L. (2017). Determining the reference geometry of plastically deformed material body undergone monotonic loading and moderately large deformation. *Finite Elements in Analysis and Design*, 130, 1–11.
- Mackerle, J. (2006). Finite element modelling and simulation of bulk material forming: A bibliography (1996 - 2005). *Engineering Computations*, 23(3), 250–342.

- Marcal, P. & King, I. (1967). Elastic-plastic analysis of two-dimensional stress systems by the finite element method. *International Journal of Mechanical Sciences*, 9(3), 143–155.
- Massivumformung, I. I. (2011). Basic knowledge: Forgings – significance, design, production, application.
- McMeeking, R. & Rice, J. (1975). Finite-element formulations for problems of large elastic-plastic deformation. *International Journal of Solids and Structures*, 11(5), 601–616.
- Neto, F. D. M. & da Silva Neto, A. J. (2013). *An Introduction to Inverse Problems with Applications*. Springer Berlin Heidelberg.
- Oden, J. T. (1969). Finite element formulation of problems of finite deformation and irreversible thermodynamics of nonlinear continua. In *Symposium of Applied Finite Element Methods in Civil Engineering* (pp. 419–456).
- Park, J. & Kobayashi, S. (1984). Three-dimensional finite element analysis of block compression. *International Journal of Mechanical Sciences*, 26(3), 165–176.
- Park, J., Rebelo, N., & Kobayashi, S. (1983). A new approach to preform design in metal forming with the finite element method. *International Journal of Machine Tool Design and Research*, 23(1), 71 – 79.
- Perzyna, P. (1966). Fundamental problems in viscoplasticity. In G. Chernyi, H. Dryden, P. Germain, L. Howarth, W. Olszak, W. Prager, R. Probstein, & H. Ziegler (Eds.), *Advances in Applied Mechanics*, volume 9 (pp. 243 – 377). Elsevier.
- Plannja (1973). Patent Number: SE7315058-3.
- Plannja (1977). Manufacturing a hardened steel article. Patent Number: GB1490535.
- Pope, G. G. (1966). A discrete element method for the analysis of plane elasto-plastic stress problems. *Aeronautical Quarterly*, 17(01), 83–104.

- Rittel, D., Zhang, L., & Osovski, S. (2017). The dependence of the Taylor–Quinney coefficient on the dynamic loading mode. *Journal of the Mechanics and Physics of Solids*, 107, 96–114.
- Rowe, G. W., Sturgess, C. E. N., & Hartley, P. (2005). *Finite-Element Plasticity and Metalforming Analysis*. Cambridge University Press.
- Shontz, S. M. & Vavasis, S. A. (2010). Analysis of and workarounds for element reversal for a finite element-based algorithm for warping triangular and tetrahedral meshes. *BIT Numerical Mathematics*, 50(4), 863–884.
- Simo, J. C. & Taylor, R. L. (1986). A return mapping algorithm for plane stress elastoplasticity. *International Journal for Numerical Methods in Engineering*, 22(3), 649–670.
- Simufact (2019). Hot forging. <https://www.simufact.com/hot-forging.html>. [Online; accessed 6-January-2019].
- Smith, I. M., Griffiths, D. V., & Margetts, L. (2013). *Programming the Finite Element Method*. John Wiley & Sons.
- Sobolev, A. & Radchenko, M. (2016). Use of Johnson–Cook plasticity model for numerical simulations of the SNF shipping cask drop tests. *Nuclear Energy and Technology*, 2(4), 272–276.
- Soyris, N., Fourment, L., Coupez, T., Cescutti, J., Brachotte, G., & Chenot, J. (1992). Forging of a connecting rod: 3d finite element calculations. *Engineering Computations*, 9(1), 63–80.
- Stankus, S. V., Savchenko, I. V., Baginskii, A. V., Verba, O. I., Prokop'ev, A. M., & Khairulin, R. A. (2008). Thermal conductivity and thermal diffusivity coefficients of 12kh18n10t stainless steel in a wide temperature range. *High Temperature*, 46(5), 731–733.

Staten, M. L., Owen, S. J., Shontz, S. M., Salinger, A. G., & Coffey, T. S. (2012). A comparison of mesh morphing methods for 3d shape optimization. In W. R. Quadros (Ed.), *Proceedings of the 20th International Meshing Roundtable* (pp. 293–311). Berlin, Heidelberg: Springer Berlin Heidelberg.

Steinmann, P. & Landkammer, P. (2014). A fast approach to shape optimization using the inverse fem. In *Material Forming ESAFORM 2014*, volume 611 of *Key Engineering Materials* (pp. 1404–1410).: Trans Tech Publications.

Surdon, G. & Chenot, J. L. (1987). Finite element calculation of three-dimensional hot forging. *International Journal for Numerical Methods in Engineering*, 24(11), 2107–2117.

Taylor, G. I. & Quinney, H. (1934). The latent energy remaining in a metal after cold working. *Proceedings of the Royal Society A: Mathematical, Physical and Engineering Sciences*, 143(849), 307–326.

Taylor, R. L. (2000). A mixed-enhanced formulation tetrahedral finite elements. *International Journal for Numerical Methods in Engineering*, 47(1-3), 205–227.

van den Boogaard, A. H., Borst, R. D., & van den Bogert, P. A. J. (1994). An adaptive time-stepping algorithm for quasistatic processes. *Communications in Numerical Methods in Engineering*, 10(10), 837–844.

Vaz, M. & Lange, M. R. (2016). Thermo-mechanical coupling strategies in elastic–plastic problems. *Continuum Mechanics and Thermodynamics*, 29(2), 373–383.

Wagoner, R. H. & Chenot, J.-L. (2005). *Metal Forming Analysis*. Cambridge University Press.

Wang, W. & Sluys, L. (2000). Formulation of an implicit algorithm for finite deformation viscoplasticity. *International Journal of Solids and Structures*, 37(48-50), 7329–7348.

- Wang, W. M., Sluys, L. J., & de Borst, R. (1997). Viscoplasticity for instabilities due to strain softening and strain-rate softening. *International Journal for Numerical Methods in Engineering*, 40(20), 3839–3864.
- Wankhede, A. & Lehn, N. (2017). *Lightweighting World*, volume 2, chapter Hot Forming: Crucial Technology for Lightweighting of Sheet Metal Components. RM Publishing Group.
- Washizu, K. (1974). *Variational methods in elasticity and plasticity (International series of monographs in aeronautics and astronautics. Division I: solid and structural mechanics, v. 9)*. Pergamon Press.
- Xiao, H., Bruhns, O. T., & Meyers, A. (1997). Logarithmic strain, logarithmic spin and logarithmic rate. *Acta Mechanica*, 124(1), 89–105.
- Yamada, T. (1995). Finite element procedure of initial shape determination for hyperelasticity. In S. N. Atluri, G. Yagawa, & T. Cruse (Eds.), *Computational Mechanics '95* (pp. 2456–2461). Berlin, Heidelberg: Springer Berlin Heidelberg.
- Yamada, Y., Yoshimura, N., & Sakurai, T. (1968). Plastic stress-strain matrix and its application for the solution of elastic-plastic problems by the finite element method. *International Journal of Mechanical Sciences*, 10(5), 343–354.
- Yang, C. & Ngaile, G. (2009). Preform design for forging processes based on geometrical resemblance. In *ASME 2009 International Manufacturing Science and Engineering Conference, Volume 1*: ASME.
- Zaera, R. & Fernández-Sáez, J. (2006). An implicit consistent algorithm for the integration of thermoviscoplastic constitutive equations in adiabatic conditions and finite deformations. *International Journal of Solids and Structures*, 43(6), 1594–1612.

Zienkiewicz, O. C. (1974). Constrained variational principles and penalty function methods in finite element analysis. In *Lecture Notes in Mathematics* (pp. 207–214). Springer Berlin Heidelberg.

Zienkiewicz, O. C. & Taylor, R. L. (2000a). *Finite Element Method: Volume 1, Fifth Edition*. Butterworth-Heinemann.

Zienkiewicz, O. C. & Taylor, R. L. (2000b). *Finite Element Method: Volume 2, Fifth Edition*. Butterworth-Heinemann.

Zienkiewicz, O. C., Valliappan, S., & King, I. P. (1969). Elasto-plastic solutions of engineering problems 'initial stress', finite element approach. *International Journal for Numerical Methods in Engineering*, 1(1), 75–100.

Modélisation numérique thermo-viscoplastique du procédé de forgeage des métaux par l'Approche Pseudo Inverse

Le forgeage à chaud est un procédé de formage des métaux utilisé pour former des matériaux qui sont difficiles à former à froid ainsi que pour réaliser des géométries complexes. La réduction de la limite d'élasticité à haute température et une augmentation subséquente de l'aptitude à la mise en forme constituent le principal mécanisme à l'origine du procédé. Les méthodes numériques constituent un moyen efficace de prédire les états de contrainte / déformation du produit à différentes étapes de la mise en forme. Bien que les méthodes classiques soient suffisamment précises pour fournir une représentation appropriée du procédé, elles ont tendance à être coûteuses en ressources informatiques. Cela limite leur utilisation dans des cas concrets, en particulier pour des études d'optimisation du procédé. L'approche pseudo inverse (API), développée dans le contexte du forgeage à froid 2D axisymétrique, fournit une estimation rapide des champs de contrainte et de déformation dans le produit final pour une forme initiale donnée. Dans ce travail, l'API est étendue pour inclure les effets thermiques et viscoplastiques dans le procédé de forgeage ainsi que dans le cas général 3D. Les résultats sont comparés aux codes commerciaux disponibles basés sur les approches classiques pour montrer l'efficacité et les limites de l'API. Les résultats obtenus indiquent que l'API est un outil assez efficace pouvant être utilisé à la fois pour des simulations 2D et 3D du forgeage à chaud.

Mots-clés en français : L'approche Pseudo Inverse, Grandes déformations, Comportement thermo-viscoplastique, Mise en forme des matériaux, Méthode des éléments finis, Forgeage à chaud

Thermo-viscoplastic numerical modeling of metal forging process by the Pseudo Inverse Approach

Hot forging is a metal forming process used to form difficult-to-form materials as well as to achieve complex geometries. The reduction of yield stress at high temperatures and a subsequent increase in formability is the primary mechanism that drives the process. Numerical methods provide an efficient means to predict the material yield and the stress/strain states of the product at different stages of forming. Although classical methods are accurate enough to provide a suitable representation of the process, they tend to be computationally expensive. This limits its use in practical cases especially for process optimization. Pseudo Inverse Approach (PIA) developed in the context of 2D axisymmetric cold forming, provides a quick estimate of the stress and strain fields in the final product for a given initial shape. In this work, the PIA is extended to include the thermal and viscoplastic effects on the forging process as well as to the general 3D case. The results are compared with commercially available software based on the classical approaches, to show the efficiency and the limitations of PIA. The results obtained indicate that PIA is a quite effective tool that can be used for both 2D and 3D simulations of hot forging.

Mots-clés en anglais: Pseudo Inverse Approach, Large deformations, Thermo-viscoplastic behaviour, Material forming, Finite element method, Hot forging

Discipline : MÉCANIQUE DES SOLIDES, GÉNIE MÉCANIQUE, PRODUCTIQUE, TRANSPORT ET GÉNIE CIVIL

Spécialité : SGM - Sciences et Génie des Matériaux

Université de Reims Champagne-Ardenne

ISI / GRESPI - EA 4694

UFR SEN,

Campus Moulin de la Housse,

51100 Reims, FRANCE

